UNIVERSITY OF CALIFORNIA
RIVERSIDE

Photomechanical, Photothermal and Photothermomechanical Mechanisms of Interaction of Nanosecond-Long Laser Pulses With Artificial Tissue Models and Pigmented Melanoma Cells in Medical Applications

A Dissertation submitted in partial satisfaction
of the requirements for the degree of

Doctor of Philosophy

in

Mechanical Engineering

by

Francisco Gerardo Pérez Gutiérrez

August 2010

Dissertation Committee
Dr. Guillermo Aguilar, Chairperson
Dr. Shankar Mahalingam
Dr. Marko Princevac

The dissertation of Francisco Gerardo Pérez Gutiérrez is approved:

_____

_____

_____

Committee chairperson

University of California, Riverside

ACKNOWLEDGMENTS

First of all I want to express my gratitude to my family for their love and support provided during all my life. Thanks to my parents for their love, countless prayers and letting me free to decide my own way. Thanks to my brother for his friendship, and to my sister for being her.

I would like to acknowledge my advisor, Prof. Guillermo Aguilar, for his support and patience during all these years. For making sure I had everything I needed to work and to live. For giving me total freedom to work on whatever I wanted and whenever I wanted. For trusting in me from the beginning to the end, even when things were not going well.

Dr. Santiago Camacho López deserves special mention. His patient advice and encouragement made possible that I became familiar with lasers and optics. He always made himself available to help me whenever I needed it. His mentorship is invaluable.

Dr. John Viator was an excellent guide in photoacoustics.

I want to thank all the colleagues I worked with throughout my graduate studies: Elias Penilla, Dr. Rodger Evans, Dr. Lorenzo Martínez Suástegui, Gabriel Guillen, Edgar Arturo Chávez Urbiola, Dr. Henry Vu, Dr. Jie Liu, Dr. Walfre Franco, Dr. Ricardo Romero Mendez, Dr. Feng Sun, Adam Slade, Erica Young. I learned something from all of you, not only about lasers and cells.

Very importantly I would like to thank Dr. Ricardo Romero Méndez, who has been an excellent mentor since I was an undergraduate student and encouraged me to pursue graduate studies. If I hadn't met him, I wouldn't have chosen this career.

I would like to thank all my friends in Riverside, who made possible that I enjoyed my time here. I will miss you all.

Finally, I need to thank the UC MEXUS-CONACyT Doctoral Fellowship program for providing most of the financial support for my graduate studies. In addition, I would also like to thank the Chancellor's Dissertation Grant and the 2009 UC MEXUS Dissertation Research Grant for the financial support provided.

DEDICATION

To my father, mother, brother and sister. This wouldn't have happened without you.

ABSTRACT OF THE DISSERTATION

Photomechanical, Photothermal and Photothermomechanical Mechanisms of Interaction of Nanosecond Laser Pulses With Artificial Tissue Models and Pigmented Melanoma Cells in Medical Applications

by

Francisco Gerardo Pérez Gutiérrez

Doctor of Philosophy, Graduate Program in Mechanical Engineering
University of California, Riverside, August 2010
Dr. Guillermo Aguilar, Chairperson

Current therapy to remove vascular lesions involves long laser pulses to coagulate the blood vessels with partial success. Small blood vessels, with thermal relaxation time shorter than the long laser pulses, remain. Skin models incorporating light scattering were irradiated with nanosecond laser pulses. The objective is to destroy blood vessels taking advantage of the short laser pulse high intensity to induce plasma mediated cavitation bubbles. These bubbles may serve as photodisruption mechanism of blood vessels. It was found that permanent or transient bubbles were produced depending on the laser dose, number of pulses and repetition rate. Scattering added to the skin models increased the threshold fluence for plasma formation.

Such fast energy deposition from nanosecond laser pulses implies mechanical effects. Laser energy is coupled to a material through a combination of linear and nonlinear absorption. The first results in heat generation and thermoelastic expansion; while the second results in an expanding plasma formation that creates a shock wave and a cavitation bubble. It was found that the shock wave emitted upon plasma formation is spherical while the pressure wave emitted by pure linear absorption has a plane and cylindrical components. For irradiation of an absorbing solution with no plasma formation, the local pressure was

calculated using empirical correlations. The low local pressure explains the bubble formation at low temperature increments.

When nanosecond laser pulses are applied to absorbing microspheres, thermoelastic expansion of the microparticles originates pressure waves. A melanoma detector takes advantage of this principle. Excessive energy creates bubbles around melanosomes damaging the plasma membrane. Optimum laser parameters for this application must be found. Melanoma cells were irradiated at 355 and 532 nm wavelengths to determine cell survival rate, compare the photoacoustic signal, determine the critical laser fluence for melanin leakage and study the intracellular interactions and their effect on the plasma membrane integrity. Cell survival decreased with increasing laser fluence, although the decrement is more pronounced at 355 nm. Melanin leaks from cells equally for both wavelengths. No significant difference in photoacustic signal was found between wavelengths. Damage to plasma membrane due to bubble formation was imaged.

Table of Contents

List of Figures

hemoglobin absorption of green light. (Insert) Absorption coefficient spectrum of hemoglobin and other skin chromophores for comparison purposes.

Fig.4.2A. Experimental set-up for measurement of pressure transients with PVDF sensors.

Fig. 4.2B. Laser exposure configuration when the beam waist was positioned on the surface of the agar gel.

Fig. 4.2C. Laser exposure configuration when the beam waist was positioned 1 mm below the surface of the agar gel.

Fig. 4.3. Experimental set up for time-resolved imaging (TRI) and equivalent target plane (ETP) system.

Fig 4.4 Experimental set up for TRIF. Pump and probe pulses are electronically synchronized as in Fig. 4.3.

Fig. 4.5. Pressure signal detected with PVDF sensor when the beam waist was positioned 1 mm below the surface of the agar gel and 10 mm away from the PVDF sensor.

Fig. 4.6. Pressure amplitude measured 10 mm away from the beam waist as a function of energy. Beam waist was positioned 1 mm below the surface of the agar gel.

Fig. 4.7. Pressure distribution within agar gel from 1 mm to 10 mm measured with PVDF sensor. Energy per pulse was 500 μJ.

Fig. 4.8. Pressure distribution within agar gel from 50 μm to 10 mm measured with PVDF sensor and TRI. Energy per pulse was 500 μJ.

Fig. 4.9A. Pressure signal obtained with a PVDF sensor when an unfocused, 6 ns laser pulse is incident on an absorbing, 10 mm thick agar gel. μ_a=33 cm^{-1}.

Fig. 4.9B. Pressure signal obtained with PVDF sensor when a focused, 6 ns laser pulse is incident on an absorbing 10 mm thick agar gel. Beam waist was positioned on the surface of the agar gel. μ_a=33 cm^{-1}.

Fig. 4.9C. Pressure signal obtained with PVDF sensor. Focused, 6 ns laser pulse is incident on absorbing, 10 mm thick agar gel. The beam waist was positioned 1 mm below the agar gel surface. μ_a=33 cm^{-1}.

Fig. 4.10. Pressure amplitude as a function of per pulse energy. Laser pulses were incident 1 mm below the surface of agar gel blocks.

Fig. 4.11. Shock wave induced focusing a 6 ns laser pulse in air.

Fig. 4.12. Plane wave propagating downwards originated by an unfocused nanosecond laser pulse inciden ton a Direct Red solution with μ_a= 22cm^{-1}

Fig. 4.13. Simple image of a cavitation bubble formed when a nanosecond laser pulse focused in the bulk of a Direct Red solution didn't have enough intensity to produce plasma.

Fig. 4.14. TRIF image of a cavitation bubble when a nanosecond laser pulse a nanosecond laser pulse focused in the bulk of a Direct Red solution didn't have enough intensity to produce plasma. No phase shift was observed.

Fig. 4.15. TRIF images when a collimated nanosecond laser pulse was incident on a quartz cuvette filled with Direct Red solution. Laser spot size was 1 mm. No significant difference in the phase change was observed as a function of time.

Fig. 4.16. Cavitation bubbles formed in the bulk of a Direct Red soultion with μ_a=22 cm^{-1}. Energy per pulse was 5 mJ and laser spot size 1 mm. Under such conditions the maximum calculated temperature increment was ~3 ^oC.

Fig. 4.17. Fringe shape can be approximated as a triangle. Using eq 4.3 and measuring the distances x_m and R, the maximum refractive index change can be calculated.

Fig. 5.1. Experimental set up for laser irradiation of melanoma cells with nanosecond laser pulses with λ=355 and 532 nm. Second or third harmonic was delivered to the sample inserting or removing the removable mirror (RM). HeNe laser serves as aiming beam. Target's holder was displaced in the X-Y direction to provide four laser pulses to each sample without overlapping of laser exposure on the same cells.

Fig. 5.2. Experimental set up for time-resolved imaging (TRI) of melanoma cells. Lasers Nd:YAG 1 as pump (λ=355 or 532 nm) and Nd:YAG 2 as probe (λ=1064 nm) are externally triggered and synchronized by delay generator (DG) at 10 Hz repetition rate. Second or third harmonic from Nd:YAG 1 laser is released to the sample inserting or removing removable mirror (RM). Mechanical shutter (MS) and CCD camera are triggered by a signal generator (SG); both, MS and CCD camera's shutter are open for 100 ms to ensure that only one pump and one probe pulses irradiate the sample and get to the camera respectively, when the lasers are triggered at 10Hz repetition rate.

Fig. 5.3. Absolute value of a typical waveform obtained with oscilloscope for comparison of photoacoustic signal at λ=355 and 532 nm. Signal was integrated from 1.6×10^{-6} to 2.5×10^{-6} sec to include the calculated acoustic depth of the irradiation well. Laser fluence was 1 J cm^{-2}, λ= 532 nm and data acquisition was at 32 dB amplification. Inserted figure shows the raw signal as it was acquired with the oscilloscope.

Fig. 5.4. Experimental set up for comparison of photoacoustic pressure at λ=355 nm and λ=532 nm. The laser pulse is brought to the melanoma cells (sample) through a focusing lens and a prism. The cells are contained in an acrylic well and diluted in Tryple E to avoid cell clumpling. The PVDF ultrasonic transducer is protected from laser damage with a 1% intralipid acrylamide disk.

Fig. 5.5. Normalized cell survival of melanoma cells irradiated with 6 ns laser pulses with λ= 355 and 532 nm. Significant difference was found in the curves for both wavelengths according to statistical analysis with $p < 0.0001$. Cell survival was normalized according to equation 2 (see body of the text), where the total number of the cells in the sample, and not only cells reached by laser, contributed to the calculation. Each data point is the average of 5 measurements with its corresponding error bars.

Fig. 5.6. Normalized PBS absorbance as a function of laser fluence. Absorbance was measured using a nanodrop spectrophotometer with λ=220 nm. Laser irradiation was carried out at λ = 355 and 532 nm. Data normalization was done with respect to the average of data points obtained with control samples (fluence = 0).

Fig. 5.7. Comparison of photoacoustic signal for λ=532 nm and 355 nm as a function of fluence. Wavelength was found to be a variable with no statistically significance to the integrated pressure obtained.

Fig. 5.8. Time-resolved imaging of melanoma cells **(A)** before and **(B)** 50 ns after a single, 6 ns laser pulse, λ=355 nm, 0.3 J/cm^2 was delivered to cells. Arrows in part **A** show undamaged cells before laser exposure; arrows in part **B** clearly showxiv cells where microbubbles were induced by the laser pulse.

Fig. 5.9. Time-resolved imaging of melanoma cells **(A)** before and **(B)** 50 ns after a single, 6 ns laser pulse, λ=532 nm, 0.65 J/cm^2 was delivered to cells. Arrows in part **A** show undamaged cells by laser exposure, arrows in part **B** clearly show cells that where the plasma membrane was totally destroyed by microbubbles induced by the laser pulse.

Fig. 5.10. Qualitative comparison of experimental data (main figure) with results from theoretical model in equation 5.2 (inset figure). Reasonable agreement between the model and experiments for fluences lower than 0.6 J/cm^2 is observed. Both curves increase linearly with fluence.

Fig A.1 Absorption coefficient of Direct Red in aqueous solution at λ=532 nm as a function of the dye concentration. Linear fit equation is y=0.0564x+1.6945. Experimental data was acquired using a photospectrometer.

Fig A.2 Equivalent electric circuit of a PVDF transducer. It can be modeled as a current source in parallel with a capacitor, internal resistance (both intrinsic) and a load resistance (either 50Ω or 1 M Ω).

Fig A.3 Set up for calibrating the PVDF sensor. The PVC cuvette contains the Direct Red solutions.

Fig A.4 Schematic of ETP system

List of Tables

List of Symbols

A	Constant that depends on laser pulse duration
C_p	Specific heat [J/Kg K]
C_s	Speed of sound [m/s]
d_0	Beam diameter [m]
F	Laser fluence [J/cm^2]
g	Anisotropy
I	Light intensity or irradiance [W/cm^2]
I(z)	Irradiance at a distance z [W/cm^2]
I_0	Incident light irradiance [W/cm^2]
k	Thermal conductivity [W/m K]
P	Pressure [Pa]
Q_g	Generated heat or volumetric energy density [W/m^3]
S	Hugniot coefficient
T	Temperature [^oC]
t	Time [s]
U	Shock wave velocity [m/s]
z	distance in the optical axis direction [m]
α	Thermal diffusivity [m^2/s]
β	Volumetric expansion coefficient [1/K]
Γ	Grüneisen coefficient $\beta C_s/C_p$
δ	Penetration depth [m]
δn	Refractive index change
δn_{max}	Maximum refractive index change

δp	Pressure change [Pa]
ΔT_{max}	Maximum temperature increment [^{o}C]
$\delta \Phi_{max}$	Maximum phase change
λ	Wavelength [m]
λ_{int}	Wavelength of interferogram [m]
μ_a	Linear absorption coefficient [m^{-1}]
μ_{eff}	Effective attenuation coefficient
μ_s	Scattering coefficient [m^{-1}]
μ_s'	Reduced scattering coefficient [m^{-1}]
μ_t	Attenuation of extinction coefficient [m^{-1}]
μ_t'	Reduced attenuation coefficient [m^{-1}]
ρ	Density [Kg/m^3]
σ_p	Peak thermoelastic stress [Pa]
τ	Thermal relaxation time [s]

Chapter 1: Introduction

Biomedical engineering is the application of engineering principles and technologies to the medical field. This field seeks to close the gap between engineering and medicine. It combines the design and problem solving skills of engineering with medical and biological sciences to improve healthcare diagnosis and treatment. It is a very broad field that encompasses a variety of engineering disciplines and life sciences[1].

In particular, my doctoral work encompasses studies in biomedical optics, which is the branch of biomedical engineering that focuses on the mechanisms of interaction of electromagnetic waves with tissues and cells, mainly wavelengths in the ultraviolet (UV), visible (VIS) and near infrared (NIR). As it will be presented in the following chapters, part of my work addresses engineering advances in *diagnostics*, that is, interactions where tissue affects the propagation and absorption of photons (e.g., imaging and spectroscopy of tissues and biomaterials) and another part deals with *therapeutics*, where photons affect tissue, going from relatively low energy photothermal interactions that moderately heat tissue to intense plasma-driven interactions, where pressure and shock waves may be formed [2].

Recent growth in the use of optics technology for biomedical research and health care has been explosive. New applications are made possible by emerging technologies in lasers, optoelectronic devices, fiber optics, physical and chemical sensors, and imaging, all of which are being applied to medical research, diagnostics and therapy.

Much of the motivation for this work started from the need to improve the therapeutical outcome of several vascular lesions like Port-wine stain (PWS), hemangiomas, and telangiectasias [3]. These lesions are abnormal blood vessels localized below the epidermis. The objective of these treatment is to increase the temperature of the targeted blood vessels to the coagulation temperature; once the blood vessel is coagulated the human body heals the affected zone as any other injury [4]. The principle behind the use of laser light for this purpose is based on the theory of photothermolysis [5], which was developed in the mid-

80's. Selective photothermolysis describes energy deposition to subsurface chromophores when three essential conditions are met: (1) a wavelength that reaches and is preferentially absorbed by the desired target structures, (2) an exposure duration is less than or equal to the time necessary for cooling of the target structures, and (3) sufficient energy is delivered to reach a threshold temperature for damage in the target structures [3,5]. For blood vessel damage, it is critical that the laser wavelength that is used is selectively absorbed by the blood vessel. Therfore, the light must first propagate through the epidermis, dermis and then into the vessel where the photons are absorbed. The epidermis always absorbs some energy and, if not controlled, may result on unintended burns due to heating. To overcome this problem, pulsed laser therapy has been combined with cryo-spray cooling (CSC) [6-8] and vacuum suction cups [9,10]. The first aims at pre-cooling the epidermis before a laser pulse is delivered, so that by the time the laser pulse is incident on the skin surface, the temperature in the epidermis is low enough that it is maintained to a safe value while and after a laser pulse is delivered. The second is aimed at increasing the volume fraction of blood within the blood vessel, so laser light absorption is increased, which aids efficiency.

While this approach of of milli- to micro-second long laser pulses with CSC has achieved partial success treating vascular lesions in skin surgery, it has been proven that some of the vasculature remains unaffected after the laser treatment. The blood vessels that remain are the smaller blood vessels which have a thermal relaxation time shorter than the laser pulse duration, therefore, the energy delivered by such laser pulses diffuses away to the surrounding tissue before its entire energy can be coupled to the blood vessel and its temperature never achieves the coagulation temperature. Under this perspective, my hypothesis is that short laser pulses offer a possibility to complete the treatment for small blood vessels. Coupling enough energy to the blood vessels in a time shorter than the vessel thermal relaxation time can induce the required temperature increment for coagulation.

Another interesting aspect of my work on laser-tissue interactions that led to the last project of my PhD studies, and the one related to laser diagnostics, is based on photoacoustic detection. When tissue increases its temperature, as any other material, it experiments thermal expansion. When the thermal expansion occurs very fast, the expanded hot material pushes the surrounding cold material launching a

pressure wave. Further propagation of such pressure waves may create tensile waves and shear stresses capable of causing sound wave propagation but also, in some cases, phase changes with moderate temperature increments and tissue tearing. Such mechanical responses play a significant role in tissue ablation and are worthy to be studied because they lead to desired or undesired effects [11-14].

A practical and current problem in medicine still is the early diagnosis of cancer. Cancer cells are genetically modified cells that grow as tumors at a specific organ. As the tumor grows, cells break off and travel through the circulatory and lymphatic systems to other organs precluding the appropriate operation of the organ leading the patient to death. Although cancer is curable if detected in its early stages, it is unlikely that a patient looks for help because it is a painless disease in those early stages. Therefore it is of paramount importance to develop methodologies that allow accurate, prompt cancer detection.

It has been shown that even in its early stages cancer tumors begin shedding cells into the circulatory system with distinct cell populations having the potential to develop into metastatic disease. Thus, there has been growing interest in identifying tumor cells in the circulatory system and using the outcome of the study to monitor the progression of various types of cancers. As different cancer types have different properties, several techniques have been developed for circulating tumor cell (CTC) detection; some of them are immunohystochemestry, reverse transcription polymerase chain reaction (RT-PCR) and magnetic cell sorting. However the first has been found to be time-consuming and subject to reviewer interpretation; the second removed the reviewer interpretation and increased the sensitivity, but has raised concerns due to inconsistency of results and amplification of false products and further investigation is required to fully develop the latter [15-18].

Melanoma is the least common, but the most dangerous of skin cancers. Melanoma cells distinguish from other cells because they contain great amounts of melanin. Melanin is an absorbing pigment in the ultraviolet and visible part of the spectrum [19,20]. A novel *in vitro* system for circulating melanoma cell (CMC) detection proposes to separate red blood cells from a routine blood draw in a centrifuge and pump the remaining solution through a closed loop that includes a quartz flow cell to be irradiated with

nanosecond-long laser pulses [21]. The system takes advantage of the melanin optical properties and short laser pulse duration to generate a photoacoustic signal that can be detected with a piezoelectric transducer incorporated to the quartz flow cell and connected to an oscilloscope. The amplitude of this signal is proportional to the CMC concentration in the circulatory system. However, to ensure continuous detection, is necessary to ensure that laser pulses do not break the plasma membrane so the melanin contained within the cells does not leak and thus hindering melanin detection via this photoacoustic technique. Hence, it is important and necessary to elucidate the appropriate laser parameters that ensure plasma membrane integrity and at the same time, maximize the signal-to-noise ratio (SNR) of the CMC system.

With this concrete problem in mind, in Chapter 5 I present a study of the mechanical effects produced by the second and third harmonics of Nd:YAG nanosecond-long laser pulses (355 and 532 nm) on the plasma membrane of pigmented melanoma cells. Cell survival and melanin leakage were measured post-laser irradiation and photoacoustic signals resulting from irradiation with both wavelengths were compared. Bubble formation around melanosomes was also identified as a plausible damage mechanism of the melanoma cell plasma membrane.

All of the problems addressed in this dissertation relate to medical applications, however, due to the multdisciplinary nature of this research, it would be inaccurate and pretentious on my part to claim that I have offered final solutions. For this to happen multidisciplinary work teams that include engineers, physicists, chemists, biologists and health professionals, are necessary and, generally, a great deal of collective work and holistic understanding has to be accumulated before a final product or porocedure can be taken to the bedside. My role as a mechanical engineer in such multidisciplinary work team is to contribute to the problem solution with models that allow us to better understand the light-tissue interaction mechanisms from the physics point of view.

References

1. Fournier RL. Basic Transport Phenomena in Biomedical Engineering. Philadelphia, PA: Taylor and Francis. 1999:312.

2. http://www.bme.ogi.edu/biomedicaloptics/.

3. Goldman MP, Fitzpatrick RE. Cutaneous Laser Surgery: The art and Science of Selective Photothermolysis. Almond G, editor. St. Louis: Mosby, Inc. 1999.

4. Jia WC, Aguilar G, Verkruysse W, Franco W, Nelson JS. Improvement of port wine stain laser therapy by skin preheating prior to cryogen spray cooling: A numerical simulation. Lasers in Surgery and Medicine 2006; 38(2):155-162.

5. Anderson RR, Parrish JA. Selective Photothermolysis - Precise Microsurgery by Selective Absoprtion of Pulsed Radiation. Science 1983; 220(4596):524-527.

6. Jia WC, Choi B, Franco W, Lotfi J, Majaron B, Aguilar G, Nelson JS. Treatment of cutaneous vascular lesions using multiple-intermittent cryogen spurts and two-wavelength laser pulses: Numerical and animal studies. Lasers in Surgery and Medicine 2007; 39(6):494-503.

7. Aguilar G, Diaz SH, Lavernia EJ, Nelson JS. Cryogen sparay cooling Efficiency: Improvement of port wine stain laser therapy through multiple-intermittent cyogen spurts and laser pulses. Lasers in Surgery and Medicine 2002; 31:27-35.

8. Aguilar G, Wang GX, Nelson JS. Dynamic behavior of cryogen spray cooling: effects of spurt duration and spray distance. Lasers in Surgery and Medicine 2003; 32:152-159.

9. Childers MA, Franco W, Nelson JS, Aguilar G. Laser surgery of port wine stains using local vacuum pressure: Changes in skin morphology and optical properties (part I). Lasers in Surgery and Medicine 2007; 39(2):108-117.

10. Franco W, Childers M, Nelson JS, Aguilar G. Laser surgery of port wine stains using local vaccum pressure: Changes in calculated energy deposition (part II). Lasers in Surgery and Medicine 2007; 39(2):118-127.

11. Oraevsky AA. Laser-induced acoustic and shock waves in ocular tissues: Armstrong Laboratory, Occupational and Environmental Health Directorate, Optical Radiation Division 1995.

12. Oraevsky AA, Jacques SL, Esenaliev RO, F.K. T. Pulsed laser ablation of soft tissues, gels, and aqueous solutions at temperatures below 100°C. Lasers in Surgery and Medicine 1996; 18(3):231-240.

13. Oraevsky AA, Jacques SL, Tittel FK. Mechanism of laser ablation for aqueous media irradiated under confined-stress conditions. Journal of Applied Physics 1995; 78(2):1281-1290.

14. Paltauf G, Dyer PE. Photomechanical Processes and Effects in Ablation. Chem Rev 2003; 103:487-518.

15. Cristofanilli M, Budd GT, Ellis MJ, Stopeck A, Matera J, Miller MC, Reuben JM, Doyle GV, Allard WJ, Terstappen LWMM, Hayes DF. Circulating Tumor Cells, Disease Progression, and Survival in Metastatic Breast Cancer. N Engl J Med 2004; 351(8):781-791.

16. Loberg RD, Fridman Y, Pienta BA, Keller ET, McCauley LK, S. TR, Pienta KJ. Detection and Isolation of Circulating Tumor Cells in Urologic Cancers: A Review. Neoplasia 2004; 6(4):302-309.

17. Mocellin S, Hoon D, Ambrosi A, Nitti D, Rossi CR. The Prognostic Value of Circulating Tumor Cells in Patients with Melanoma: A Systematic Review and Meta-analysis Clin Cancer Res 2006; 12(15):4605-4613.

18. Ring AE, Zabaglo L, Ormerod MG, Smith IE, Dowsett M. Detection of circulating epithelial cells in the blood of patients with breast cancer: comparison of three techniques. British Journal of Cancer 2005; 92(5):906-912.

19. http://omlc.ogi.edu/spectra/melanin/jacques.mcauliffe.gif.

20. Jacques SL, et.al. The Melanosome: Threshold temperature for explosive vaporization and internal absorption coefficient during pulsed laser irradiation. Photochemistry and Photobiology 1991; 53(6):769-775

21. Weight RM, Viator JA, Dale PS, Caldwell CW, Lisle AE. Photoacoustic detection of metastatic melanoma cells in the human circulatory system. Opt Lett 2006; 31(20):2998-3000.

Chapter 2: Theoretical Background

Laser light is an electromagnetic wave that has three characteristics that make it unique: coherence, intensity and monochromaticity. Coherent light is emitted with the same phase, frequency and polarization; laser light distinguishes from other types of light because its intensity is much higher compared with other light types; laser light has a very narrow electromagnetic spectrum, thus it is called monochromatic light. While all work according to the same general principles, they are differentiated on the basis of the medium they employ to create the laser action.

Generics about interactions between lasers and materials

Classification of lasers

Lasers can be classified according to the gain medium that emits the light or according to the operation mode. According to the gain medium there are: gas, liquid and solid state lasers. Examples of gases used as gain medium are: mixture of helium and neon, carbon dioxide, nitrogen, argon and others. Liquid lasers use colored compounds carried by a solvent that is typically pumped by other light source (maybe another laser) to produce laser light; these lasers are also known like “dye” lasers. Solid state lasers generally use a semiconductor crystal as gain medium, some examples are ruby, neodymium-doped yttrium aluminum garnet (Nd:YAG) and titanium-doped sapphire (Ti:Sapphire).

According to the operation mode, in general there are continuous wave (CW) and pulsed lasers [1]. CW lasers emit laser light continuously; a typical example is the HeNe laser pointer and Argon laser. Pulsed lasers emit pulses of light of a wide variety of pulse duration, repetition rates and wavelengths. Pulse duration can go from the millisecond to the femtosecond regime, although lasers that emit attosecond-long pulses have been built [2]. The gain medium used to make a pulsed laser may be one of the three mentioned above. There are two main mechanisms to produce pulsed lasers that emit sub-microsecond laser pulses, which are Q-switching and Mode-locking.

Laser and material parameters

The primary laser parameters that characterize the interaction between a pulsed laser and a material are: wavelength, pulse energy, pulse duration, spot size and repetition rate. Secondary laser parameters can be derived from the primary laser parameters: the laser power, fluence and irradiance are associated with the pulse energy, duration and spot size. Power is the pulse energy divided by the pulse duration; for high repetition rate burst it is possible to also incorporate the average power. Fluence is defined as the laser pulse energy divided by the cross sectional area of the laser beam, its units are [J/cm^2]. Irrradiance is the laser pulse energy divided by the laser pulse duration and the beam cross sectional area and its units are [W/cm^2] [3]. The wavelength is associated with the light frequency.

Both the temporal and spatial profile of a laser pulse can (almost always) be characterized by a Gaussian function. There are several conventions to characterize the width of the Gaussian function. One is the full width half maximum (FWHM), which is the width of the Gaussian function measured at ½ of its maximum height. Another is the width measured at $1/e^2$ of the maximum height. The convention used to measure the pulse duration and spot size must always be specified. In this work the latter is used [4].

The important material parameter that characterizes laser-matter interaction is the refractive index, which for the general case is a complex quantity. Its real part is associated with refraction and its imaginary part to the material absorption. Both parts have linear and nonlinear components which may play a significant role in the interaction, depending upon the laser irradiance applied to the material [5]. A complete description of these terms is beyond the scope of this chapter and therefore not presented.

When a laser beam is incident on a material, part of it is reflected at the surface and other part is transmitted within the bulk of the material. As the beam propagates, its intensity is attenuated due to absorption and scattering. The most important material parameter for this work is the linear absorption coefficient, which is defined as the probability per unit length that a photon is absorbed, therefore its units are [cm^{-1}] [3]. The ability of a medium to absorb electromagnetic radiation depends on a number of factors, mainly the electronic constitution of its atoms and molecules, the wavelength of radiation, the thickness of

the absorbing layer, and internal parameters such as temperature or concentration of absorbing agents and it is a function of the wavelength [1,3,6]. The distribution of energy absorbed by a material is described by the Beer-Lambert law:

$$I(z) = I_0 \exp(-\mu_a z) \tag{2.1}$$

where z denotes distance in the optical axis direction, $I(z)$ is the intensity at distance z, I_0 is the incident irradiance, μ_a is the absorption coefficient of the medium. From equation 2.1, it can be derived that:

$$z = \frac{1}{\mu_a} \ln \frac{I_0}{I(z)} \tag{2.2}$$

The inverse of the absorption coefficient μ_a is referred to as the absorption length δ, in which the intensity $I(z)$ has dropped to 1/e of its incident value I_0.

$$\delta = \frac{1}{\mu_a} \tag{2.3}$$

Scattering occurs when the photon changes its direction of propagation caused by random spatial variations in tissue density, refractive index, and dielectric constant and actual light distributions can be substantially different from distributions using Beer's law. Scattering by large particles is rather wavelength independent, whereas scattering by smaller particles is stronger at shorter wavelengths. It can be modeled by the scattering coefficient defined as the probability per unit length that a photon is absorbed and it follows a law similar to that of Beer's law:

$$I(z) = I_0 \exp(-\mu_s z) \tag{2.4}$$

Optical penetration is governed by a combination of absorption and scattering, thus an attenuation coefficient μ_t can be defined as:

$$\mu_t = \mu_a + \mu_s \tag{2.5}$$

And it is the coefficient that would govern the light attenuation in equation 2.1, which holds for isotropic materials. However for an anisotropic material, the anisotropy *g*, a measure of how much forwardness is retained after a scattering event must be considered. Thus, the reduced scattering coefficient, useful to describe diffusion of photons in a random walk step of $1/\mu_s$' rather than many steps of size $1/\mu_s$, is defined as

$$\mu_s' = \mu_s(1-g) \tag{2.6}$$

So the reduced attenuation coefficient, useful when absorption, scattering and anisotropy are present, is defined as:

$$\mu_t' = \mu_a + \mu_s' = \mu_a + \mu_s(1-g) \tag{2.7}$$

The effective attenuation coefficient, useful for very highly scattering materials such that $\mu_s << \mu_a$ is defined as:

$$\mu_{eff} = \sqrt{3\mu_a\mu_t'} = \sqrt{3\mu_a(\mu_a + \mu_s(1-g))} \tag{2.8}$$

Mechanisms of interaction between lasers and materials

The different possible mechanisms of interaction between laser pulses and matter are shown in Fig. 2.1. As the laser irradiance is inversely proportional to the laser pulse duration, the shorter the pulse the higher the irradiance. For long laser pulses in the order of milli to microseconds, laser light is absorbed by the chromophore according to Beer's law and the interaction becomes merely thermal. The heat generated upon light absorption is transferred to the surroundings of the irradiated volume via heat diffusion. As the laser pulse durations shortens to the nanosecond regime, the stress confinement conditions may be achieved and the mechanical effects associated to the rapid energy deposition play a significant role in material removal; this process is called photoablation. As the laser pulse shortens further, laser light becomes more intense and nonlinear absorption takes place leading to plasma formation. Each of the

relevant mechanisms of interaction relevant for each part of this thesis is described in the theoretical background section of each part.

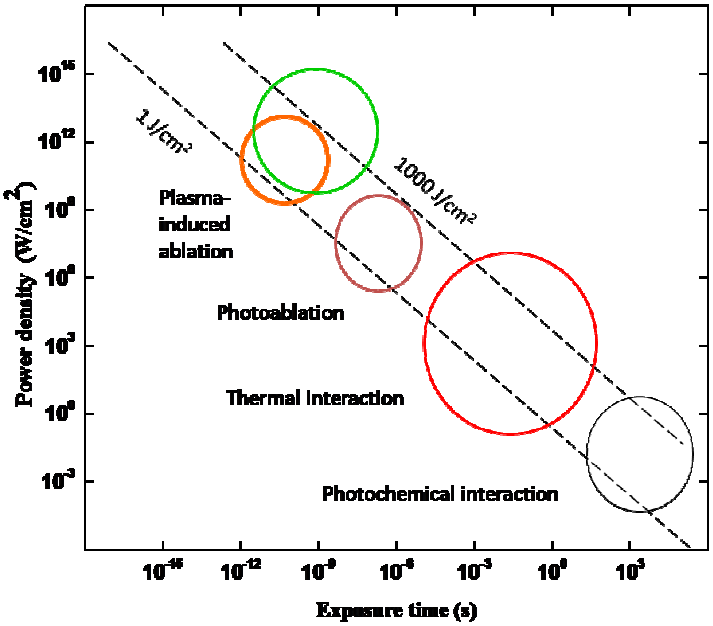

Fig 2.1. Map of the different mechanisms of interaction between laser pulses and materials as a function of both irradiance (or power density) and pulse duration (or exposure time) [7].

Photothermal interactions

For the sake of simplicity scattering events are neglected in the following paragraphs. When a laser pulse is incident on a material, its energy is coupled to the material and heat generation is produced, which can be calculated as:

$$Q_g = \mu_a F e^{-\mu_a z} \tag{2.9}$$

where Q_g is the heat generated, F is the laser fluence. The term calculated in equation 2.9 is also known as the volumetric energy density.

This heat diffuses to the surrounding material and Q_g can be introduced in the heat diffusion equation to calculate the spatial and temporal dependent temperature distribution within the material:

$$\rho C_p \frac{\partial T}{\partial t} = k\left(\frac{\partial^2 T}{\partial x^2} + \frac{\partial^2 T}{\partial y^2} + \frac{\partial^2 T}{\partial z^2}\right) + Q_g \tag{2.10}$$

where ρ, C_p and k are the material's density and specific heat and thermal conductivity respectively.

The thermal relaxation time τ is the time required for the heat to diffuse away a characteristic length. The thermal relaxation time for a layer if thickness δ is defined as:

$$\tau = \frac{\delta^2}{\alpha} = \frac{\rho C_p \delta^2}{k} \tag{2.11}$$

where α is the thermal diffusivity.

When the laser pulse is shorter than the thermal relaxation time, there is no time for the heat to diffuse away from the irradiation volume and the maximum temperature is achieved at the material surface. Such condition is called thermal confinement. The maximum temperature increment ΔT_{max} that can be achieved under thermal confinement conditions given by:

$$\Delta T_{\max} = \frac{\mu_a F}{\rho C_p} \tag{2.12}$$

Temperature increments lead to different effects, such as melting, vaporization, carbonization, chemical effects, etc. depending on the type of material. In the case of biological tissues, temperature increments and may lead to protein thermal denaturation and tissue coagulation.

Fig. 2.2 shows a schematic of the photothermal-matter interactions, where the role of both laser parameters and material properties can be distinguished:

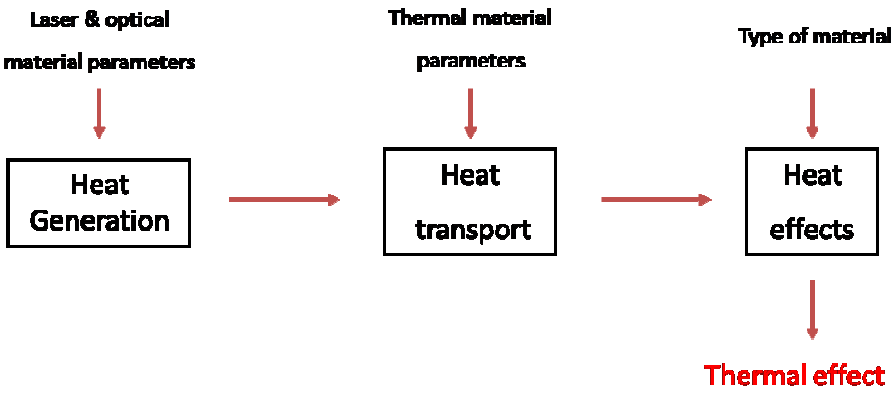

Fig. 2.2. Diagram of thermal interactions between laser pulses and materials. Laser parameters and material optical properties drive heat generation, while the material thermal properties determine heat transport throughout the irradiated material. The type of material determines the possible thermal damage.

Photothermomechanical interaction

While the material's temperature increases as a result of laser light absorption, it goes through a rapid thermoelastic expansion. When laser irradiation happens under thermal confinement conditions, the irradiated volume is heated under an isochoric process. The thermoelastic expansion of the hot material surrounded by cold material creates a pressure wave. Thermoelastic stresses are most prominent when the laser pulse is shorter than the characteristic time for a stress wave to propagate across the heated volume. This condition is known as stress confinement. In contrast, when the laser pulse is comparable or longer than the characteristic time for stress wave propagation, significant expansion of the laser-heated volume occurs during the laser pulse. This has the effect of reducing the stress peak. The peak thermoelastic stress σ_p is given by:

$$\sigma_p = A\Gamma\mu_a F \tag{2.13}$$

where Γ is the Grüneisen coefficient and A depends on the laser pulse duration. The Grüneisen coefficient is a thermophysical property of the material defined as the internal stress per unit energy density generated upon depositing energy into a target under constant volume conditions.

$$\Gamma = \frac{\beta C_s^2}{C_p} \tag{2.14}$$

where β is the volumetric expansion coefficient, *Cs* is the speed of sound. Physically, it represents the portion of the optical energy converted into mechanical energy. The Grüneisen coefficient of water varies with temperature; it equals 0.11 at 20 ^{o}C, 0.125 at 25 ^{o}C and 0.5 at 100 ^{o}C. The constant $A=1$ when stress confined conditions are fulfilled and $A<1$ otherwise [8].

Laser induced pressure waves have been studied experimentally using two main tools. The first is a piezoelectric transducer such as polyvinylidene fluoride (PVDF) and lithium niobate ($LiNbO_3$), which signal may be sent to an amplifier and then read in an oscilloscope [9-11]; the second is either Michelson or Mach-Zenhder interferometry[12-15].

Depending on the experimental conditions, these pressure waves have been found to be of significance in inducing phase change in water, a common model for laser-tissue interactions research, below 100 ^{o}C [9,10]. Fig. 2.3 shows the typical studied case when a nanosecond-long laser pulse is incident on a material with absorption coefficient $\mu_{a.}$ where the resulting pressure wave is detected with a piezoelectric transducer at a certain distance away from the interaction region.

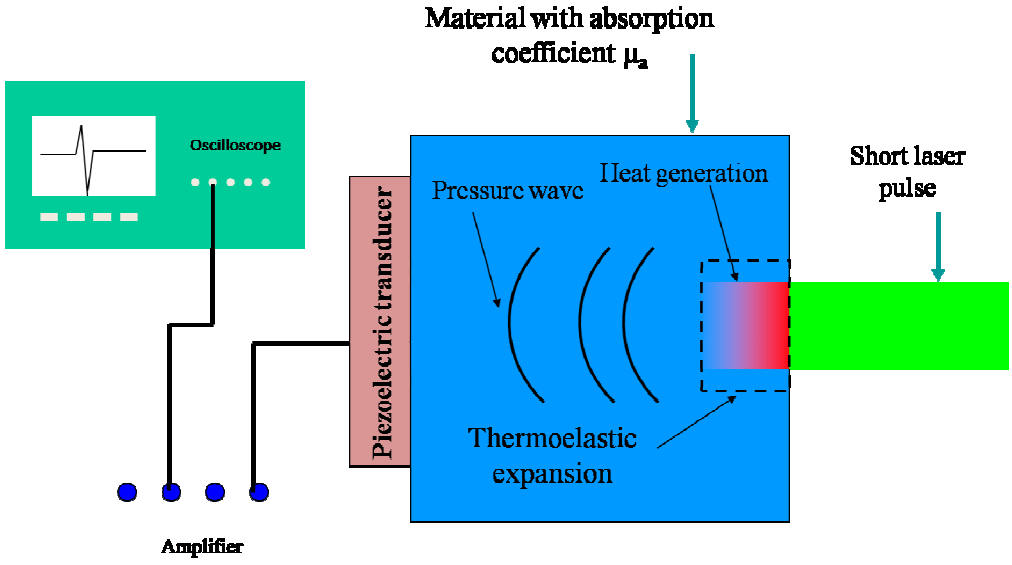

Fig. 2.3. Typical photoacoustic experiment where a laser pulse is absorbed by a material with absorption coefficient μ_a. The material experiments a thermoelastic expansion that results in the emission of a pressure wave. The pressure wave can be detected by a piezoelectric transducer and its signal recorded in an oscilloscope.

When the laser pulse is absorbed by the material, the resulting pressure wave shape depends on the beam diameter d_0 and the material absorption coefficient μ_a. If $d_0 > 1/\mu_a$, it results in a plane wave propagating parallel to the optical path; in contrast, when $d_0 < 1/\mu_a$ it results a cylindrical wave propagating in radial direction, perpendicular to the optical path [16].

In the first case, when $d_0 > 1/\mu_a$, a plane compressive wave parallel to the laser beam, propagates in both directions. The compressive wave propagating in opposite direction to the laser beam encounters an acoustic mismatch at the material-air interface due to the lower acoustic impedance of air. As a consequence, a tensile wave is reflected and propagates in the optical path direction following the compressive component [9-11,17]. When the irradiated material is water, which absorption coefficient has been increased with some absorbing dye, the low pressure (tensile wave), together with moderate temperature increments produce micro-cavitation bubble formation [9,10].

Photoablation

The combination of high pressure waves originated at the surface of a laser irradiated linearly absorbing medium with photochemical and photothermal decomposition that weakens the material within the irradiation volume, results in material ejection producing material ablation (material removal) [1,8]. Photoablation was first studied in several polymers and soon after biological tissues were ablated. It is the principle in which refractive cornea surgery is based to correct the refractive power of the cornea to correct myopia, hyperopia or astigmatism [1].

In the case of collagen-rich biological tissues, such as cornea, the main chromophore for UV light is the collagen fibrils that constitute the extracellular matrix, which is the structure that gives strength to the tissue. Photoablation with UV laser of such tissues produces very clean ablation compared to IR radiation, where the main chromophore is the water contained in the tissue and stress confinement is not totally fulfilled.

UV-light absorption results in heat generation in the fibrils that is transferred to the rest on the tissue structures with typical temperature increments likely go beyond 100 ^{o}C with its subsequent thermal denaturation. Furthermore, UV light produces scission of the chemical bonds between the biomolecules, which results in photochemical denaturation of the tissue structures. Both types of denaturation contribute to the photoablation process weakening the extracellular matrix, which together with the stress transients produced by the fast energy deposition enhance material ejection. In contrast, the main chromophore for IR photoablation is the water contained in the tissue from where heat is transferred to the rest of the tissue structures. Because UV radiation destroys the extracellular matrix, compared to IR radiation due to the photochemical process involved, photablation with UV light occurs faster and results in a cleaner surface ablation [8,18].

Bubble and pressure wave formation around laser heated microabsorbers

An important application case in selective retina treatment (SRT), selective laser trabeculoplasty (SLT) as well as in other biomedical procedures such as nanoparticle assisted cellular surgery and selective cell killing is the case of laser heated spherical microabsorbers. Technical applications comprise bubble jet printer technologies, steam laser cleaning, bubble induced optical limiting in suspensions, transient holographic gratings, bubble mediated fast optical switching [19] and references therein.

Retina and some skin types contain major amount of melanin, which is high absorbing chromophore in the whole UV and VIS spectrum. Melanin is contained within cells in the melanosomes which are spherical shaped organelles 1 μm in diameter approximately [20].

The thermal relaxation time of a 1 μm melanosome with 1.37×10^{-7} m^2/s thermal diffusivity is 7.3 μs. So when a submicrosecond-long laser pulse is used to irradiate melanosomes, thermal confinement is fulfilled, thus the temperature increment on the surface of the melanosome can be calculated according to equation 2.12. When the melanosome has absorbed the laser energy and a maximum temperature has been achieved, the melanosome experiments thermoelastic expansion and launches a pressure wave. Then heat is transferred to the layer of water (cytoplasm) adjacent to the melanosome and temperature in the water increases as fast as 10^{10} K/s and may be as high that it is vaporized forming a cavitation/boiling bubble. As the bubble expands, it interacts with the plasma membrane and causes disruptive effects of the cell. This case is treated in detail in Chapter 5.

Plasma mediated ablation

When a very intense laser pulse interacts with some material, the intense electric field initiates ionization via thermionic emission for nanosecond laser pulses or multiphoton ionization for pico or femtosecond laser pulses releasing electrons from existing atoms. Free electrons serve as photon absorbers that collide with other atoms releasing more electrons that at the same time continue absorbing more

photons. This continuous process is known as avalanche ionization. As a consequence of the ionization processes, a phenomenon called *optical breakdown* or *plasma formation* occurs at irradiances of the order of 10^{14} W/cm^2 in air and 10^{11} W/cm^2 for solids and liquids[1,8,21,22]. Such high irradiances are easily achieved with a 6 ns laser pulse with few hundreds of microjoules of energy focused through a 0.5 NA lens [23]; even a few nanojoules of energy are enough to produce optical breakdown in water with a focused beam of femtosecond laser pulses [22,24].

Plasma formation induces a sudden, adiabatic temperature rise of the order of 10, 000 K in the focal volume due to the energy of free electrons. Because of its high kinetic energy, electrons diffuse into the surrounding medium [8,21,22]. When the inert ions follow at a certain time delay mass is moved and a shock wave separates from the boundary of the plasma. It initially moves at supersonic speed and then decelerates to sonic speed [1,8,22,25-27].

When plasma is induced in the bulk of a fluid or gel, water or agar for example, the material occupying the focal volume is vaporized and work is done over the non vaporized material and the kinetic energy is stored as potential energy in the expanding bubble. After its expansion the bubble collapses due to the static pressure and launches another shockwave. The process may repeat a few times before the total energy is dissipated and the gasses dissolve in the surrounding fluid [1,8,14,23,25-29]. The bubble formation upon plasma formation constitutes the principle under which tissue cutting relies on for cornea surgery.

The complex flow field originated in the vicinity of a solid wall due to an oscillating plasma-generated oscillating bubble produces shear stresses that have been used to induce specific molecular delivery to cells [30-32]. The basic idea of these studies was to induce a bubble in the culturing medium (seeded with an specific molecule) of a cell monolayer, so the shear stresses resulting from the fluid movement-solid boundary interaction stretch the cells plasma membrane, creating porous through which molecules can get into without killing the cells. This is an important application in biotechnology.

Plasma mediated ablation of materials results in a very clean ablation with evidence of minimal thermal and mechanical damage next to the focal volume if the appropriate laser parameters are chosen [33-38]. This capability has taken an importance for micro-processing of materials where a surface micropatterning is desired.

References

1. Niemz M. Laser-Tissue Interactions: Fundamentals and Applications. New York: Springer. 2002.

2. Paul PM, Toma ES, Breger P, Mullot G, Auge F, Balcou P, Muller HG, Agostini P. Observation of a Train of Attosecond Pulses from High Harmonic Generation Science 2001; 292:1689-1692.

3. Goldman MP, Fitzpatrick RE. Cutaneous Laser Surgery: The art and Science of Selective Photothermolysis. Almond G, editor. St. Louis: Mosby, Inc. 1999.

4. Siegman AE. How to (maybe) measure laser beam quality. OSA TOPS 1998; 17:184-199.

5. Rangel-Rojo R. Optica Nolineal: CICESE class notes. 2004.

6. Welch AJ, Gemert MJCv. Optical-thermal response of laser-irradiated tissue. Kogelink H, editor. New York: Plenum press. 1995. 925 p.

7. Boulnois JL. Photophysical processes in recent medical laser developments: a review. Lasers Med Sci 1986; 1:47-66.

8. Vogel A, Venugopalan V. Pulsed laser ablation of biological tissue. Chemical Reviews 2003; 103:577-644.

9. Oraevsky AA, Jacques SL, Esenaliev RO, F.K. T. Pulsed laser ablation of soft tissues, gels, and aqueous solutions at temperatures below 100°C. Lasers in Surgery and Medicine 1996; 18(3):231-240.

10. Oraevsky AA, Jacques SL, Tittel FK. Mechanism of laser ablation for aqueous media irradiated under confined-stress conditions. Journal of Applied Physics 1995; 78(2):1281-1290.

11. Paltauf G, Dyer PE. Photomechanical Processes and Effects in Ablation. Chem Rev 2003; 103:487-518.

12. Hobley J, Kuge Y, Gorelik S, Kasuya M, Hatanaka K, Kajimoto S, Fukumura H. Water expansion dynamics after pulsed IR laser heating. Phys Chem Chem Phys 2008; 10:5256-5263.

13. Kim B, Feit MD, Rubenchick AM, Joslin EJ, Celliers PM, Eichler J, Da Silva LB. Influence of pulse duration on ultrashort laser pulse ablation of biological tissues. Journal of Biomedical Optics 2001; 6:332-338.

14. Kim B, Komashko AM, Rubenchick AM, Feit MD, Reidt S, Da Silva LB, Eichler J. Interferometric analysis of ultrashort pulse laser-induced pressure waves in water. Journal of Applied Physics 2003; 94:709-715.

15. Martí-López L, Ocaña R, Porro JA, Morales M, Ocaña JL. Optical observation of shock waves and cavitation bubbles in high intensity laser-induced shock processes. Applied Optics 2009; 48:3671-2380.

16. Oraevsky AA. Laser-induced acoustic and shock waves in ocular tissues: Armstrong Laboratory, Occupational and Environmental Health Directorate, Optical Radiation Division 1995.

17. Viator JA, Jacques SL, Prahl S. Depth profiling of absorbing soft materials using photoacoustic models. IEEE Journal of selected topics in quantum electronics 1999; 5(4):989-996.

18. Apitz I, Vogel A. Material ejection in nanosecond Er:YAG laser ablation of water, liver, and skin. Appl Phys A 2005; 81:329-338.

19. Neumann J, Brinkmann R. Nucleation dynamics around single microabsorbers in water heated by nanosecond laser irradiation. Journal of Applied Physics 2007; 101(11):114701-114709.

20. http://omlc.ogi.edu/spectra/melanin/jacques.mcauliffe.gif.

21. Vogel A, Nahen K, Theisen D, Noack J. Plasma Formation in Water by Picosecond and Nanosecond Nd:YAG Laser Pulses-Part I: Optical Breakdown at Threshold and Superthreshold Irradiance. IEEE Journal of Selected Topics in Quantum Electronics 1996; 2(4):847-860.

22. Vogel A, Noack J, Hutmann G, Paltauf G. Mechanisms of femtosecond laser nanosurgery of cells and tissues. Appl Phys B 2005; 81:1015-1047.

23. Evans R, Camacho-López S, Pérez-Gutiérrez FG, Aguilar G. Pump-probe imaging of nanosecond laser-induced bubbles in agar gel. Opt Express 2008; 16(10):7481-7492.

24. Vogel A, Linz N, Freidank S, Paltauf G. Femtosecond-Long-Induced Nanocavitation in Water: Implications for Optical Breakdown Threshold and Cell surgery Physical review letters 2008; 100:038102-038101-038102-038104.

25. Fischer JP, Juhasz T, Bille JF. Time resolved imaging of the surface ablation of soft tissue with IR picosecond laser pulses. Appl Phys A 1997; 64:181-189.

26. Vogel A, Busch S. Shock wave emission and cavitation bubble generation by picosecond and nanosecond optical breakdown in water. J Acoust Soc Am 1996; 100(1):148-165.

27. Vogel A, Lauterborn W, Timm R. Optical and acoustical investigations of the dynamics of laser-produced cavitation bubbles near a solid boundary. J Fluid Mech 1989; 206:299-338.

28. Brujan EA, Vogel A. Stress wave emission and cavitation bubble dynamics by nanosecond optical breakdown in a tissue phantom. J Fluid Mech 2006; 558:281-308.

29. Vogel A, Lauterborn W. Acoustic transient generation by laser-produced cavitation bubbles near solid boundaries. J Acoust Soc Am 1988; 82(2):719-731.

30. Dijkink R, Gac SL, Nijhuis E, Berg Avd, Vermes I, Poot A, Ohl CD. Controlled Cavitation-cell interaction: trans-membrane transport and viability studies. Phys Med Biol 2008; 53:375-390.

31. Hellman AN, Rau KR, Yoon HH, Venugopalan V. Biophysical response to pulsed laser microbeam-induced cell lysis and molecular delivery. J Biophoton 2007; 1:24-35.

32. Rau KR, Quinto-Su PA, Hellman AN, Venugopalan V. Pulsed Laser Microbeam-Induced Cell Lysis: Time-Resolved Imaging and Analysis of Hydrodynamic Effects. Biophysical Journal 2006; 91:317-329.

33. Cummings JP, Jr. JTW. Tissue tearing caused by pulsed laser-induced ablation pressure. Applied optics 1993; 32:494-501.

34. Horneffer V, Linz N, Vogel A. Principles of laser-induced separation and transport of living cells. J of Biomedical Optics 2007; 12:054016-054011 - 054016-054013.

35. Lenzer M, Kruger J, Sartania S, Cheng Z, Spielman C, Mourou G, Kautek W, Krausz F. Femtosecond Optical Breakdown in Dielectrics. Physical Review Letters 1998; 80:4076-4079.

36. Lu J, Xu RQ, Chen X, Shen ZH, Ni XW, Zhang SY, Gao CM. Mechanisms of laser drilling of metal plates underwater. Journal of Applied Physics 2004; 95:3890-3894.

37. Venugopalan V, III AG, Nahen K, Vogel A. Role of Laser-Induced Plasma Formation in Pulsed Cellular Microsurgery and Micromanipulation. Physical Review Letters 2002; 88(078103):1-4.

38. Vogel A, Lorenz K, Horneffer V, Huttmann G, Smolinski Dv, Gebert A. Mechanisms of Laser-Induced Dissection and Transport of Histologic Specimens. Biophysical Journal 2007; 93:4481-4500.

Chapter 3: Short and Ultrashort Laser Pulse Induced Bubbles on Transparent and Scattering Tissue Models

Introduction

Since its invention, the laser has been widely used for many applications in the field of medicine; both continuous wave (CW) and pulsed lasers are suitable for medical applications [1-11]. The physical mechanisms involved in a laser-matter interaction depend, aside from wavelength, on the pulse intensity, which itself depends on the laser pulse duration; the shorter the pulse the higher the peak intensity [12,13]. Long laser pulses (μs to ms) couple its energy to the material mainly through the wavelength-dependent linear absorption, according to an extinction coefficient (μ_t); most of the energy deposited to the material produces heat and, therefore, the interaction is dominated by heat diffusion. When the laser pulse is very intense, a fast optical and avalanche ionization process dominates the interaction and an expanding plasma is produced with very small amount of heat transferred to the targeted material. Ultrashort laser-matter interactions are, to a certain degree, wavelength-independent. While for certain transparent materials like glass there exist two distinctive "and definite trends" for the damage threshold fluence of the material for laser pulse durations above and below 10 ps [14], the boundary between long and ultrashort pulses is not very well established in the context for all materials, particularly biological ones.

Long laser pulses (ms to μs) at convenient wavelengths have been incorporated to laser surgeries where the aim is to produce thermal (by laser heating) treatment of specific chromophores and/or tissue ablation [15]. However, there are specific cases where the treatment is not totally successful; as an example, Port Wine Stain (PWS) birthmarks are an abnormal layer of blood vessels 10 to 100μm in diameter localized 100 to 500 μm below the skin surface, that have been treated using long (1 to 2ms) laser pulses in combination with Cryogen Spray Cooling (CSC) [16-21]. The aim of this treatment is to achieve the temperature at which blood in the vessel coagulates at the same time that the other chromophores in the skin remain undamaged; this treatment has proved success with large blood vessels (~100 μm) because they have a long thermal relaxation time (5ms) that allows thermal confinement in the blood vessel, hence

achieving the coagulation temperature; in contrast, smaller blood vessels (10μm) have shorter thermal relaxation time (50μs), which does not allow sufficient thermal confinement, hence the laser heat produced during the pulse quickly diffuses away to the surrounding tissue before the coagulation temperature is achieved and the blood vessel remains undamaged. A feasible solution for this problem is the use of shorter (nano, pico to femtosecond) laser pulses that deliver its energy faster than the thermal relaxation time of those small vessels. My work in this area intended to evaluate if this approach would be feasible, but also to explore if additional mechanical phenomena could be triggered by the laser-tissue interaction such as cavitation and shockwaves, which might also contribute to the damage and elimination of the very small blood vessels which are difficult to remove by slow laser heating.

Several researchers have looked at the effects of nano, pico and femtosecond laser pulses in biological materials, such as skin, liver, cornea and retina and water used as tissue model [22]. However there is no evidence that nanosecond laser pulses have been used to destroy blood vessels.

Given the complexity of a biological system that incorporates a blood vessel, and that the purpose of the work is to study the physical mechanisms of interaction between nanosecond laser pulses and blood vessels, I first worked with artificial tissue models that mimic real tissue in a more realistic way than pure water.

Several authors have observed that when submicrosecond laser pulses are focused on aqueous media a bubble is formed its diameter and lifetime strongly depend on the laser parameters and material properties, but the conditions for bubble formation must be determined in each individual case. There are three different possible mechanisms for bubble formation: (1) optical breakdown, (2) refraction wave and (3) overheating of the material. In this part of the work I focused in the optical background.

When a bubble is formed in an elastic media, such as agar gels, the bubble expands and collapses several times before disappearing, however, when the plasma is very intense, the pressure inside the bubble may be so high that it plastically deforms the material producing a permanent bubble, in other words, a bubble that does not expand a collapse.

The threshold fluence for plasma formation is the fluence at which there is 50% probability that plasma is formed. This threshold depends on the laser pulse peak irradiance. When a laser beam is focused in the bulk of a material, it loses some energy as it propagates through because of absorption and scattering, reducing the local irradiance at the focal point.

It is important to find out the laser parameters that lead to plasma formation that generates a cavitation bubble in a particular material. Such bubbles can serve as photodisruption mechanism for the small blood vessels that remain after traditional laser surgery with longer laser pulses.

In the initial stage of the work, experiments focusing a 5 ns, Nd:YAG laser beam on agar gel artificial tissue models (phantom) were carried out [23,24]. The threshold fluence for bubble formation was found for different absorption coefficients when the laser beam was focused at a specific depth below the surface; also, the characterization of the bubble diameter as a function of fluence was carried out for several samples with different absorption coefficients, however, only permanent bubbles were studied.

Addition of dyes and intralipids in different concentrations to agar gels allows to make a more realistic skin model. In the present work the main objectives are to study the bubble dynamics, i.e., its formation and evolution when a series of pulses at three different repetition frequencies are delivered using a fluence value close to the threshold fluence and, to find the threshold fluence for bubble formation in a scattering tissue model. The last study intends to mimic a highly scattering tissue, like skin. These experiments were carried out using a 532 nm, Nd:YAG laser, pulse duration of 5 nanoseconds and a 90 femtosecond laser.

Materials and Methods

Artificial Tissue Models

Agar is typically a strong gelling polysaccharide derived from red seaweeds. Agar solutions gel due to the presence of the agarose fraction of the crude agar at common concentrations between 0.5 and

2.0%. Agar typically needs to be heated above 90 ºC to liquify (melt) and depending on the seaweed source the setting temperature can be between 30 and 45 ºC. As agar gels are mainly conformed by water, they are an excellent material to make artificial tissue phantoms. They may also be combined with other substances to approximate its optical properties to more realistic tissue[24,25]. In this work, two types of agar phantoms were used. Figure 3.1 shows the first model, which is made of a single 500 µm thick layer of transparent agar, it was used for the experiments where the bubble dynamics were studied for different number of pulses and repetition rates. Note that the beam was focused 100µm below the surface, a typical depth at which a blood vessel can be found. Figure 3.2 shows the second model, which we used to study the bubble formation in a highly scattering medium. It is composed of two layers. The top 254 µm thick layer, the scattering one, is constituted by a mixture of liquid agar gel and 4.8% intralipid; the scattering layer was stacked on top of another layer made of transparent agar gel. For this case the laser beam was focused at 50, 100 and 200 µm deep in the scattering layer.

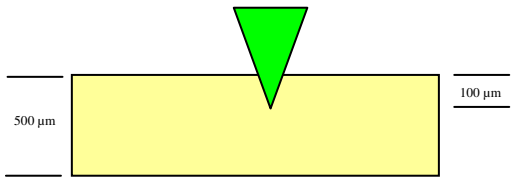

Fig. 3.1. 500 µm thickness transparent agar single layer.

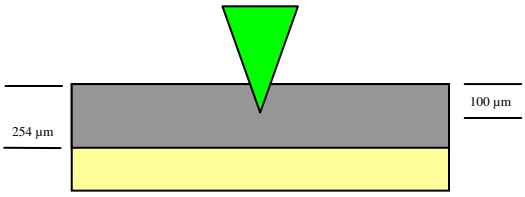

Fig. 3.2. Highly scattering agar layer stacked on top of another layer of transparent agar.

Experimental setup and bubble detection

The experimental set up is shown in Figure 3.3. It can be used in a configuration that includes both a 532 nm, Nd:YAG, 5 nanosecond pulses as well as a 810 nm, Ti:Sapphire, femtosecond as excitation beams and a 632.8 nm HeNe continuous wave laser as probe beam, which are focused on the target with a 0.5 NA, 8 mm focal length aspherical lens that we will call the microprocessing lens. The energy per pulse delivered on target is monitored either with a properly calibrated photodiode and an oscilloscope or directly with an energy head detector. A CCD camera is used to capture the image of the focused beam on the

target; this is done by using an image relay system constituted by the microprocessing lens and the 500mm lens shown in Fig. 3; the light that reflects backwards from the surface is collected by the two lenses projecting an image of the beam waist onto the CCD. This image relay system provides three very useful features to our set up: (1) it requires normal incidence to work so that the sample surface is always perpendicular to the incident beam, and therefore, in the event of a transversal scan of the sample the beam waist of the focusing light stays always at a constant distance from the surface; (2) it allows fine positioning of the beam waist right on the surface of the sample, and hence at a known depth within the layer, with a resolution of the order of the Rayleigh range of the focusing beam, and; (3) the same image relay system allows to record movies of the bubble formation and evolution inside the agar gel. The bubble formation dynamics is also recorded by use of the HeNe probe beam; the light transmitted through the sample is collected onto a photodiode connected to a data acquisition system. If the bubble is not present, the HeNe light detected by the photodiode produces a constant signal, however, when the bubble forms the initial constant signal drops to a minimum (when the bubbles reaches its maximum diameter) and it recovers back up as the bubble collapses.

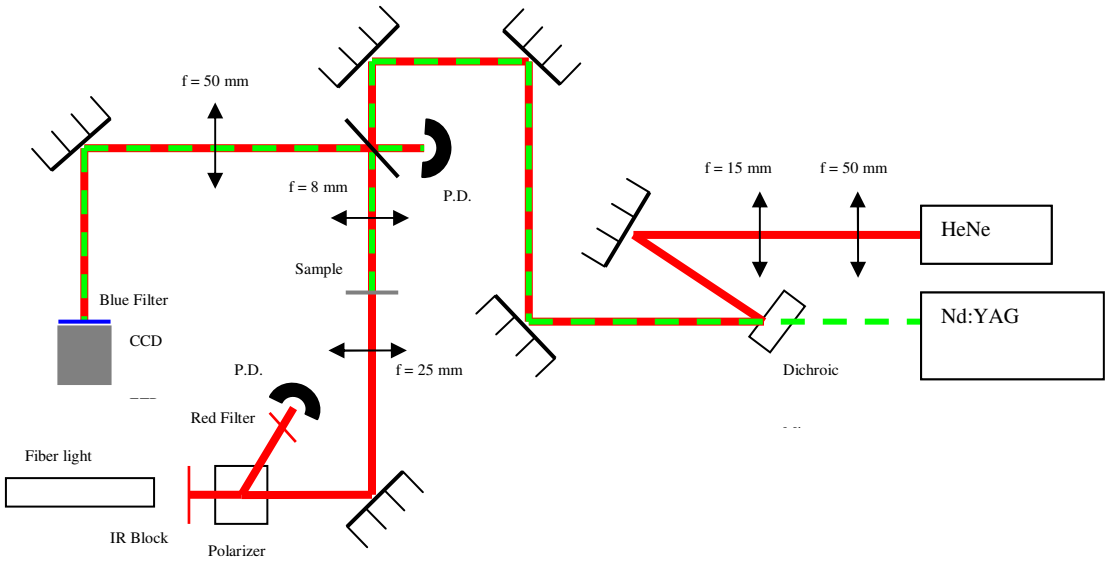

Fig. 3.3. Experimental Setup for cavitation bubble visualization in agar gels.

Image processing

Movies of the laser-induced bubbles were taken at 10 frames per second and split into several pictures. The diameter of the bubble was measured for a selected number of pictures using a standard image processing software (ImageJ). Figure 3.4 shows a typical sequence of photos of the bubble image obtained on the CCD camera.

Results and discussion

Bubble dynamics

Figures 3.5 to 3.9 contain experimental results of laser irradiation of agar gel models with laser pulses of 5ns duration, at a wavelength of 532 nm, on a 500 μm thick transparent layer. The beam was focused 100μm deep in the agar gel layer. The data point plotted at t=0 represents the diameter of the bubble right after the last pulse. All these experiments were carried out with fluence slightly smaller than that for the bubble formation threshold (240 J/cm^2) for permanent bubbles (220.6 ± 9.6 J/cm^2) such that we could generate the transient bubbles we are interested in; the fluence values shown in figures 5 to 9 correspond to the average fluence value of the total number of pulses applied.

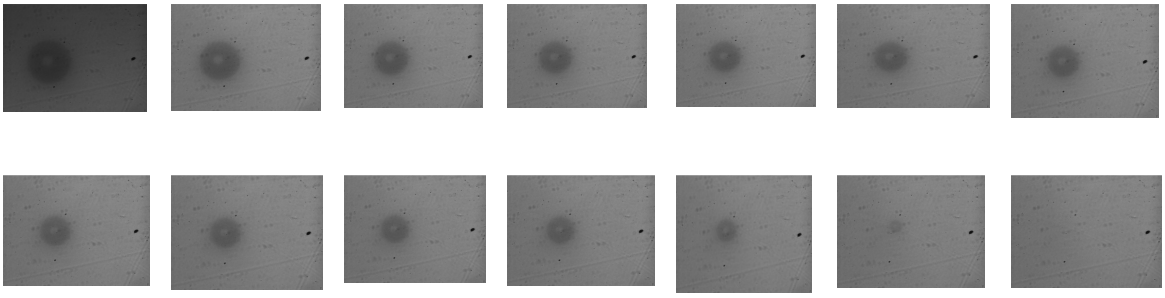

Fig. 3.4. Typical sequence of photos that describe how the bubble diameter changes with time. The bubble was obtained by using a single 5 ns (532nm) Nd:YAG laser pulse with fluence of 204.65 J/cm^2. Upper row (left to right): 0 s, 0.4 s, 1.06 s, 1.73 s, 2.4 s 3.06 s, 3.77 s. Lower row (left to right): 4.4 s, 5.06 s, 5.73 s, 6.4 s, 9.7 s, 13.06 s, 15.5 s.

Figure 3.5 shows the time evolution from maximum bubble diameter when a single laser pulse is applied, each curve corresponds to different applied fluences, which are in fact obtained from the inherent fluctuation of the laser system. Except for one case (199.16 J/cm^2), it was found that the higher the fluence,

the bigger the bubble and the longer the life-time. The case that falls off the typical trend seen for the other cases might be explained by an inhomogeneous agar gel sample. This is also suggested by the fact that for some experiments the bubble was not formed. Figure 5 shows only the cases where the bubbles were formed.

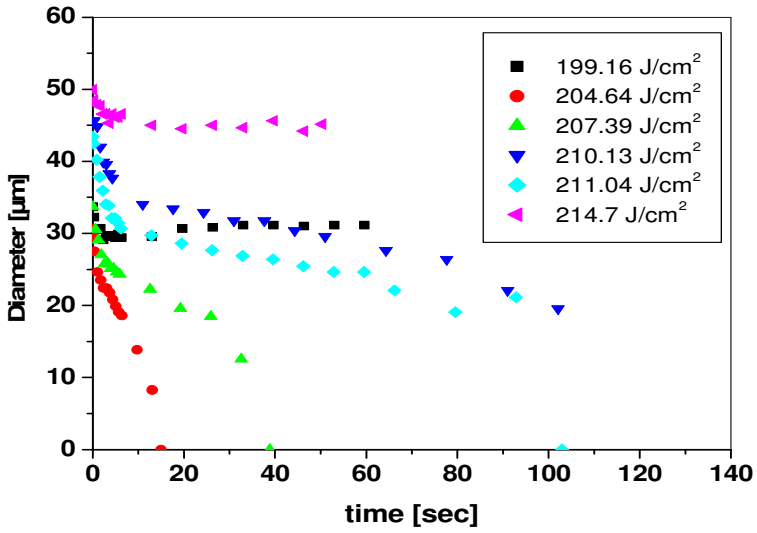

Fig. 3.5. Bubble diameter evolution when the bubbles are created by a single 5 ns Nd:YAG laser pulse at 532nm.

Figures 3.6 to 3.9 contain the evolution of the bubble diameter for bubbles formed by a different number of pulses (1 to 10) at three different repetition rates (1, 2 and 3 Hz). Two types of distinctive bubbles were obtained: Figures 3.6 and 3.8 show the typical trend for the **type 1** bubbles which are transient and, therefore, they shrink until they fully disappear. The data point with diameter equal to zero is missing in the plot, this is due to the lack of screen resolution to measure the bubble at the exact instant when the bubble collapses completely. Figures 3.7 and 3.9 show the **type 2** bubbles, which experience some shrinkage at the beginning, but they manage to remain at constant diameter in the agar gel for long periods of time. For the evolution of the **type 1** bubbles, it is possible to distinguish three different slopes that indicate the rate at which the bubble diameter collapses at different times, while in the case of the **type**

2 bubbles only two slopes are distinguished after the bubbles have formed. We must point out that in many cases, where several pulses were delivered, the average fluence value is not directly proportional to the initial bubble diameter as it is the case when a single pulse was delivered to the target (Fig. 3.5), this may be due to the fact that the shown value is the *average* fluence taken from all the applied pulses, but it is the pulses with higher fluence the ones that dominate the final size of the bubbles. There are cases where the delivery of 10 pulses at 2 and 3 Hz repetition rate resulted in rather too large bubbles, which could not be measured with the current experimental setup. Table 3.1 summarizes the type of bubble formed in all the experiments according to the number of pulses and the repetition rate and fluence used. It can be clearly seen that when the pulses are delivered at 1Hz it takes 10 consecutive pulses for the bubble to start to behave as a type 2 bubble, otherwise, the bubbles behave always type 1 bubbles; while in the case when pulses are delivered at 3 Hz all the bubbles, even those formed with just a couple of pulses, are permanent (type 2).

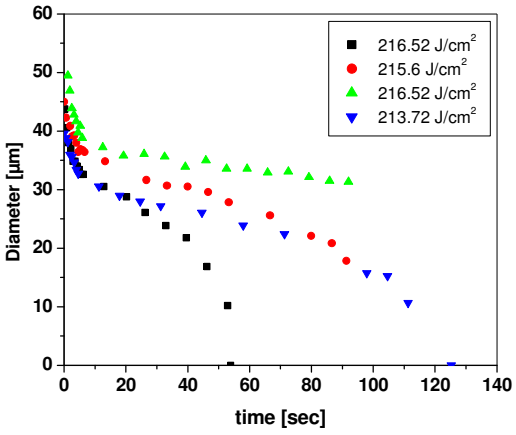

Fig. 3.6. Bubble dynamics when 6 pulses at 1 Hz are applied.

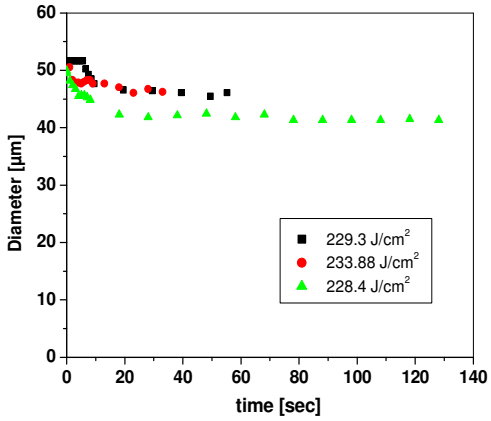

Fig. 3.7. Bubble dynamics when 10 pulses at 1 Hz are applied.

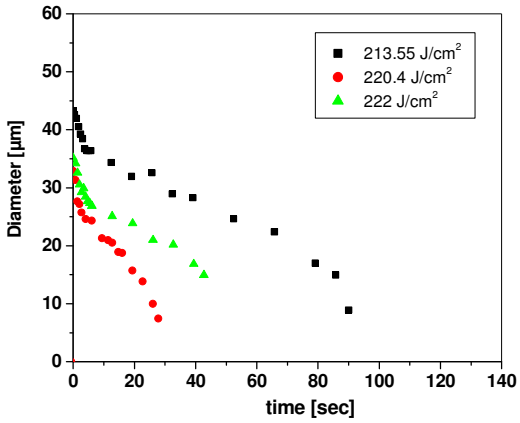

Fig. 3.8. Bubble dynamics when 2 pulses at 1 Hz are applied

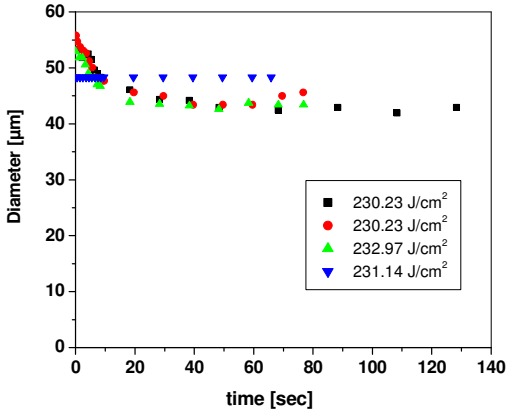

Fig. 3.9. Bubble dynamics when 2 pulses at 3 Hz are applied

Figures 3.10 and 3.11 describe the initial bubble diameter as a function of the number of pulses and the repetition rate at which the pulses were delivered on the target, respectively; error bars were added when calculation of standard deviation was possible from the experimentally acquired data. It can be seen from the plots and the experimental observation (Table 3.1) that there is a slight tendency of the bubble diameter to increase with the number of pulses at 1Hz and with repetition rate. This variation is more significant when 10 pulses are applied; unfortunately, this cannot be plotted in figures 10 and 11 because we were unable to measure those large bubbles, as mentioned above.

	Frequency		
Number of pulses	**1 Hz**	**2 Hz**	**3 Hz**
1	1	-	-
2	1	1	2
3	1	1	2
6	1	2	2
10	2	NM	NM

Table 3.1. Summary of bubble type obtained when different number of pulses at three different repetition rates. The type 1 bubble completely collapses with time; the type 2 bubble remains at a constant diameter in the agar gel. NM: means the bubble was too large to be measured with our current set up.

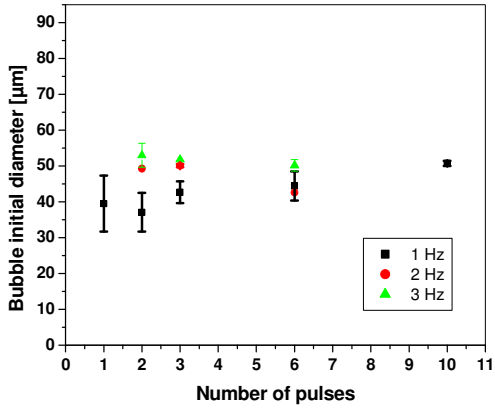

Fig. 3.10. Initial bubble diameter as a function of number of pulses

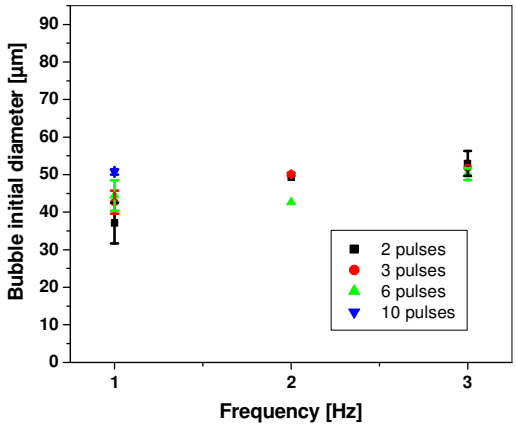

Fig. 3.11. Initial bubble diameter as a function of repetition rate.

Effect of Scattering.

Figures 3.12 and 3.13 show plots that compare the laser fluence required to form a bubble with a 5 ns laser pulse at three different depths in transparent and highly scattering agar gel, respectively. From Figure 3.12, it can be seen that there is insignificant difference in the fluence required to produce the bubble in transparent agar, regardless of the depth at which the beam is being focused; notice also that there is no a defined value for bubble formation threshold fluence, which is indicated by the overlapping of the fluence error bars for the bubble and no-bubble formation events. Figure 3.13 shows the data for bubble formation in highly scattering agar. It can be seen that in this case too, the laser fluence difference for the bubble and no-bubble formation is very small, although only for the cases where the laser beam is focused at depths of 50 and 100 µm. However, this laser fluence difference becomes larger if the laser beam is focused 200µm deep. It is also clear from comparison of Figs. 3.12 and 3.13 that the formation of all bubbles in the scattering agar requires larger fluences (on the order of 50% higher fluence) as compared to the formation of bubbles in transparent agar, especially for the 200µm deep case, where up to 3 times higher fluence is required.

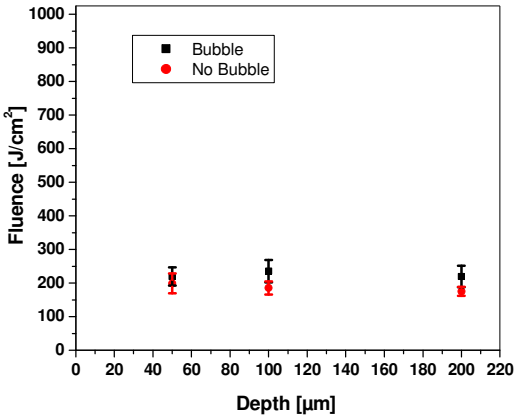

Fig. 3.12. Laser fluence required to form a bubble in transparent agar at different depths.

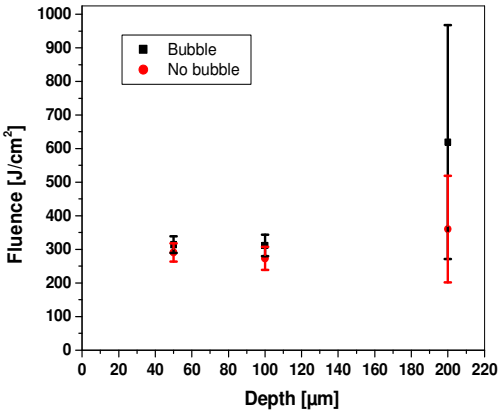

Fig. 3.13. Laser fluence required to form a bubble in scattering agar at different depths.

Irradiation with femtosecond laser pulses.

Similar experiments were carried out irradiating transparent agar gels with bursts from Ti:Sapphire femtosecond laser pulses positioning the focal point 100µm below the gel surface, the variation of the bubble size with time is shown in Figure 3.14; the maximum energy used for these experiments was the maximum energy that was available with the laser system at the moment of the experiment. The fluence value shown in Figure 3.14 for each curve is the average fluence of two burst that produced the bubble. It should be noticed that the initial size of the bubbles is half of the maximum size obtained with nanosecond laser pulses and that all of these bubbles collapse within 20 seconds, in contrast with those produced by nanosecond laser pulses. No permanent bubbles were observed.

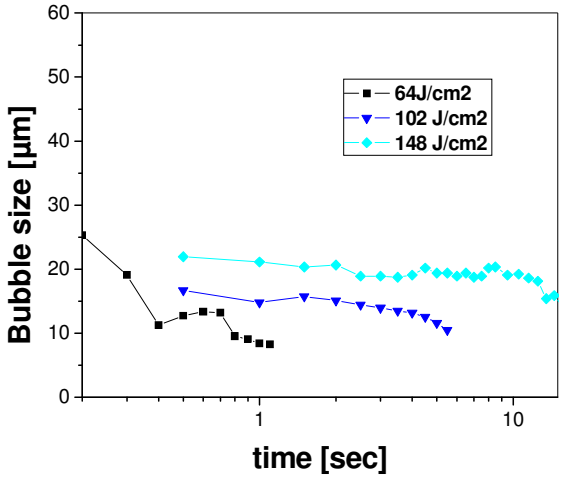

Fig. 3.14. Bubble dynamics when bursts of femtosecond laser pulses are applied to transparent agar gels positioning the beam's waist 100 below the gel surface.

Conclusion

The type of bubble (transient or permanent that can be produced by single 5 ns laser pulses is strongly dependent on the pulse fluence as shown in a previous work [24,25]; however, for fluences under the threshold for permanent bubble formation, the type of bubble that can be formed depends on the number of pulses and the frequency at which these are delivered. The fluence needed to form a bubble in highly scattering agar gel is ~50% more as that needed in clear agar gel at 50 and 100 µm deep. However, at 200 µm, at least 3 times higher fluence is required. Bubbles produced with femtosecond laser pulses with the fluences available in the laboratory were always transient and half the initial size than those produced with nanosecond laser pulses.

References

1. Verkruysse W, Beek JF, VanBavel E, Gemert MJCv, Spaan JAE. Laser Pulse Impact on Rat Mesentric Blood Vessels in Relation to Laser Treatment of Port Wine Stain. Lasers in Surgery and Medicine 2001; 28:461-468.

2. Tanzi EL, Lupton JR, Alster TS. Lasers in dermatology: Four decades of progress J Am Acad Dermatol 2003; 49:1-34.

3. Sadick NS. Laser Treatment With a 1064-nm Laser for Lower Extremity Class I-III Veins Employing Variable Spots and Pulse Widths Parameters. Dermatol Surg 2003; 29:916-919.

4. Ross EV, McKinlay JR, Sajben FP, Miller CH, Barnette DJ, Meehan KJ, Chhieng NP, M.J.Deavers, Zelickson BD. Use of a Novel Ebrium Laser in a Yucatan Minipig: A Study of Residual Thermal Damage, Ablation, and Wound Healing as a Function of Pulse Duration Lasers in Surgery and Medicine 2002; 30:93-100.

5. Pfefer TJ, Smithies DJ, Milner TE, Gemert MJC, Nelson JS, Welch AJ. Bioheat Transfer Analysis of Cryogen Spray Cooling During Laser Treatment of Port Wine Stains. Lasers in Surgery and Medicine 2000; 26:145-157.

6. Majaron B, Verkruysse W, Tanenbaum BS, Milner TE, Telenkov SA, Goodman DM, Nelson JS. Combining two excitation wavelengths for pulsed photothermal profiling of hypervascular lesions in human skin. Phys Med Biol 2000; 45:1913-1922.

7. Germert MJCv, Welch AJ, Pickering JW, Tan OT, Gijsbers GHM. Wavelengths for Laser Treatment pf Port Wine Stains and Telangiectasia. Lasers in Surgery and Medicine 1995; 16:147-155.

8. Gatinel D, Hoang-Xuan T, Azar DT. Volume Estimation of Excimer Laser Tissue Ablation for Correction of Spherical Myopia and Hyperopia Investigative Ophthalmology and Visual Science 2002; 13:1445-1449.

9. Dover JS, Arndt KA. New Approaches to the Treatment of Vascular Lesions. Lasers in Surgery and Medicine 2000; 26:158-163.

10. Aksan A, McGrath JJ. Thermomechnical Analysis of Soft-Tissue Thermotheraphy. Transactions of the ASME 2003; 125:700-708.

11. Ahcan R, Zorman P, Recek D, Ralca S, Majaron B. Port Wine Stain Treatment With a Dual-Wavelength Nd:Yag Laser and Cryogen Spray Cooling: A Pilot Study. Lasers in Surgery and Medicine 2004; 34:164-167.

12. Vogel A, Venugopalan V. Mechanisms of Pulsed Laser Ablation of Biological Tissues. Chem Rev 2003; 103:577-644.

13. Vogel A, Noack J, Huttman G, Paltauf G. Mechanisms of femtosecond laser nanosurgery of cells and tissues. Applied Physics B 2005; 81:1015-1047.

14. Du D, Liu X, Korn G, Squier J, Mourou G. Laser-Induced Breakdown by Impat ionization in SiO_2 With Pulse Widths from 7 ns to 150 fs. Applied Physics Letters 1994; 64:3071-3073.

15. Anderson R, Parish JS. Selective Photothermolysis, precise microsurgery by selective absorption of pulsed radiation Science 1983; 220:524-527.

16. Svaasand LO, Randeberg LL, Aguilar G, Majaron B, Kimel S, Lavernia EJ, Nelson JS. Cooling efficiency of cryogen spray during laser theraphy of skin. Lasers in Surgery and Medicine 2003; 32:137-142.

17. Majaron B, Svaasand LO, Aguilar G, Nelson JS. Intermittent cryogen spray cooling for optimal heat extraction during dermatologic laser treatment. Physics in Medicine and Biology 2002; 47:3275-3288.

18. Karapetian E, Aguilar G, Kimel S, Lavernia EJ, Nelson JS. Effects of mass flow rate and droplet velocity on surface heat flux during cryogen spray cooling Physics in Medicine and Biology 2003; 48:N1-N6.

19. Edris E, Choi B, Aguilar G, Nelson JS. Measurements of laser light attenuation follwong cryogen spray cooling surt termination. Lasers in Surgery and Medicine 2003; 32:143-147.

20. Aguilar G, Wang GX, Nelson JS. Dynamic behavior of cryogen spray cooling: effects of spurt duration and spray distance. Lasers in Surgery and Medicine 2003; 32:152-159.

21. Aguilar G, Diaz SH, Lavernia EJ, Nelson JS. Cryogen sparay cooling Efficiency: Improvement of port wine stain laser therapy through multiple-intermittent cyogen spurts and laser pulses. Lasers in Surgery and Medicine 2002; 31:27-35.

22. Vogel A, Venugopalan V. Mechanisms of pulsed laser ablation of biological tissues. Chem Rev 2003; 103(2):577-644.

23. Romo-Cadenas G, Perez-Gutierrez FG, Mina-Rosales A, Camacho-Lopez S, Aguilar G. Study of ns and fs pulse laser-induced effects in biological tissue models and corneal tissue. IX Medical Physics Conference, Guadalajara, Jalisco 2006.

24. Romo-Cardenas G, Camacho-Lopez S, Perez-Gutierrez FG, Aguilar G. Estudio de efectos foto-inducidos en modelos de tejido-biologico usando pulsos laser de nanosegundos. XLVIII Congreso Nacional SMF/XVIII Reunion Anual de Optica 2005; OPTICA2005 OM-01-1.

25. Romo-Cardenas G, Perez-Gutierrez FG, Mina-Rosales A, Camacho-Lopez S, Aguilar G. Study of ns and fs pulse laser-induced effects in biological tissue models and corneal tissue. IX Medical Physics Conference, Guadalajara, Jalisco 2006.

Chapter 4: Mechanical response of artificial tissue models irradiated with Nd:YAG nanosecond laser pulses.

Introduction

Laser-ablation of tissue with nanosecond laser pulses has been widely studied in the past and has been introduced in medical applications. The mechanisms of interaction between nanosecond laser pulses and biological tissues are very interesting in medicine because it is possible to induce tissue ablation, but also cutting and tearing with high precision and minimal thermal and mechanical damage to the surrounding tissue. An excellent review of pulsed laser ablation is given in [1]. At low irradiance, the optical energy couples to the target material according to the material's linear absorption coefficient [2,3]. In this regime, thermal effects are dominant and if the laser pulse is shorter than the acoustic relaxation time, stress confinement conditions occur and a thermoelastic expansion of the material launches a pressure wave [4-6]. In contrast, at high irradiance, it is possible to couple optical energy to optically transparent materials [7]. As the irradiance increases, the laser pulse ionizes the material via multiphoton ionization seeding free electrons that serve as absorbers of photons. When photons are absorbed further, more electrons are released serving as absorbers of more photons via an avalanche ionization [1,2]. This energy coupling mechanism is what is referred to as non-linear absorption.

From an experimental point of view, for nanosecond and picoseconds laser pulses, the threshold for plasma formation is definded as the radiant exposure (or fluence) at which there is observation of luminescent plasma. For shorter laser pulses, plasma does not emit luminescence in the visible part of the spectrum and the threshold has to be experimentally determined through the observation of cavitation bubbles in water. From a theorethically point of view plasma formation is identified by the generation of a free electro density between 10^{18} and 10^{21} cm^{-3} [1]. Evidence of plasma formation within tissue-like models (like water or gels) is the appearance of bubbles, even with nanosecond laser pulses.

Laser induced bubbles are very important and deserve special attention as they are the principle in which tissue ablation, cutting and tearing is based. Laser-induced bubbles, however, are not exclusive

evidence of plasma formation but they may be formed by different mechanisms. When plasma is formed in transparent water or a gel, the violent expansion of plasma pushes the surrounding material launching a shock wave and an oscillating cavitation bubble results from vaporization of the material where plasma was formed. Under this scenario, thermal effects to the surrounding tissue are negligible [1,8-11]. If the plasma is very strong and pressure within the bubble is enough to plastically deform the gel, the result is long lasting bubbles like those reported in chapter 3.

A second type of laser-induced bubbles is cavitation bubbles, which may be induced at moderate temperature increments (below 100 ^{o}C) aided by tensile stresses. These bubbles are induced in water or gels with high linear absorption coefficient. With a nanosecond laser pulse, the fast energy deposition creates the conditions to launch a compressive pressure wave. When this compressive wave interacts with a water/air interface, it is reflected as a tensile wave [5,12]. This tensile wave represents a low local pressure that reduces the temperature required to achieve the saturation point and therefore produce a phase change.

Additionally, a third type of laser-induced bubbles are boiling bubbles, which happen when fast light absorption, like with nanosecond laser pulses, is high enough to produce temperature increments higher than the saturation temperature or even the spinodal limit. This type of bubbles is treated in the next chapter.

The separation between cavitation and boiling bubbles is not well defined when the tissue model is both heated and subjected to tensile stresses (stretched) at the same time. From this perspective, mechanical effects induced by nanosecond laser pulses are very interesting as both absorption regimes: linear (which induces heating) and non-linear (which induces the tensile stresses) can be found.

The objective of this chapter is to carry out a comprehensive experimental analysis of the mechanical effects that result when tissue models are irradiated with nanosecond laser pulses to elucidate the relative contiribution of linear and nonlinear absorption to bubble formation.

Three different experimental techniques were used for this purpose: (1) home made polyvinylidene fluoride (PVDF) transducers [13,14], (2) time-resolved imaging (TRI) [15] and (3) time-resolved Mach-Zehnder interferometry (TRIF) [16-18]. PVDF is a piezoelectric polymer that allows recording the time history of pressure transients. The shape of this signal carries important information

about the laser-tissue interaction. Such sensors are suitable for these experiments because of its low cost, fast time response and high sensitivity. However, the disadvantage for the current experimental conditions in the laboratory is that pressure can only be measured at approximately 1 mm away from the beam focus position without risk of damaging the transducer. In order to measure the pressure next to the focal point, a time-resolved imaging (TRI) system was developed. Images from the TRI system are useful to visualize the propagation of a shock wave when plasma is formed. TRI provides information of the rate of change of the shock wave radius as a function of time, i.e. the shock wave velocity. A mathematical model combines the shock wave velocity, the material properties and speed of sound, to calculate pressure difference between the shocked and unshocked regions. The disadvantage of TRI is that it is not useful to measure pressure transients when plasma is not formed. To overcome this limitation, a time resolved Mach-Zehnder interferometer (TRIF) was built to study the mechanical effects that occur when the irradiance of nanosecond laser pulses is not high enough for plasma formation and the energy is linearly absorbed within the tissue model. The combination the PVDF sensors and TRI systems allowed characterization of the pressure distribution within the tissue model, while TRIF allowed measurement of pressure due entirely to the linear absorption of laser light at the irradiation volume.

For tissue models, we used both agar gels with two agar concentrations and water. The selection of each model depended on each experiment. Both gels and water were used with PVDF sensors and TRI, whereas only water was used for the TRIF experiments.

Materials and methods

Tissue models

For the experiments presented here, agar gel blocks with thickness from 1 to 11 mm were made. Two agar concentrations were prepared with 2 and 4 grams of agar powder in 100 ml of deionized water. To prepare the gels, deionized water was heated to boiling point and agar powder in solution was added to meet the required concentrations; then the liquid agar gel was poured into molds of the appropriate thickness made with glass slides.

Direct Red dye is a red color organic dye with high linear absorption in the green part of the spectrum similar to hemoglobine (Hb), which is a reference value for medical applications since most tissues contain blood.. Fig.4.1 shows the absorption spectrum of a 10% aqueous solution of Direct Red. The linear absorption coefficient of the agar gels and aqueous solutions was varied adding Direct Red dye so the resulting linear absorption coefficients at λ=532 nm were μ_a = 22, 33, 47 and 97 cm^{-1}. These linear absorption coefficients were determined according to the methodology described in [19].

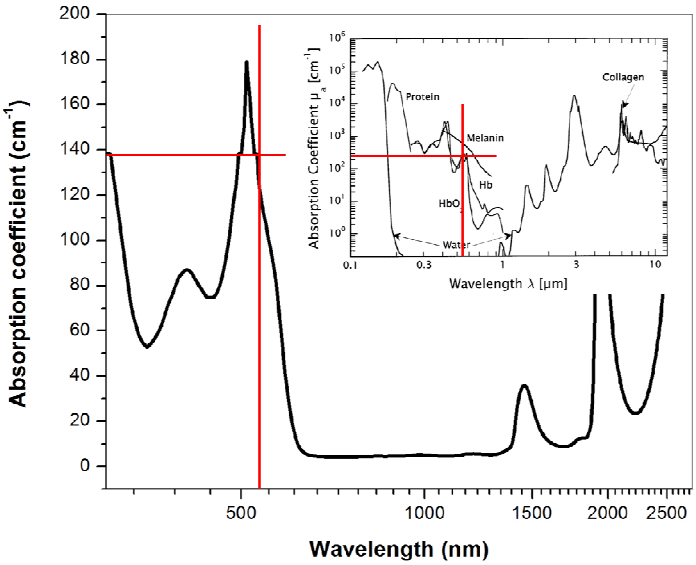

Fig 4.1 Absorption coefficient spectrum of an agar gel with 10% Direct Red concentration. Direct red absorption peak is in the green part of the spectrum. This peak makes Direct Red an ideal dye to model hemoglobin absorption of green light. (Insert) Absorption coefficient spectrum of hemoglobin and other skin chromophores for comparison purposes [1].

Piezoelectric sensors

Polyvinylidene fluoride (PVDF) is a polymer with pyroelectric and piezoelectric properties that make it suitable to measure laser-induced stresses. A pressure sensor was made using a 25 μm thick, aluminum-metalized PVDF film. The sensor was connected to a digital oscilloscope through a 1MΩ impedance to ensure proportionality of voltage to pressure [20]. The PVDF transducer sensitivity was 85 mV/MPa and the response time was measured to be 30 ns. Single oscilloscope traces were obtained for each laser exposure, i.e. the signals obtained were not averaged using the oscilloscope controls.

Laser exposures and laser parameters

Figure 4.2 shows the configurations under which laser exposures were carried out. Fig. 4.2A shows the experimental set up for the measurements with the PVDF sensor. Fig. 4.2B shows the configuration when the beam waist was positioned on the surface of the agar gel block; this configuration was useful to limit the interaction region to the high irradiance (beam waist) only. Fig. 4.2C shows the configuration when the beam waist was positioned 1 mm below the agar gel block surface. This configuration was useful to study the interaction under linear absorption conditions.

The agar gel block was displaced after each laser exposure to avoid any interference with irregularities in the material due to remaining bubbles/craters from previous exposures. For experiments with water, a cuvette was glued to the sensor's aluminum case. The beam waist was found using the equivalent target plane (ETP) system described in the section below.

Laser energies used in the present study were kept below 1 mJ as higher energies tend to produce long lasting bubbles in agar gel when the laser pulse is focused [21]. The laser was focused to a beam waist $1/e^2$ radius of 2.3 μm, measured with the ETP system (described below).

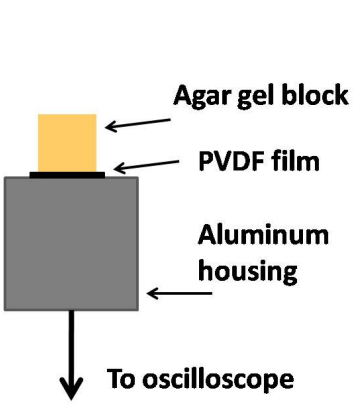

Fig.4.2A. Experimental set-up for measurement of pressure transients with PVDF sensors.

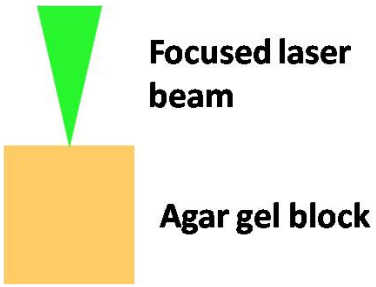

Fig. 4.2B. Laser exposure configuration when the beam waist was positioned on the surface of the agar gel.

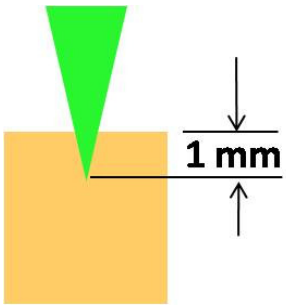

Fig. 4.2C. Laser exposure configuration when the beam waist was positioned 1 mm below the surface of the agar gel.

Time Resolved Imaging (TRI)

The experimental setup for time-resolved imaging of laser-agar gel interactions is shown in Fig. 4.3. It consists of two nanosecond laser systems electronically synchronized. The first, used as the pump, was a Brilliant (Quantel, Les Ulis Cedex, France), Q-switched, Nd:YAG laser that incorporates the second harmonic crystal to produce 6 ns laser pulses at λ=532 nm. The second, used as the probe, was an EKSPLA (Lithuania), Q-switched, Nd:YAG that incorporates an Optical Parametric Oscillator (OPO). The OPO was set to operate at λ=1064 nm. This probe wavelength was chosen because Direct Red dye has low linear absorption at this wavelength compared to that at 532 nm [15].

Both beams were brought co-linear onto the sample. The delivered energy was varied with the combination of the half wave plate (HWP1) and polarizer (P1). Energy was monitored with a cross-calibrated energy meter (EM) (Ophir) to a second energy meter, (Molectron, Portland OR) positioned at the sample's location. The probe beam energy was varied changing the relative delay of the Q-switch to flash lamp by means of the triggering electronic pulse from the delay generator (DG) (BNC, San Rafael CA, USA). The beam passed collimated through the sample by means of lenses L1 (f=35mm) and L2 (f=6mm).

A magnified image of the sample is formed by the combination of lenses L3 (f=25 mm) and L4 (f=400 mm) onto a CCD camera (IMI Tech, Seoul, Korea). A long-pass filter with cut-off wavelength at λ=610 nm (RF) positioned in front of the CCD blocked scattered light from the green pump beam.

The electronic delay generator DG provided the electronic pulses required to externally trigger both laser systems at 10 Hz repetition rate. The relative delay between the probe pulse and the pump pulse can be set directly with the DG unit's controls. Single laser pulses from the pump beam are selectively released by a mechanical shutter (MS) (Uniblitz, Rochester NY, USA) that opens its aperture for 100 ms, therefore allowing only one laser pulse to pass through it. This is achieved by applying 3 V, 100 ms long square pulses from a signal generator SG (BNC, San Rafael CA, USA) to the mechanical shutter driver MSD (Uniblitz, Rochester NY, USA). The settings in the SG are 3 V, 5 Hz, 50% duty cycle. Simultaneously, the signal out of the SG is divided and also sent to trigger the CCD whose exposure time was set to 130 ms. This exposure time guarantees that only light from the probe pulse is captured by the CCD up to tens of milliseconds after the pump pulse released from the MS. At the same time the SG is externally triggered with a DC power supply DCPS (Circuit Specialists, Inc., Mesa AZ, USA) and a custom made hand trigger HT. The delay generator could produce delays as short as 1 ns, however the experimental setup time resolution is given by the probe pulse duration, which was 6 ns.

The lens L1 in the IR beam also served a second purpose. The CCD could be placed to have the pump beam retro-reflected from the target onto the CCD in an image relay; this setup is commonly referred to as as an equivalent target plane (ETP) system. The ETP was used to set the location of the beam focus in the sample when each new sample was placed. The pump laser was focused to a beam waist $1/e^2$ radius of 2.3 μm, measured with the ETP system. The probe laser passed the sample with a $1/e^2$ radius of 175 μm and a per pulse energy of 1 μJ.

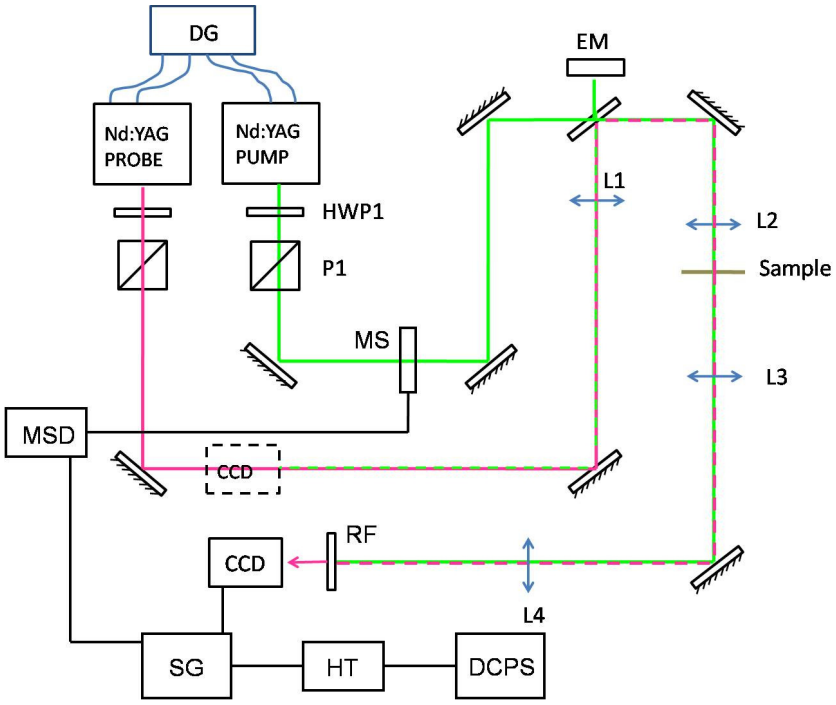

Fig. 4.3. Experimental set up for time-resolved imaging (TRI) and equivalent target plane (ETP) system (see body of the text).

Time-resolved Mach Zehnder interferometry (TRIF)

The mechanical effects of linearly absorbed laser energy were monitored with a Mach-Zehnder interferometer. The experimental set up is shown in Fig. 4.4. The probe and pump beam were electronically synchronized in the same way they were for the TRI system and the synchronization details are not shown again in Fig. 4.4. The pump pulses were delivered by the Quantel laser at λ=532 nm, while the probe pulses were delivered by the OPO system of the EKSPLA laser at λ=633 nm. The pump pulse is focused in the bulk of the Direct Red solution by a removable aspheric lens L1. The probe pulse is split into two paths by means of a 50/50 beam splitter BS1. A quartz cuvette filled with an aqueous solution of Direct Red is placed conviently so that the pump pulse is incident on on it from above and its energy absorbed by the Direct Red solution. Another quartz cuvette filled with the same Direct Red solution is positioned in the reference arm of the interferometer so that both optical paths are equal. The two arms are recombined at a second 50/50 beam splitter BS2 where an interference fringe pattern is generated. A 50 mm focal length

lens magnifies the interferogram and sends the image to the CCD camera. As in the TRI system, the temporal resolution of the TRIF system is given by the probe pulse duration.

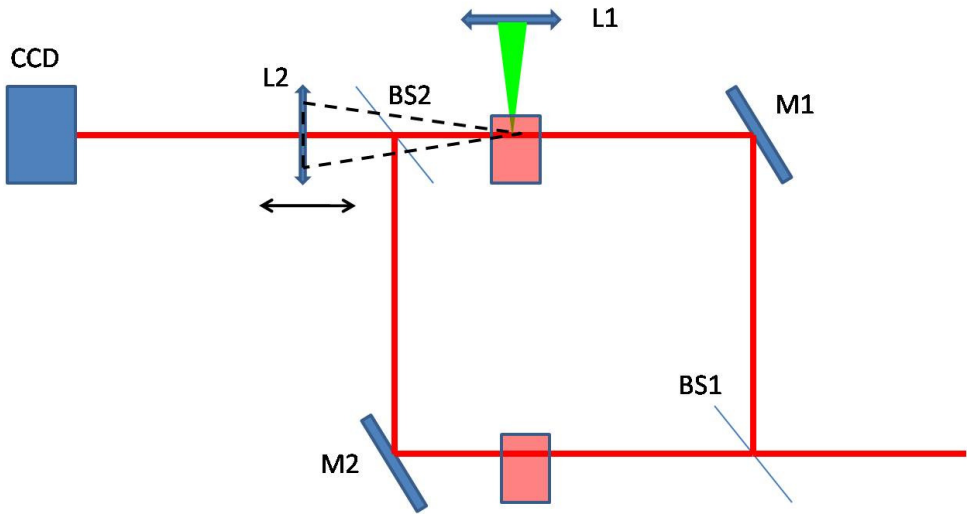

Fig 4.4 Experimental set up for TRIF. Pump and probe pulses are electronically synchronized as in Fig. 4.3

Results and discussion

Variation of mechanical properties

Figure 4.5 shows the typical wavefrom obtained when a nanosecond laser pulse is focused 1 mm below the surface of transparent agar gel blocks and deionized water. From now on, the laser beam waist (focus) is in this same position unless otherwise indicated. The laser energy was 500±50 μJ and the distance from the beam waist to the PVDF sensor was 10 mm. Waveforms are shown at this distance from the beam waist to ensure that the pressure wave curvature, which starts as a spherical shock wave [8], is large enough so it can be considered as a plane wave when it reaches the PVDF film. In general the waveforms have a bipolar shape. At time t=0, there is a sharp rise of the signal that gets to a maximum within a few hundreds of nanoseconds and gradually decreases. It has been shown previously by optical means that the actual shock wave width produced by a 200 mJ nanosecond laser pulse in water is about 25 ns [8], so the actual shock waves in these experiments are most likely shorter. As the signal decreases, there is a sharp decrease followed by a local minimum and eventually the magnitude reaches a zero value again. The sharp rise is

produced by the lower part of the spherical shock wave that propagates downwards to the sensor. The sharp decrease is produced because the upper part of the shock wave that propagates upwards is reflected backwards with inverted sign after it interacts with the agar gel or water-air interface where it finds an acoustic impedance mismatch.

Figure 4.6 shows the maximum amplitude of the waveforms as a function of the laser pulse energy for the three materials studied. As expected, the higher the energy, the higher the amplitude. However for laser energies below 500 μJ, the amplitude for the 2% agar and deionized water overlap, while the amplitude for the 4% agar remains lower. This observation is more evident in Fig 4.5 (read below) when the amplitude of the pressure wave is measured at different distances from the beam waist. This is because 4% agar is significantly stiffer than 2% agar and deionized water; therefore the expanding plasma launches a weaker shockwave.

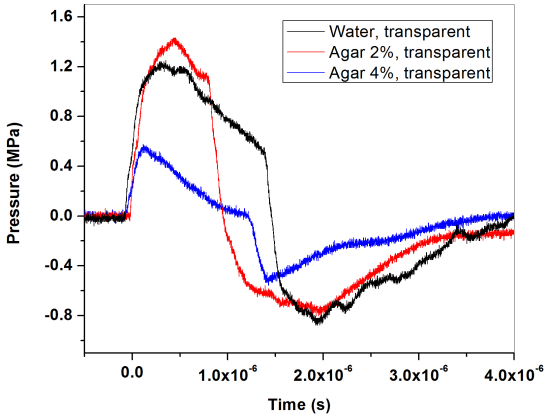

Fig. 4.5. Pressure signal detected with PVDF sensor when the beam waist was positioned 1 mm below the surface of the agar gel and 10 mm away from the PVDF sensor.

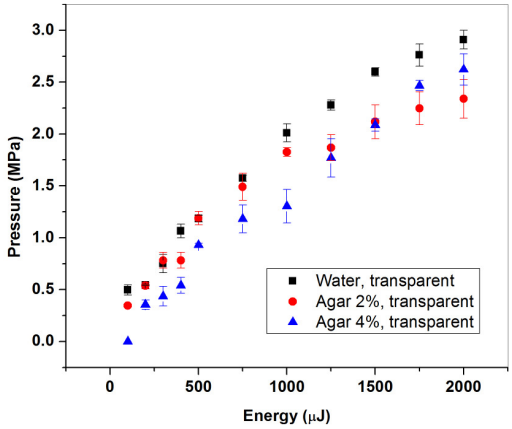

Fig. 4.6. Pressure amplitude measured 10 mm away form the beam waist as a function of energy. Beam waist was positioned 1 mm below the surface of the agar gel.

Pressure as a function of distance

Figure 4.7 shows the maximum amplitude of the pressure wave measured with agar samples of different thicknesses. Using samples of different thicknesses allows to measure pressure at specific

distances from the beam waist. The energy per pulse was 500±50 μJ. The pressure amplitude for the 2% agar blocks and deionized water overlap and show a linear decay with sample thickness; the pressure amplitude drops by 25% while it propagates from 1 mm to 10 mm away from its origin to the PVDF sensor. In contrast, the maximum pressure amplitude for the 4% agar gel blocks is approximately 40% lower than that for 2% agar blocks and water. Although the amplitude for this agar concentration is higher measured 1 mm away from the beam waist, the rest of the measurements for longer distances away from the beam waist do not show decay as steep as it is for the 2% agar gel blocks and deionized water.

It is very difficult to perform measurements with the PVDF sensor for samples thinner than 1 mm because there is a large chance of damaging the sensor. Therefore, the shock wave amplitude is investigated indirectly using a mathematical model that involves the information that can be obtained from TRI. Such information is the shock wave radius as a function of the relative delay from the pump and probe pulses. The shock wave velocity can be obtained calculating the derivative of this function and pluged into equation 4.1. Mathematical derivation of this equation starting from mass, momentum conservation equations and Hugonit equation to relate the shock wave velocity to the particle velocity is in [15] and references therein:

$$P_1 - P_2 = \rho_2 U\left(\frac{U - C_s}{S}\right) \tag{4.1}$$

where P_1-P_2 is the pressure difference between the shocked and unshocked regions, ρ_2 is the agar gel density, U is the shock wave velocity, C_s is the speed of sound and S is the Hugoniot coefficient for 10% gel. C_s and S values are 1520 m/s and 2.0 respectively [15].

Figure 4.8 shows the pressure distribution inside the agar gel blocks and deionized water from 50 μm to 10 mm away from the beam waist. It contains the same data points than Figure 4A from 1 to 10 mm, in addition to the data points 50 μm away from the beam waist calculated with equation 4.1. Shock wave velocites for these data points were obtained from TRI. Only one data point for each

material was calculated. The reason is because the field of view of the CCD camera was such that the shock wave radius increased linearly with respect to the pump-probe delay, and therefore shock wave speed was observed to be constant; in other words, it was impossible to see the shock wave deceleration until it becomes a pressure wave. It is expected that the shock wave becomes a pressure wave propagating a sonic speed in less than 150 ns after optical breakdown [8].

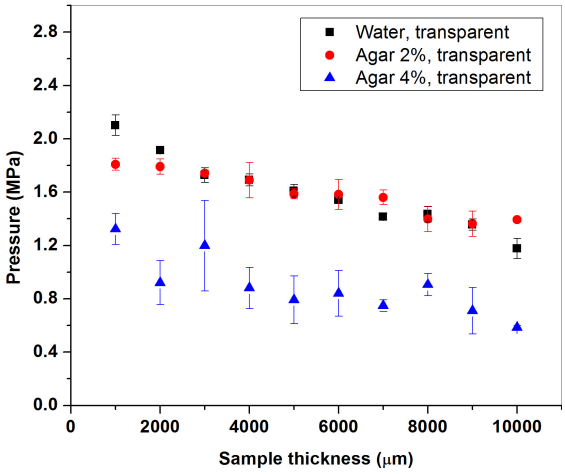

Fig. 4.7. Pressure distribution within agar gel from 1 mm to 10 mm measured with PVDF sensor. Energy per pulse was 500 μJ.

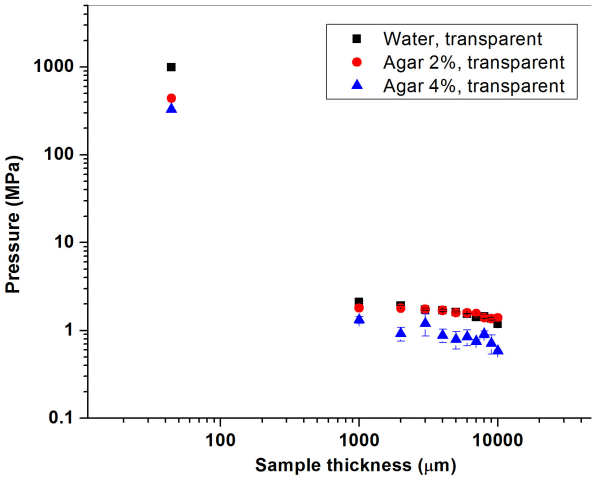

Fig. 4.8. Pressure distribution within agar gel from 50 μm to 10 mm measured with PVDF sensor and TRI. Energy per pulse was 500 μJ.

Pressure for different irradiation configurations

Fig. 4.9A shows the pressure wave originated when an unfocused nanosecond laser pulse is incident on an absorbing agar gel block. The wave gradually increases exponentially with a slope according to the Beer's law and the gel's absorption coefficient. If stress confinement conditions are met and ablation threshold is not overcome, the entire signal has a symmetric bipolar shape such that the integral vanishes [6]. Fig. 4.9B shows the typical signal when the beam waist is positioned on the gel surface and Fig. 4.9C corresponds to the configuration positioning the beam waist 1 mm below the gel surface. All these signals show a sharp increase at t = 0, reach a maximum and then decrease.

In contrast to Fig 4.9A, the sharp rise in Figs. 4.9B and 4.9C is produced by a shock wave that is launched due to plasma formation. The pressure signal in Figure 4.9B shows two spikes on top of

the signal originated. In this experiment the beam waist was positioned on the surface of the agar gel using the ETP system previously described, however, there is an inherent error in the beam waist positioning in the order of the lens' Rayleigh range. When the beam waist is positioned 40 μm above the gel surface, twice the Rayleigh range of the lens used, and the irradiance is enough to ionize the air above, two different pressure waves are generated and travel simultaneously. The first, labeled with number 1 in Fig. 4.9B, is generated by the plasma formation in air and propagates downwards to the sensor. The second spike, labeled with number 2, is originated by linear absorption of the light that propagates after the plasma and is incident on the agar gel surface. The final signal shown in figure 4.9B is the superposition of these two waves. Interestingly, oscilloscope traces with spikes very similar to those obtained here are shown in recent studies where a PDVF sensor was developed to monitor nanosecond laser induced-bubble collapse near a solid surface [16,17]. Clearly the laser exposure configuration used in the present study is different and bubble collapse is not the mechanism responsible for the spikes we observe in our experiments.

Figure 4.9C shows a pressure wave originated in an agar gel block when the beam waist was positioned 1 mm below the surface. Here the lower part of the spherical shock wave propagates as a compressive wave towards the sensor, while the upper part propagates also as a compressive wave towards the free surface and is reflected backwards with inverted sign as a tensile wave. The change from compressive to tensile wave takes place due to the acoustic impedance mismatch between the agar gel surface and air. The tensile wave is clearly shown as a sharp decay in the pressure wave in Figure 4.9C. The time difference between the rise edge of the pulse (compressive) and the fall edge (tensile) agrees well with the time that it takes for an acoustic wave to travel 2 mm at 1500 m/s. For this rough calculation, the deceleration of the wave from shock wave to a pressure wave is neglected.

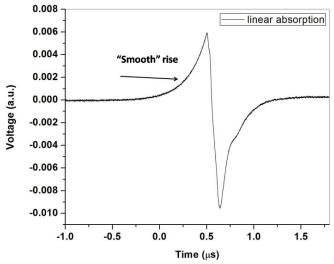

Fig. 4.9A. Pressure signal obtained with a PVDF sensor when an unfocused, 6 ns laser pulse is incident on an absorbing, 10 mm thick agar gel. μ_a=33 cm^{-1}.

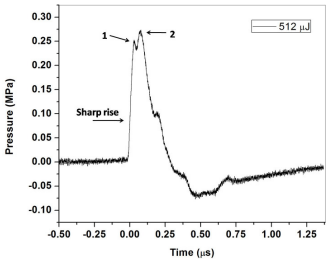

Fig. 4.9B. Pressure signal obtained with PVDF sensor when a focused, 6 ns laser pulse is incident on an absorbing 10 mm thick agar gel. Beam waist was positioned on the surface of the agar gel. μ_a=33 cm^{-1}.

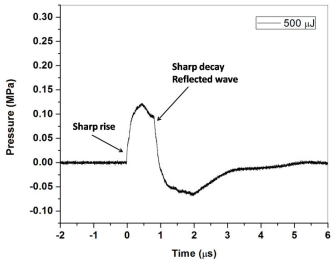

Fig. 4.9C. Pressure signal obtained with PVDF sensor. Focused, 6 ns laser pulse is incident on absorbing, 10 mm thick agar gel. The beam waist was positioned 1 mm below the agar gel surface. μ_a=33 cm^{-1}.

Linear absorption coefficient

Fig. 4.10 shows the amplitude of the pressure signals detected with the PVDF sensor when the laser waist was positioned 1 mm below the 2% agar gel surface surface and 10 mm away from the sensor for different absorption coefficients as a function of the per pulse energy. The transparent agar gel shows higher pressure increments because almost the entire energy from the laser pulse is deposited in the focal volume and is readily available to produce plasma. In contrast, pressure amplitude for absorbing agar gels show lower pressure increments because the beam propagates 1 mm through the gel and the energy that remains to produce plasma is less than in the previous case. In fact, for the 47 cm^{-1} agar gel blocks, no signal was detected for energies lower than 500 μJ. The heat generated while the beam propagates through the 1 mm is not enough to induce a pressure wave detectable with the sensor because the size of the beam is large and therefore the fluence low. No changes of the pressue signal as a function of the pulse energy were detected for the configuration when the beam waist was positioned on the surface of the agar gel.

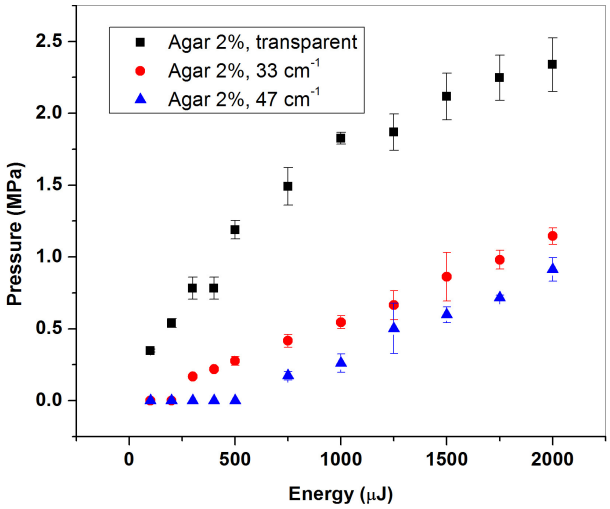

Fig. 4.10. Pressure amplitude as a function of per pulse energy. Laser pulses were incident 1 mm below the surface of agar gel blocks.

Time-resolved Mach-Zehnder interferometry (TRIF)

Figures 4.11 and 4.12 show the sensitivity obtained with the Mach-Zehnder interferometer built. Fringe shift indicates a phase difference between the probe and reference arms of the interferometer. Fig. 4.11 shows the interferogram originated due to an elliptical shockwave launched by optical breakdown in air. Fig. 4.12 shows a plane wave propagating in the direction of the arrows in a Direct Red aqueous solution with μ_a= 22 cm^{-1}. Lens L1 was removed and the laser beam was incident from the top of the picture. Spot size was 5 mm.

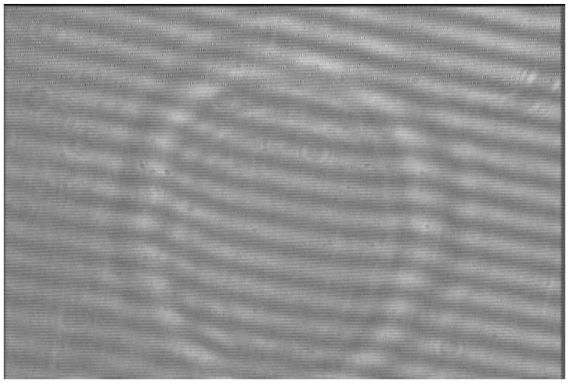

Fig. 4.11. Shock wave induced focusing a 6 ns laser pulse in air.

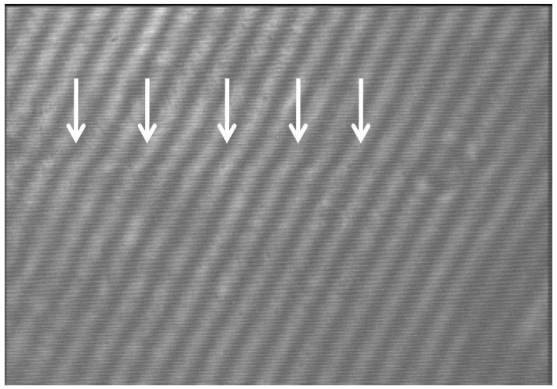

Fig. 4.12. Plane wave propagating downwards originated by an unfocused nanosecond laser pulse incident on a Direct Red solution with μ_a= 22cm^{-1}.

Figures 4.13 and 4.14 show images of a cavitation bubble that was formed when the pump laser beam was focused in the bulk of the Direct Red solution and the laser irradiance at the focal point was not high enough to produce plasma. Fig. 4.13 shows a simple image of the bubble when the reference arm of the interferometer had been blocked and Fig 4.14 shows the interferogram when another bubble was formed under similar irradiation conditions. No fringe shift was observed in Fig. 4.14. Although the irradiated volume increased its temperature upon laser energy absorption, the lack of fringe shift in the interferogram may be explained because the beam waist was about 6 μm in diameter, which is too slender to induce a phase change in the optical propagation path of the probe arm with respect to the reference arm of the Mach-Zehnder interferometer.

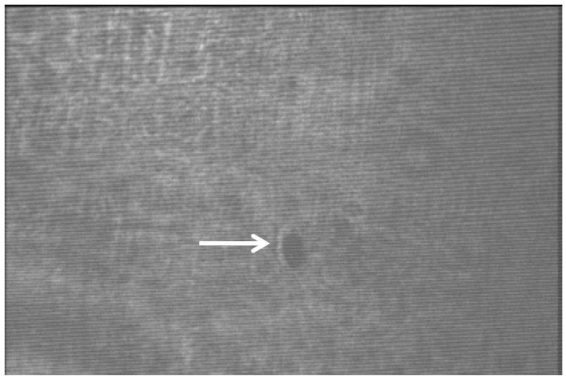

Fig. 4.13. Simple image of a cavitation bubble formed when a nanosecond laser pulse focused in the bulk of a Direct Red solution didn't have enough intensity to produce plasma.

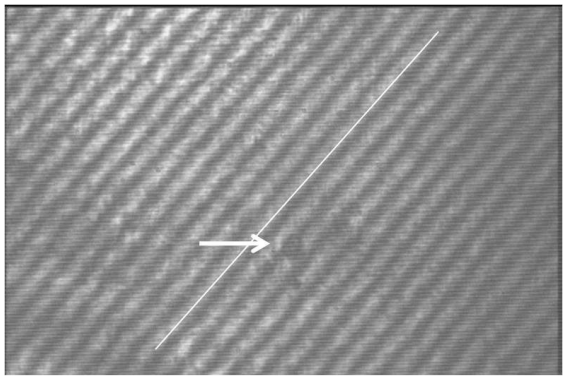

Fig. 4.14. TRIF image of a cavitation bubble when a nanosecond laser pulse a nanosecond laser pulse focused in the bulk of a Direct Red solution didn't have enough intensity to produce plasma. No phase shift was observed.

Given that no phase change was registered when the laser beam was focused in the Direct Red solution with laser fluence under the threshold for plasma formation, the approach was to increase the size of the laser beam and laser pulse energy to create cavitation bubbles under similar conditions. Fig. 4.15 shows a schematic of the new experimental conditions. For these experiments, the lens L1 in Fig. 4.4 was removed. The pump beam was collimated and reduced to a 1 mm diameter. The absorption coefficient of

the sample was μ_a=22 cm^{-1} which produced penetration depth δ = 450 μm. Under such conditions δ is comparable to the beam diameter and a cylindrical wave propagating in the radial direction results.

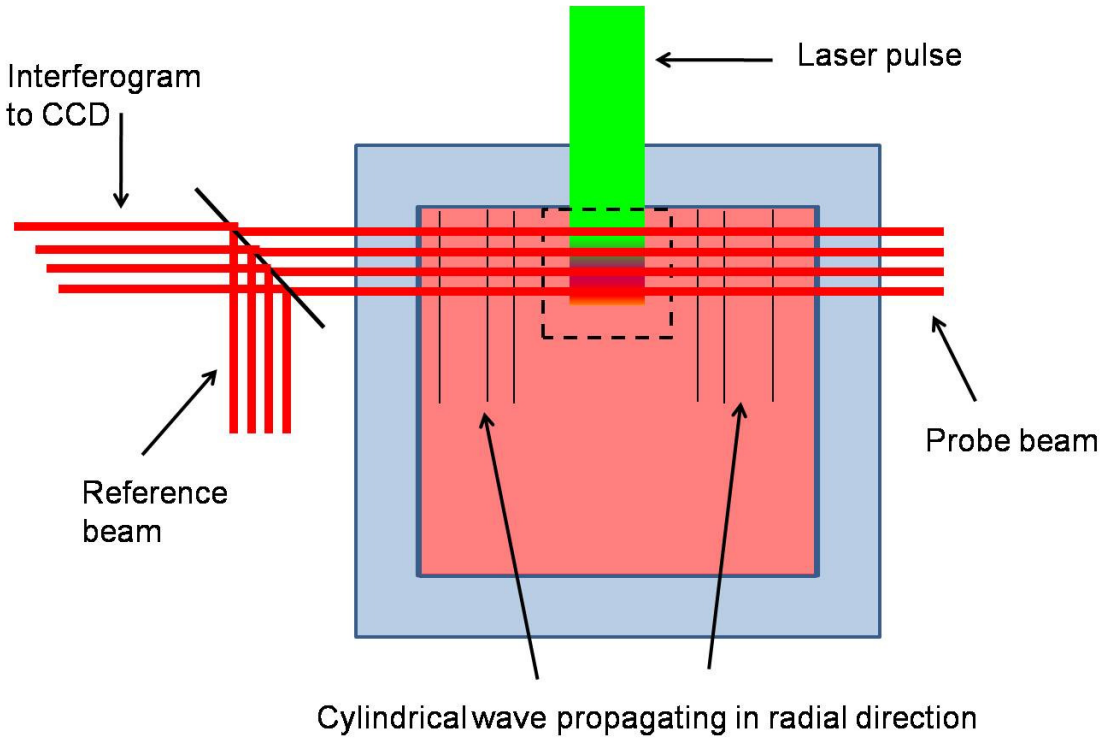

Fig. 4.15. Experimetal conditions in which a nanosecond laser pulse is linearly absorbed in an aqueous solution of Direct Red and the interaction region is observed through TRIF. Because δ is comparable to the beam diameter, a cylindrical wave propagating in the radial direction results.

Figure 4.16 shows images of TRIF carried out in the irradiated volume. Although it is still difficult to observe the cylindrical wave propagating in the images in Fig. 4.16, it is visible during the first 250 ns when a movie with these same images is made. It is possible to observe a fringe shift along the beam propagation path.

The fringe shift was measured for each picture obtained. No significant difference in the optical phase change was observed as a function of time. This is because the heat generated upon laser pulse energy absorption is confined to the irradiation volume for at least the 5 μs delay with respect to the pump pulse when the images were taken.

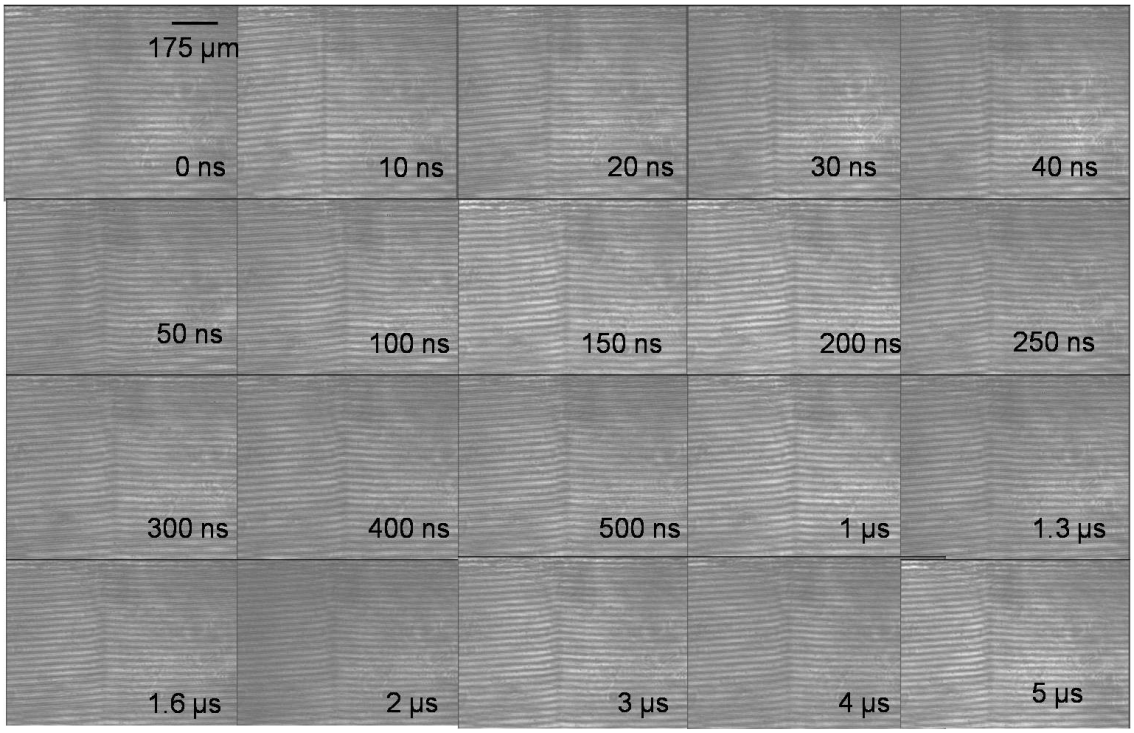

Fig. 4.16. TRIF images when a collimated nanosecond laser pulse was incident on a quartz cuvette filled with Direct Red solution. Laser spot size was 1 mm. No significant difference in the phase change was observed as a function of time.

Figure 4.17 shows microcavitation bubbles that were formed in the bulk of a Direct Red aqueous solution when a nanosecond laser pulse was incident. The absorption coefficient of the solution was $\mu_a = 22$ cm^{-1} and the energy per pulse was 5 mJ. The temperature increment associated with these irradiation conditions is ~ 3^oC, which is too low to induce a phase change at standard pressure. The influence of tensile stresses on the phase change is evident at so low temperature increment under this perspective.

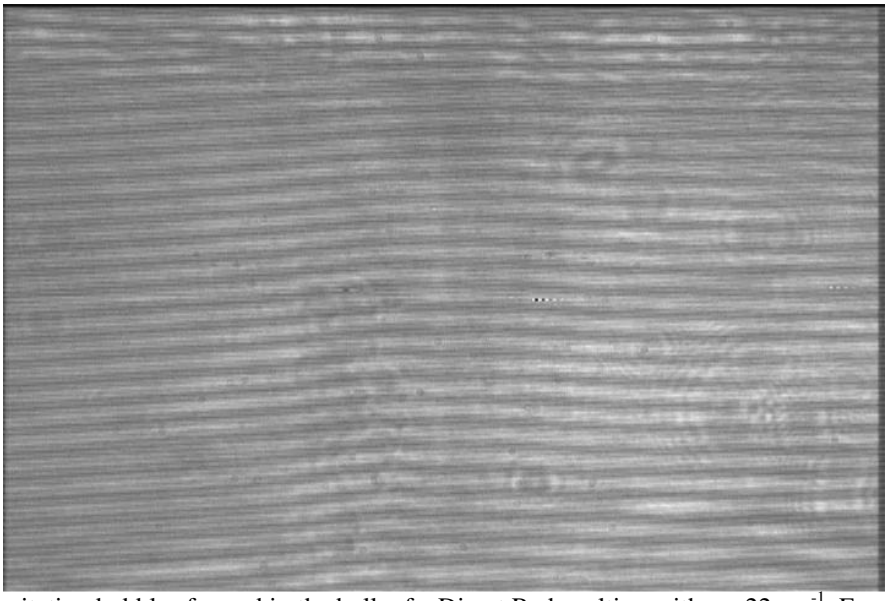

Fig. 4.17. Cavitation bubbles formed in the bulk of a Direct Red soultion with μ_a=22 cm^{-1}. Energy per pulse was 5 mJ and laser spot size 1 mm. Under such conditions the maximum calculated temperature increment was ~3 ^oC.

The fringe shape can be approximated as a triangular profile according to Fig. 4.18. The maximum refractive index change can be calculated using equation 4.2 following the procedure in [17] if the phase change is known from the interferogram.

$$\delta n_{\max} = \frac{\lambda_{\text{int}} \cdot \delta\Phi_{\max} \cdot 1.5}{2\pi \cdot 2\sqrt{R^2 - x_m^2}} \tag{4.2}$$

where δn_{max} is the maximum refractive index change, λ_{int} is the wavelength of the interferogram, $\delta\Phi_{max}$ is the maximum phase change, R and x_m can be measured from the interferogram in Fig. 4.18. The wavelength of the interferogram was measured to be λ_{int}=28 μm from an interferogram when the pump pulse was blocked (not shown). From the interferogram shown in Fig. 4.18, $\delta\Phi = \pi$, R= 1104 μm and x_m= 540 μm were measured. The resulting refractive index change with this information is δn_{max}=0.01090.

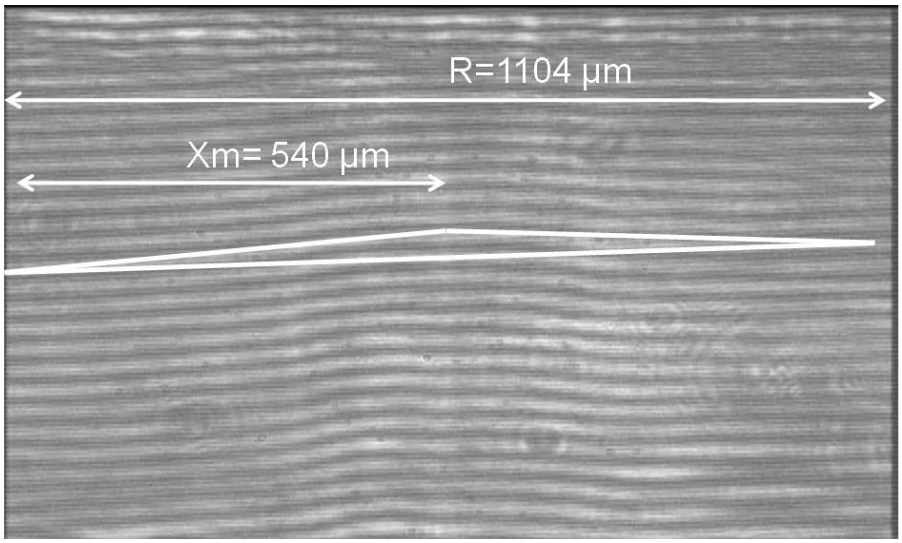

Fig. 4.18. Fringe shape can be approximated as a triangle. Using eq 4.3 and measuring the distances x_m and *R,* the maximum refractive index change can be calculated.

An empirical equation that relates the refractive index of water as a function of pressure, temperature and light wavelength was reported in [22]. For the case studied here, considering the temperature increment of 3 ^{o}C, and the 633 nm wavelength of the probe pulse, the mentioned equation reduces to equation 4.3:

$$0 = \delta n + 1.48\times10^{-5}\,\delta p - 1.89\times10^{-9}\,\delta p^{2} \tag{4.3}$$

where δn is the refractive index change and δp is pressure change in bars. Solving for δp with the refractive index change δn calculated above, results in a pressure change (decrement) of -67 MPa. Such pressure with negative sign is a tensile wave, which explains caviation bubble formation with such a low temperature increment.

What really happens is that the cylindrical irradiated volume is being stretched in the radial direction due to the thermoelastic expansion, such that the local pressure in the center of the cylinder is low enough to induce microcavitation bubbles aided by a low temperature increment. Preexisting microbubbles and impurities may serve as nucleation centers that facilitate cavitation.

Microcavitation bubbles induced in an aqueous solution of potassium chromate by a nanosecond laser pulse originating temperature increments as low as 5 ^{o}C have been studied before [5,12]. In those

experiments the laser spot size was much larger than the light penetration depth and, therefore, the compressive pressure wave that resulted from fast thermoelastic expansion of the irradiated volume surrounded by cold material was a plane wave. Such wave propagates in both directions, the optical path direction and in the opposite direction towards the solution/air interface. When the latter wave reaches the solution/air interface it encounters an acoustic mismatch because of the lower acoustic impedance of air compared with that of water, and is reflected as a tensile wave. The combination of the tensile wave and moderate temperature increments is the mechanism responsible for initiating the cavitation bubbles.

In the experiment carried out here, the laser spot size is comparable with the light penetration depth and the resulting wave from the thermoelastic expansion is a cylindrical wave. The expansion in the radial direction stretches the irradiated volume and originates tensile stresses within the interaction volume. There is actually no tensile wave propagating in this case. Even though expansion of the cylinder in the optical path direction also takes place, the radial explansion is more important. The plane wave in the optical path was not even detected with TRIF. In contrast, in the experiments in [5,12], the tensile wave is the result of the interaction of a purely compressive wave with the boundaries (water/air interface) that encounters as it propagates.

In the next chapter, the bubble formation around absorbing particles upon nanosecond laser pulse energy absorption is discussed. It is very interesting that those bubbles form when local temperature increments exceed several hundreds of degrees Celcius and also when they exceed only a few tens of degrees Celcius. For the latter case, tensile stresses may be a plausible explanation for those bubble formation

Conclusions

Mechanical effects of irradiation with nanosecond laser pulses of agar gels were studied with three experimental techniques: PVDF sensors, TRI and TRIF. It was found that the amplitude of the pressure waves detected with a PVDF sensor from 1 to 10 mm away from the beam waist has not significant difference for the agar gel concentrations tested. The pressure increments a few tens of micrometers from the beam waist are two orders of magnitude higher than 1 mm away; in other words, the pressure amplitude

decreases 2 orders of magnitude in the first millimiter of propagation. In addition a brief description of the shape for the pressure signals obtained with the PVDF sensor for the different irradiation configurations was presented. Increasing the linear absorption coefficient of the samples affected the amplitude of the signal when the beam was positioned 1 mm below the surface because plasma formation is weaker due to energy absorbed throughout the 1 mm propagation. This is a clear indication that plasma formation is the dominant interaction mechanism in these experiments. TRIF revealed the role of tensile stresses on microcavitation bubble formation when very low temperature increments (~3^{o}C) take place upon laser energy linear absorption.

References

1. Vogel A, Venugopalan V. Mechanisms of pulsed laser ablation of biological tissues. Chem Rev 2003; 103(2):577-644.

2. Niemz M. Laser-Tissue Interactions: Fundamentals and Applications. New York: Springer. 2002.
3. Welch AJ, Gemert MJCv. Optical-thermal response of laser-irradiated tissue. Kogelink H, editor. New York: Plenum press. 1995. 925 p.

4. Oraevsky AA. Laser-induced acoustic and shock waves in ocular tissues: Armstrong Laboratory, Occupational and Environmental Health Directorate, Optical Radiation Division 1995.

5. Oraevsky AA, Jacques SL, Esenaliev RO, F.K. T. Pulsed laser ablation of soft tissues, gels, and aqueous solutions at temperatures below 100°C. Lasers in Surgery and Medicine 1996; 18(3):231-240.

6. Paltauf G, Dyer PE. Photomechanical Processes and Effects in Ablation. Chem Rev 2003; 103(2):487-518.

7. Boyd RW. Nonlinear optics. Oxford: Academic Press. 2008.

8. Vogel A, Busch S, Parlitz U. Shock wave emission and cavitation bubble generation by picosecond and nanosecond optical breakdown in water. J Acoust Soc Am 1996; 100(1):1996.

9. Vogel A, Lauterborn W. Acoustic transient generation by laser-produced cavitation bubbles near solid boundaries. J Acoust Soc Am 1988; 82(2):719-731.

10. Vogel A, Lauterborn W, Timm R. Optical and acoustic investigations of the dynamics of laser-produced cavitation bubbles near a solid boundary. J Fluid Mech 1989; 206:299-338.

11. Vogel A, Nahen K, Theisen D, Noack J. Plasma Formation in Water by Picosecond and Nanosecond Nd:YAG Laser Pulses-Part I: Optical Breakdown at Threshold and Superthreshold Irradiance. IEEE Journal of Selected Topics in Quantum Electronics 1996; 2(4):847-860.

12. Oraevsky AA, Jacques SL, Tittel FK. Mechanism of laser ablation for aqueous media irradiated under confined-stress conditions. Journal of Applied Physics 1995; 78(2):1281-1290.

13. Wang YC, Chen YW. Application of piezoelectric PVDF film to the measurement of impulsive forces generated by cavitation bubble collapse near a solid boundary. Experimental Thermal and Fluid Science 2007; 32:403-414.

14. Wang YC, Huang CH, Lee YC, Tsai HH. Development of a PVDF sensor array for measurement of the impulsive pressure generated by cavitation bubble collapse. Experiments in Fluids 2006; 41:365-376.

15. Evans R, Camacho-Lopez S, Perez-Gutierrez FG, Aguilar G. Pump-probe imaging of nanosecond laser-induced bubbles in agar gel. Optics Express 2008; 16(10):7481-7492.

16. Kim B, Feit MD, Rubenchick AM, Joslin EJ, Celliers PM, Eichler J, Da Silva LB. Influence of pulse duration on ultrashort laser pulse ablation of biological tissues. Journal of Biomedical Optics 2001; 6(3):332-338.

17. Kim B, Komashko AM, Rubenchick AM, Feit MD, Reidt S, Da Silva LB, Eichler J. Interferometric analysis of ultrashort pulse laser-induced pressure waves in water. Journal of Applied Physics 2003; 94(1):709-715.

18. Martí-López L, Ocaña R, Porro JA, Morales M, Ocaña JL. Optical observation of shock waves and cavitation bubbles in high intensity laser-induced shock processes. Applied Optics 2009; 48:3671-2380.

19. Viator JA, Jacques SL, Prahl S. Depth profiling of absorbing soft materials using photoacoustic models. IEEE Journal of selected topics in quantum electronics 1999; 5(4):989-996.

20. Giao MAP, Redrigues NAS, Riva R, Schwab C. PVDF sensor in laser ablation experiments. Review of scientific instruments 2004; 75:5213-5215.

21. Perez-Gutierrez FG, Evans R, Camacho-Lopez S, Aguilar G. Short and ultrashort laser pulse induced bubbles on transparent and scattering tissue models. 2007. p 64350V64351-66435V64358.

22. Thormahlen I, Straub J, Grugull U. Refractive Index of Water Its Dependence on Wavelength, Temperature and Density. J Phys Chem 1985; 14:933-945.

Chapter 5: Plasma Membrane Integrity and Survival of Melanoma Cells after Nanosecond Laser Pulses

Introduction

Detection of circulating tumor cells (CTC) in human blood and lymph systems has the potential to aid clinical decision making in the treatment of cancer [1-4]. The presence of CTC may signify the onset of metastasis, indicate relapse, or may be used to monitor disease progression. Initial CTC detection systems were based on histopathologic techniques and have been proven to be time-consuming and subject to reviewers interpretation. Non-optical means exist for CTC detection, including Reverse Transcriptase Polymerase Chain Reaction (RT-PCR) [5,6]. Even though PCR led to increased sensitivity and specificity of detection, and removed the subjective influence inherent in earlier CTC detection methods, its clinical implementation is not feasible due to their complexity and concerns regarding the specificity of PCR in detecting CTC due to inconsistency of results and amplification of false products [5]. The use of immunohistochemestry for CTC detection relies on antibody recognition of a specific tissue-type marker of cancer-specific marker. Immunohistochemestry has shown conflicting opinions about its reliability and specificity [5]. CTC detection is still an uncertain research area and optimal detection has yet to be achieved.

Design and construction of a circulating melanoma cells (CMC) detection system is based on the fact that melanoma cells contain a great amount of melanin and fewer than 5% of melanomas are amelanotic[7,8]. Since melanin is a strong optical absorber for the whole visible spectrum[9], laser irradiation has been used to induce acoustic responses in melanin *in vivo* [10]. Based on this principle, a previous study proposed the use of photoacoustic waves for rapid and accurate *in vitro* detection of circulating melanoma cells (CMC) obtained from routine blood draws from metastatic melanoma patients [11]; the authors demonstrated that at least 10 phantom melanoma cells are necessary to maintain a strong photoacoustic signal. A more recent study attempted detection of circulating cells, nanoparticles and

contrast agents *in vivo* [12]; the authors reported threshold sensitivity as low as a single cancer cell in the background of 10^7 normal blood cells.

While *in vivo* detection becomes feasible, implementation of this concept *in vitro* has several advantages: it is fast, inexpensive and minimally invasive. *In vitro* detection entails obtaining the mononuclear cell layer (MNCL) derived from lysing and spinning a blood sample from a melanoma patient in a centrifuge. The resulting MNCL is mixed with 20 ml of normal saline and introduced into a flow system consisting of a pump, a fluid receiver, a transparent flow chamber with an integrated acoustic sensor, and a pulsed laser (λ = 450 nm; 5 ns pulse duration) system which creates the conditions for acoustic wave generation [11]. Unfortunately, while larger fluences inevitably result in stronger photoacoustic signals, thus increasing the signal-to-noise ratio (SNR), excessively high optical absorption inside the CMC produces localized laser-heat generation that may lead to bubble formation. Bubble formation inside cells may lead to plasma membrane damage, thereby allowing melanin to leak from the cell, and thus preventing continuous photoacoustic detection. The ideal operation condition for a system of this type in a clinical application is to have a continuous detection. For this, it is necessary to ensure that the plasma membrane remains undamaged after laser irradiation, so the melanin does not leak from the cell and diffuse into the circulating solution, reducing the SNR of the photoacoustic signal.

Survival of pigmented melanoma cells after irradiation with laser pulses of 40 ns and 300 μs at λ=694 nm has been studied before [13]. The authors compared the effects of pulse duration using melanoma cells of a mouse pigmented melanoma cell line (B-16) and a human non-pigmented melanoma cell line (FaDu). It was found that pigmented melanoma cells died only when irradiated with 40 ns pulses, whereas the non-pigmented cells remained viable for both pulse durations. In addition, they demonstrated acoustic wave transients when 8.5 ns laser pulses at λ=532 and 625 nm were used; these transients are from 2.5 to 3-fold higher for λ=532 nm wavelength as compared to 625 nm; however melanosome's optical absorption coefficient at λ=532 nm is only 1.75 times higher as compared to λ=625 nm according to the experimental expression $\mu_a = 1.70 \times 10^{12} \lambda^{-3.48}$ presented in reference [9], where μ_a is the absorption coefficient

and λ is the wavelength expressed in nanometers. Unfortunately they did not show data for cell survival after irradiation with 8.5 ns.

There are experimental [14,15], numerical [16] and theoretical [17] studies that focus on bubble formation around microabsorbers, such as melanosomes and absorbing microbeads in water after laser irradiation with nano- and micro-second pulse durations. Experimental studies [18-21] have revealed that: (a) the threshold fluence for bubble formation increases with pulse duration as heat transfer increases; and (b) there is a transition from bubble-driven (mechanical) to protein denaturation-driven (thermal) cell death as the pulse duration is longer. These studies, however, focused on retinal pigment epithelium (RPE) melanosomes. Thus the motivation for work presented in this manuscript is the lack of equivalent information melanoma cells from cutaneous origin.

It has been proven that CTC's are photoacoustically detectable using laser pulses of 5 ns duration, 450 nm wavelength, and 0.450 J/cm^2 fluence [11]. However, this wavelength is difficult to obtain at that pulse duration, as it requires a frequency-tripled Q-switched laser system to pump an Optical Parametric Oscillator (OPO). An OPO is a complex nonlinear optical system that increases by a factor of two the cost of the laser system used for photoacoustic excitation-detection of CTC's, and it requires maintenance from experienced technicians.

The purpose of this work is to better understand the laser-melanoma cell interactions to assist on the design of an *in vitro* photoacoustic CTC system developed specifically for pigmented melanoma cell detection. The specific objectives of the present work on human melanoma cells are to:

(a) Determine melanoma cell survival after laser pulses of 6 ns [11] at wavelengths that are feasible to obtain (e.g., second and third harmonics of a Nd:YAG, Q-switched laser: λ = 532 and 355 nm), and where melanin is still a high linear optical absorber (the 1 ns difference between the pulse duration in some of the experiments in this work and those in reference [11] should not be of consideration).

(b) Study a potential enhancement of the photoacoustic signals using λ=355 nm in comparison to λ=532 nm, since melanin linear absorption at 355 nm is higher than at 532 nm by a factor of 4.

(c) Determine whether melanin leaks from melanoma cells and the critical laser fluence at which this happens, which would adversely affect the SNR of continuous photoacoustic detection.

(d) Develop a time-resolved imaging system with nanosecond resolution to study the intracellular interactions (e.g., laser-induced bubble formation) within the melanoma cells, and their effect on the plasma membrane integrity. This on view that the main concern for the *in vitro* melanoma detector is melanin leakage from the cell.

Materials and Methods

Cell culturing and sample preparation

HS936.T (C1) cells were grown as a monolayer in Dulbecco's Modified Eagle Medium (American Type Culture Collection ATCC, Manassas, VA) with 10% horse serum and 1% of Penicillin-Streptomycin on 6-well cell culture clusters until the culture was confluent. Media was changed every other day. Incubator atmosphere was at 37°C, 5% CO_2 and 90% humidity. Cell monolayers were rinsed with Phosphate Buffered Saline (PBS), and harvested from tissue culturing wells adding Cellstripper (Mediatech, Inc., Herndon VA) and incubating for 5 min at 37°C. The cells were resuspended in PBS at a concentration of 2.5×10^6 cells/ml, and sedimented by low-speed centrifugation. Cells were washed and resuspended in PBS twice, and placed on 24-well tissue culture treated clusters at cell density of 500 cells/ mm^2.

Laser Irradiation

Figure 5.1 shows a schematic of the optical system used to irradiate the samples. Laser irradiation was performed using a Q-switched, Nd:YAG laser and it also has three high power output ports for the fundamental, second and third harmonics; 1064, 532 and 355 nm wavelengths, respectively.

The second harmonic laser beam delivered to the cell cultures was collimated and resized to $1/e^2$ spot diameter of 1 mm, using a combination of a convergent LC (f = 125 mm) and a divergent LD (f = -50

mm) lens. The energy per pulse was varied using an attenuator made of a half wave plate HWP1 and a polarizer P1, and it was monitored with a previously cross calibrated energy meter EM (Ophir, Logan, UT) to a second energy meter placed at the target's position. The sample was mounted on a 3D translation stage that allowed easy repositioning of the sample. By means of a pellicle beam splitter BS, in line with the Nd:YAG beam, a continuous wave (CW), 0.5 mW, 543 nm wavelength He-Ne laser (Thorlabs, Newton NJ) served as aiming beam. A total of 4 pulses were delivered to each sample. Each pulse was delivered at a fresh site, therefore, a single cell was never irradiated more than once. Cells were not irradiated using a single pulse with a large spot size because with such a large spot, the laser fluence that can be achieved with our laser is not high enough to induce damage to the cells. Laser irradiation with the third harmonic (λ = 355 nm) was possible by removing the mirror RM and it was carried out in the same way as it was done with the second harmonic. The distance between lenses LC and LD was adjusted to give the same spot size (as in the second harmonic case) at the sample and the delivered energy was adjusted by using various neutral density (ND) filters.

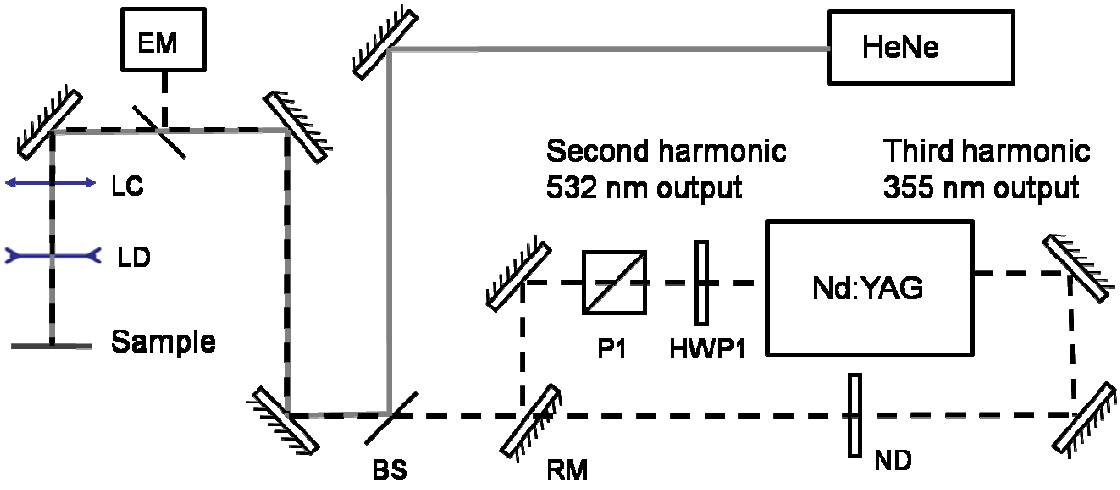

Fig. 5.1. Experimental set up for laser irradiation of melanoma cells with nanosecond laser pulses with λ=355 and 532 nm. Second or third harmonic was delivered to the sample inserting or removing the removable mirror (RM). HeNe laser serves as aiming beam. Target's holder was displaced in the X-Y direction to provide four laser pulses to each sample without overlapping of laser exposure on the same cells.

Cell damage determination

Immediately following laser irradiation, a 0.08% solution of Trypan blue, used as a viability assessment dye, was added to the whole sample, including irradiated and non irradiated cells. Cells were collected from the well cluster and counted using a hemacytometer. The reactivity of Trypan blue is based on the fact that the chromophore is negatively charged and does not interact with the cell unless the membrane is damaged. Therefore, all the cells which exclude the dye are undamaged. Control samples were kept without laser irradiation during the experiment. Long-term effects were not considered as they are irrelevant for continuous photoacoustic CTC's detection.

Melanin leakage determination

Immediately following laser irradiation, samples of cells and PBS were collected in Eppendorf tubes. Cells and PBS were then separated by centrifugation at 8000 *g* for three minutes. Absorbance of the resulting mixture of PBS and melanin from the control and laser-irradiated samples was measured in a Nanodrop spectrophotometer (Thermo Scientific, Wilmington DE) at 220 nm. This spectrophotometer was chosen because it handles sample volume about 3 µl. Differences in PBS absorbance as a function of laser fluence with respect to control samples indicate that there is melanin diluted in PBS that came from the laser-damaged cells.

Comparison of photoacoustic signals for λ = 355 and 532 nm

To compare the amplitude of the photoacoustic signal produced by both wavelengths, the experimental set up shown in Figure 5.2 was built. Either the second or the third harmonic from a Surelite OPO PLUS (Continuum, Santa Clara, CA), Nd:YAG, Q-switched laser system that emits 5 ns laser pulses was used. The laser beam was focused into a 1 mm spot diameter through a focusing lens and reflected through a right angle prism onto an acrylic well holder positioned on top of a laboratory made, unfocused type, polyvinylidene fluoride (PVDF) ultrasonic transducer with sensitivity 0.71 mV/bar. The well holder contained 50 µl of a 1% intralipid acrylamide disk that was used to protect the transducer. 25 µl of sample suspension was pipetted into the well for testing and a newly made scattering disk was used for each

individual test. The signal from the PVDF transducer was sent to a signal amplifier and then into an oscilloscope.

The concentration used for each test was 1 x 10^6 cells/ml of suspension. The total irradiated volume was 1 µl so the total number of cells irradiated was 1000. In addition, to lessen the effects of cell clumping, the cells were irradiated while suspended in Tryple E.

The photoacoustic signal was quantified as the integrated pressure, which is the result of integrating the oscilloscope trace from 1.6 to 2.5 µs, which is the calculated acoustic depth of the irradiation well. Integrated pressure units are [volts*seconds]. The thickness of the acrylimide scattering disk was 2.5 mm at the middle. There are some curved effects due to the cuvette being 4.5 mm in diameter due to fluid adhesion. The thickness of the samples was 1.25 mm in the middle it was half since the disk was loaded with 50 uL and 25 uL for the sample. A typical absolute waveform taken at 1 J/cm^2 at 32 dB amplification is shown in Figure 5.3.

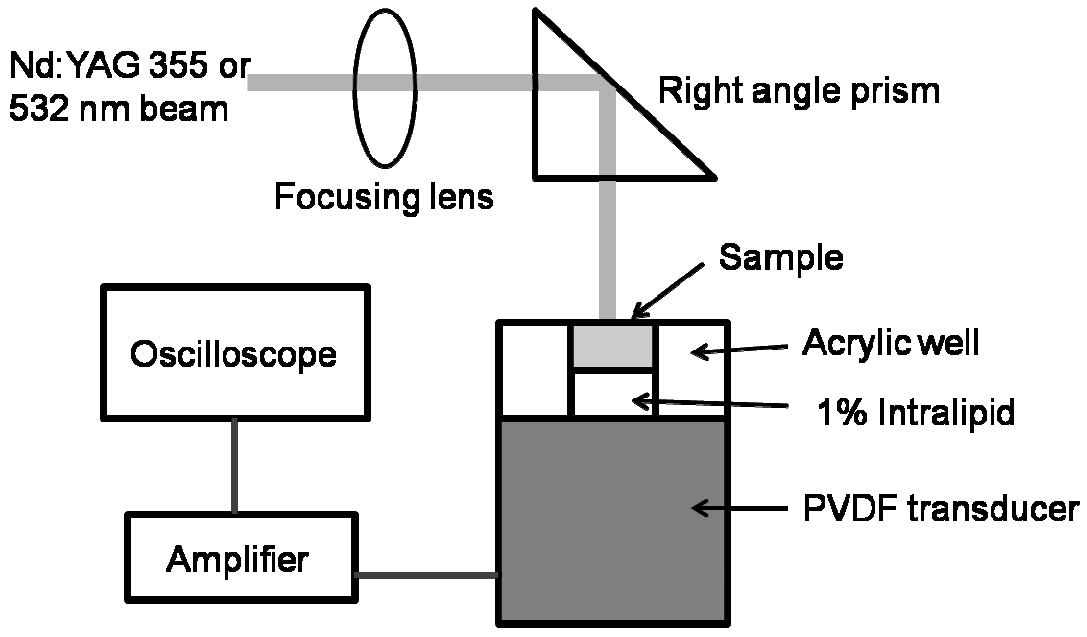

Fig. 5.2. Experimental set up for comparison of photoacoustic pressure at λ=355 nm and λ=532 nm. The

laser pulse is brought to the melanoma cells (sample) through a focusing lens and a prism. The cells are contained in an acrylic well and diluted in Tryple E to avoid cell clumpling. The PVDF ultrasonic transducer is protected from laser damage with a 1% intralipid acrylamide disk.

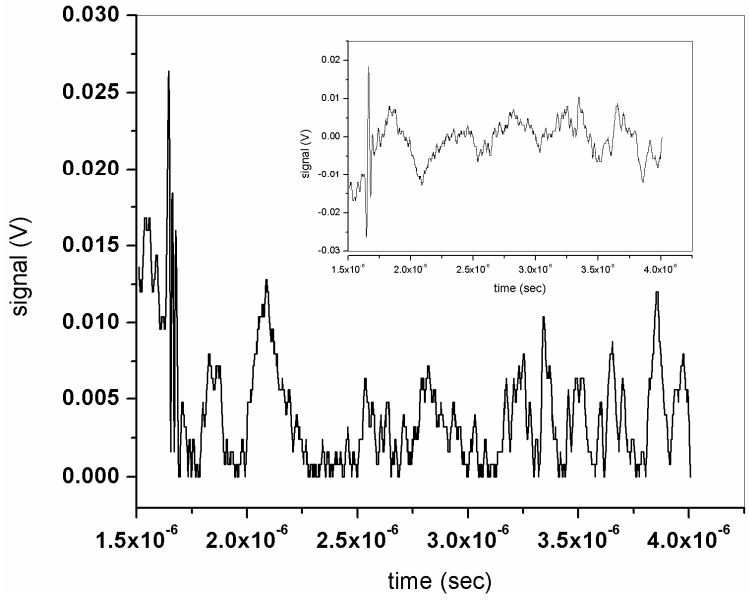

Fig. 5.3. Absolute value of a typical waveform obtained with oscilloscope for comparison of photoacoustic signal at λ=355 and 532 nm. Signal was integrated from 1.6×10^{-6} to 2.5×10^{-6} sec to include the calculated acoustic depth of the irradiation well. Laser fluence was 1 J cm^{-2}, λ= 532 nm and data acquisition was at 32 dB amplification. Inserted figure shows the raw signal as it was acquired with the oscilloscope.

Time-resolved imaging of laser irradiated cells

The experimental setup for TRI of laser-cell interaction is shown in Figure 5.4. It consists of two nanosecond laser systems electronically synchronized. The first, used as the pump, was the EKSPLA laser system previously described (Nd:YAG 1). The second, used as probe, was a Brilliant (Quantel, Les Ulis Cedex, France), Q-switched, Nd:YAG laser that emits 6 ns laser pulses at the fundamental λ=1064 nm (Nd:YAG 2). This probe wavelength was chosen because melanin has lower absorption as compared to 532 and 355 nm.

Both beams were brought co-linear onto the sample. The green/UV pump beam was resized by means of lenses LC (f = 125 mm) and LD (f = -50 mm) to increase laser fluence on the sample. The delivered energy was varied and recorded in the same way than for the cell damage experiment. The probe beam was slightly focused onto the sample with lens L1 (f = 250 mm). A magnified image of the sample is formed by an aspheric lens L2 (f = 6 mm) and L3 (f = 400 mm) onto a charged coupled device (CCD) camera (Hamamatsu, Lake Forest, CA). A long-pass filter with cut-off wavelength at λ=610 nm (RF) positioned in front of the CCD blocked scattered light from the green pump beam.

The delay generator DG provided the electronic pulses required to externally trigger both laser systems at 10 Hz repetition rate with a relative delay. Single laser pulses from the pump beam are selectively released by a mechanical shutter (MS) (Uniblitz, Rochester, NY) that opens its aperture for 100 ms, therefore allowing only one laser pulse pass through it. Simultaneously, the signal out of the SG is divided and also sent to trigger the CCD whose exposure time was set to 100 ms. This exposure time and the long-pass filter guarantee that only light from the probe pulse is captured by the CCD.

The pump laser beams for these experiments have a Gaussian intensity profile with $1/e^2$ diameter of 910 μm. The diameter of the pump and probe laser beams overfill the CCD field of view.

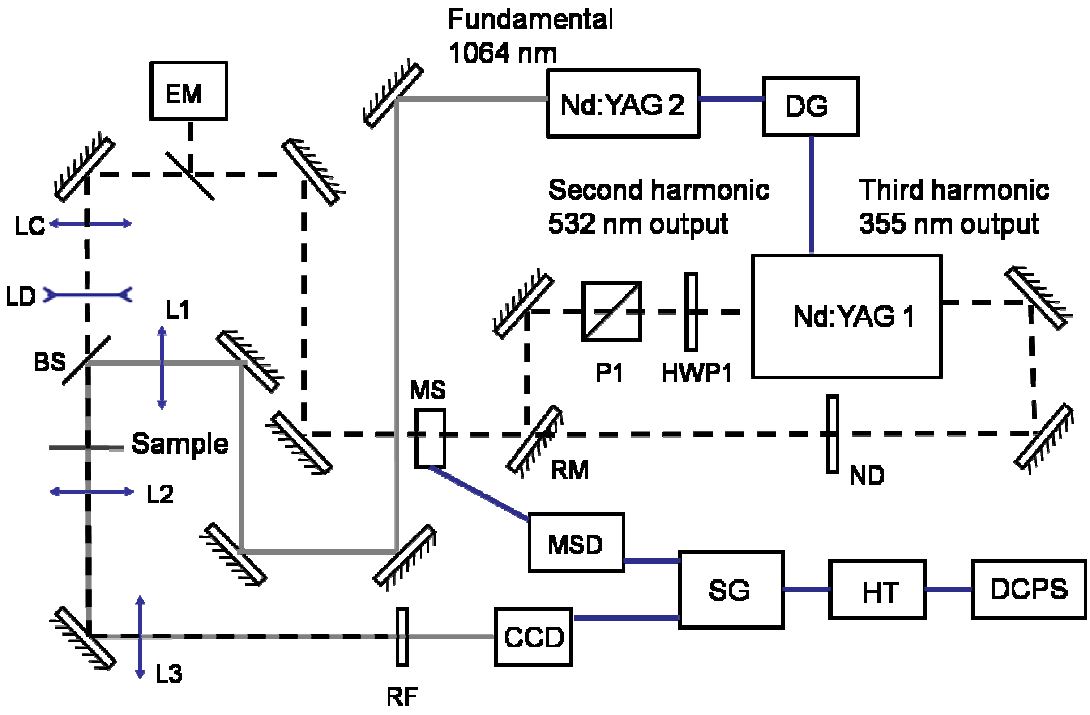

Fig. 5.4. Experimental set up for time-resolved imaging (TRI) of melanoma cells. Lasers Nd:YAG 1 as pump (λ=355 or 532 nm) and Nd:YAG 2 as probe (λ=1064 nm) are externally triggered and synchronized by delay generator (DG) at 10 Hz repetition rate. Second or third harmonic from Nd:YAG 1 laser is released to the sample inserting or removing removable mirror (RM). Mechanical shutter (MS) and CCD camera are triggered by a signal generator (SG); both, MS and CCD camera's shutter are open for 100 ms to ensure that only one pump and one probe pulses irradiate the sample and get to the camera respectively, when the lasers are triggered at 10Hz repetition rate.

Results

Cell damage determination

Figure 5.5 shows the normalized cell survival of melanoma cells as a function of the average fluence of the 4 laser pulses incident on each sample at 532 and 355 nm wavelengths. Cell survival is calculated according to

$$C = \frac{N_{undamaged}}{N_{damaged} + N_{undamaged}} \tag{5.1}$$

where C is cell survival, $N_{undamaged}$ is the number of undamaged cells and $N_{damaged}$ is the number of damaged cells. The denominator in equation 5.1, the sum of $N_{undamaged}$ and $N_{damaged}$, is the total number of

cells per well, not the total number of irradiated cells. Cell survival of irradiated samples was normalized with respect to the average cell survival of control samples, which were not irradiated at all.

In the range of laser fluences used for photoacoustic detection of melanoma cells in suspension, we found that the amount of undamaged cells decreases by 40% and 50% for the 532 nm and 355 nm wavelengths with increasing fluence, respectively. The decay of cell survival at both wavelengths is described by exponential curves. The slopes of both curves were found to have significant difference when compared through nonlinear, one phase exponential decay fit with $p<0.0001$ using GraphPad Prism v.5.00. Nevertheless, for the highest fluences, cell survival tends to be the same value at both wavelengths; this means that for such high fluences, the higher absorption for the shorter wavelength is no longer important.

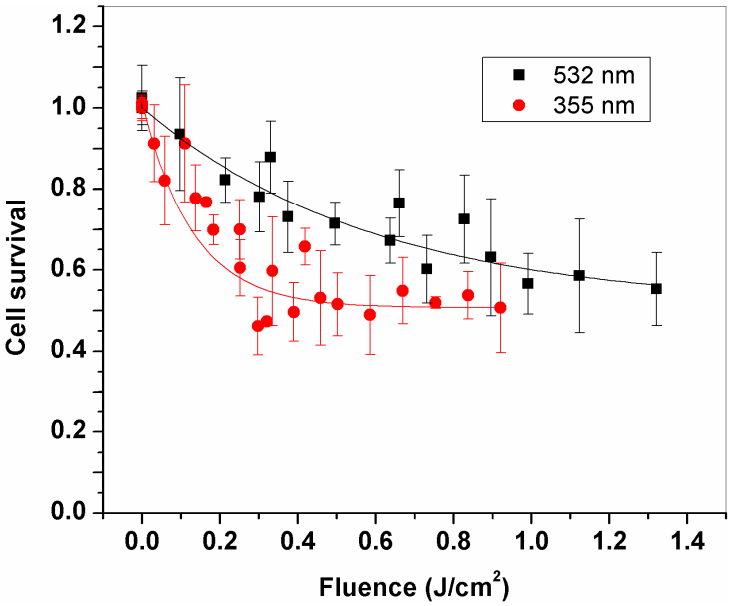

Fig. 5.5. Normalized cell survival of melanoma cells irradiated with 6 ns laser pulses with λ= 355 and 532 nm. Significant difference was found in the curves for both wavelengths according to statistical analysis with $p < 0.0001$. Cell survival was normalized according to equation 2 (see body of the text), where the total number of the cells in the sample, and not only cells reached by laser, contributed to the calculation. Each data point is the average of 5 measurements with its corresponding error bars.

Melanin leakage determination

Figure 5.6 shows absorbance values of the resulting mixture of PBS and melanin when human pigmented melanoma cells were irradiated. Data is shown normalized with respect to the average of the resulting mixture absorbance of control samples. It is plausible that the large dispersion of data is due to the variable amount of melanin contained in melanoma cells, just as it is for melanosomes [9]. However, it is evident that PBS absorbance increases with increasing laser fluence, suggesting that plasma membrane is being damaged by the laser pulse and thus melanin is leaking from the cell.

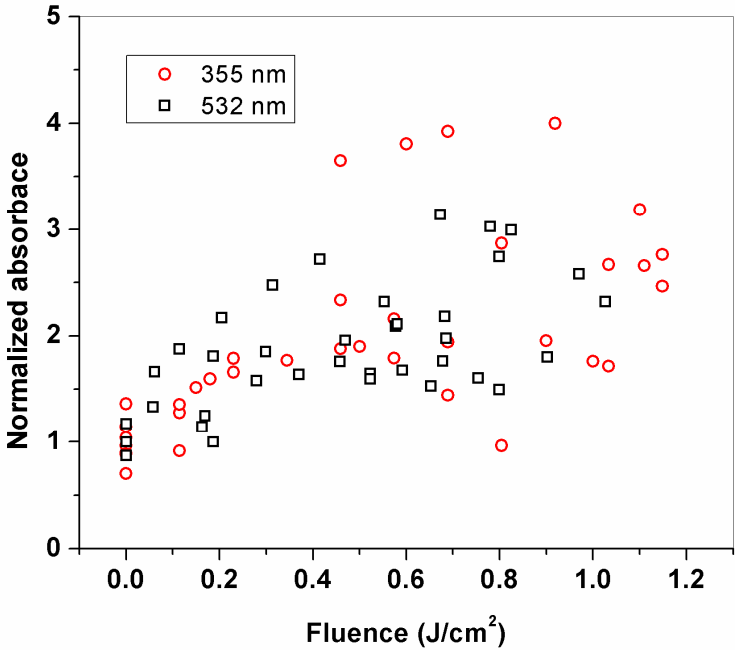

Fig. 5.6. Normalized PBS absorbance as a function of laser fluence. Absorbance was measured using a nanodrop spectrophotometer with λ=220 nm. Laser irradiation was carried out at λ = 355 and 532 nm. Data normalization was done with respect to the average of data points obtained with control samples (fluence = 0).

Comparison of photoacoustic signals for λ = 355 and 532 nm

Figure 5.7 shows the integrated pressure generated by the laser-cell interaction as a function of laser fluence for both wavelengths tested. Each data point is the result of averaging 5 sets of data acquired; each data set is the average of 16 laser shots. As expected, the integrated pressure increases with fluence for both wavelengths. However, the dependence of the integrated pressure on wavelength is not obvious at first

sight; therefore, a two-way ANOVA was performed (with α=0.05) twice: first by considering the whole data up to 1 J/cm^2 and, second, by only considering fluences up to 0.6 J/cm^2.

The resulting *p* values from the first two-way ANOVA for the two individual factors in the experiment (wavelength and fluence) are 0.9942 and <0.0001, respectively, whereas the *p* value for the interaction between them is 0.0011. Such *p* values indicate that while the fluence and the interaction between fluence and wavelength are statistically significant for predicting the integrated pressure, the wavelength by itself is unimportant. In contrast, for the second ANOVA, the *p* values were 0.007 and < 0.0001 for wavelength and fluence, respectively, whereas for the interaction of both the *p* value was 0.2737, meaning that both fluence and wavelength are statistically significant for the integrated pressure prediction, whereas the interaction between them is not.

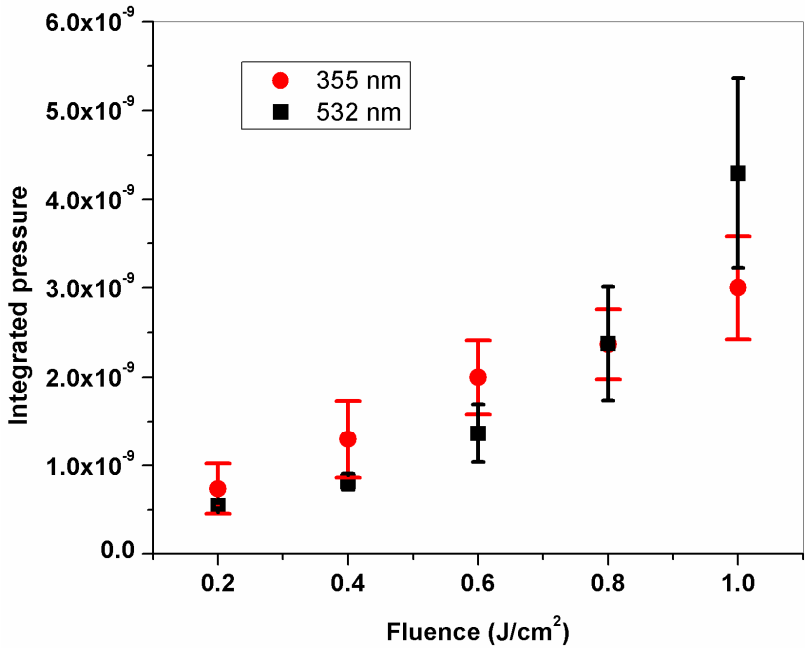

Fig. 5.7. Comparison of photoacoustic signal for λ=532 nm and λ=355 nm as a function of fluence. Wavelength was found to be a variable with no statistically significance to the integrated pressure obtained.

Time-resolved imaging of melanoma cells

TRI allowed imaging melanoma cells a few nanoseconds right after its interaction with the pump laser pulse. Fig. 5.8 shows images taken: (A) before, (B) 50 ns after melanoma cells were irradiated using a 6 ns laser pulse with fluence of 0.3 J/cm^2 at λ=355 nm. (B) shows the melanoma cell when "boiling" bubbles are being formed within the cell.

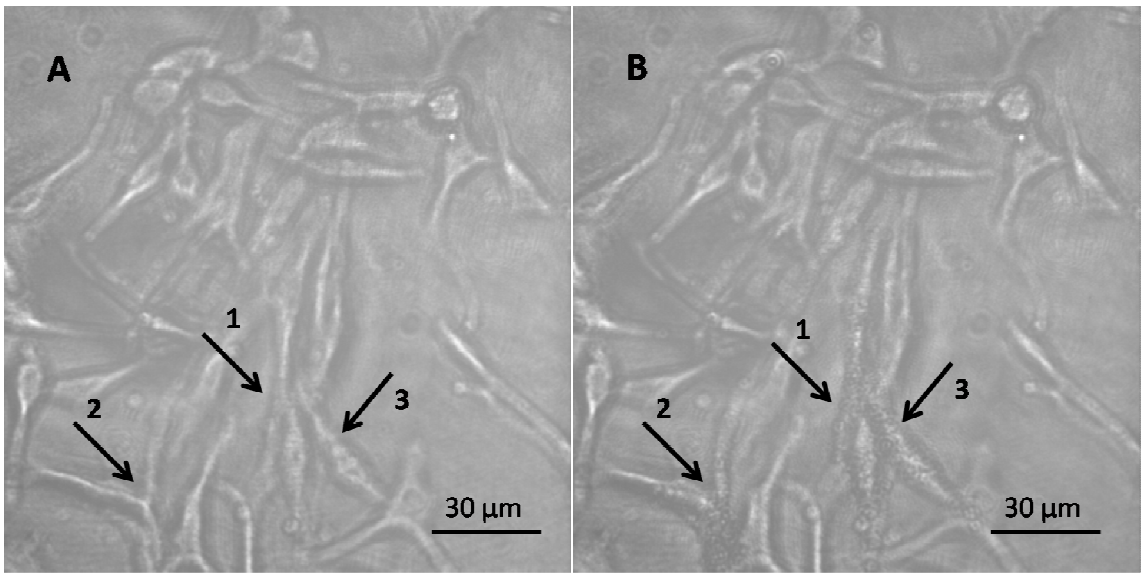

Fig. 5.8. Time-resolved imaging of melanoma cells **(A)** before and **(B)** 50 ns after a single, 6 ns laser pulse, λ=355 nm, 0.3 J/cm^2 was delivered to cells. Arrows in part **A** show undamaged cells before laser exposure; arrows in part **B** clearly show cells where microbubbles were induced by the laser pulse.

Figure 5.9 shows images (A) before, (B) 50 ns after irradiation using a 6 ns laser pulse with fluence of 0.65 J/cm^2 at λ=532 nm. Arrows in Fig. 8A show the melanoma cells without damage prior to laser exposure. Arrows in Figure 8B show the same cells post laser exposure when the plasma membrane has been obviously damaged. These results show solid evidence of plasma membrane damage after irradiation with 6 ns laser pulses for both laser wavelengths.

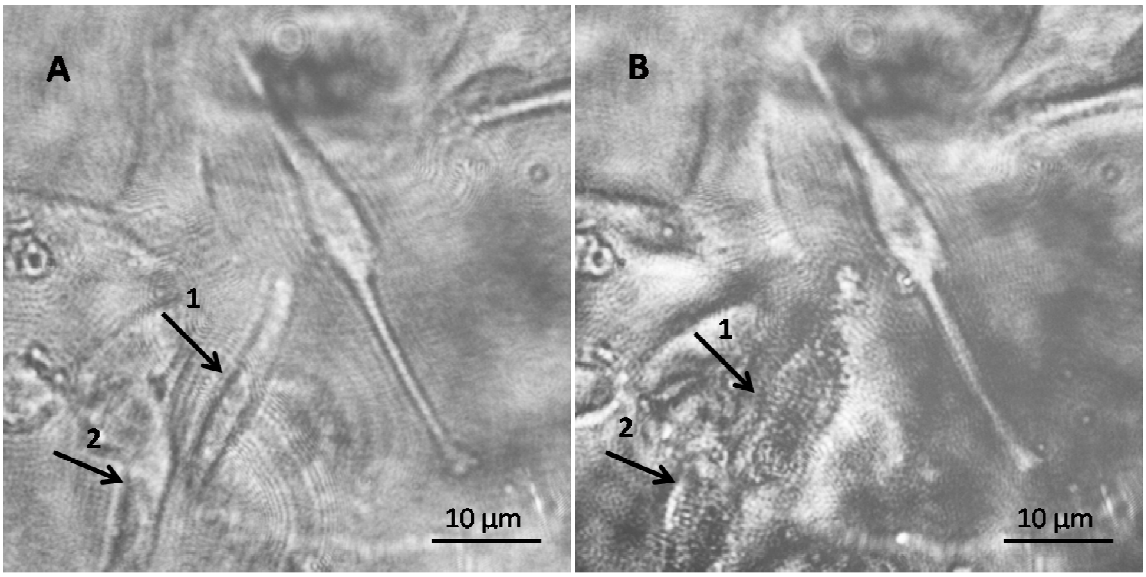

Fig. 5.9. Time-resolved imaging of melanoma cells **(A)** before and **(B)** 50 ns after a single, 6 ns laser pulse, λ=532 nm, 0.65 J/cm^2 was delivered to cells. Arrows in part **A** show undamaged cells by laser exposure, arrows in part **B** clearly show cells that where the plasma membrane was totally destroyed by microbubbles induced by the laser pulse.

Discussion

Our results show that the amount of undamaged cells after laser irradiation decreases from 40 to 50 % in an exponential decay as a function of delivered fluence. At λ=355 nm, the amount of cells that survive laser irradiation did not decrease further for fluences higher than 0.35 J/cm^2, while at 532 nm the amount of undamaged cells does not decrease for fluences higher than 1 J/cm^2. It is worth to notice that for the higher fluences cell survival tends to the same value. For such fluences, the error bars for both wavelelengths in Fig. 5.5 overlap. The reason for this is because four pulses were delivered to each sample, but the samples were displaced after each pulse, so any given region within the sample received only one pulse and adjacent regions may have not been reached directly by the laser beam. Therefore, the fact that the amount of undamaged cells did not change after certain fluence indicates that all the cells reached by pulses at or above such fluence were killed. It should be mentioned here that all the cells in the sample contributed to calculate the cell survival percentage. A very similar curve was obtained irradiating mouse melanoma cells (B-16) with 40 ns laser pulses at 694 nm in a previous study, although their methodology

for laser irradiation and assessing cell survival was different [13]. It is worth noting that in this study, we use shorter laser pulses and wavelengths. Therefore, it is reasonable to expect stronger laser-melanosomes thermomechanical interactions.

In a related study where single blast-transformed lymphocytes were irradiated with a similar laser pulse duration than in our experiments, the authors tested three different methods to detect damaged cells [22]. They found differences in the amount of cells damaged by pulses of the same energy, suggesting that some cells of the same kind are more susceptible to laser damage than others. This may be a plausible explanation for our experiments too since we observed as much as 20% variation in damage for the same laser fluence and wavelength.

Measurements of absorbance of the mixture of melanin and PBS (Fig. 5.5) showed that its absorbance increased as laser fluence increased. We observed up to a 4-fold increase in the PBS absorbance for the higher fluences tested with respect to the control samples. Data obtained showed large dispersion due to the inherent variability of melanin contained in melanoma cells, just as it is for melanosomes [9]. It was not possible to establish a dependence of melanin and PBS mixture absorbance with the wavelength used to irradiate the cells, meaning that both wavelengths damage the cells and melanin consequently leaks from them. None of the previous studies about interactions of pigmented melanoma cells or RPE with Q-switched nanosecond laser pulses reported melanin concentration in the cell culturing/PBS medium post laser irradiation.

Data of integrated pressure as a function of fluence up to 0.6 J/cm^2 in Fig. 5.7 indicates that the 355 nm wavelength offers an advantage to maximize the SNR compared with the 532 nm, as expected due to the 4-fold increment in the melanin absorption coefficient at that wavelength. This is in agreement with the information provided in Fig. 5, where cell survival up to that wavelength is clearly higher for 532 nm as compared to the 355 nm.

The cross over of the integrated pressure in Fig. 5.7 for fluences higher than 0.6 J/cm^2 can be attributed to the fact that the total number of cells reached by the laser pulse are damaged at 355 nm,

whereas there are still undamaged cells reached by laser at 532 nm, as shown in Fig. 5.5. The integrated pressure measured in these experiments has two components, the photoacoustic pressure resulting from thermoelastic expansion of the melanosomes within melanoma cells and the pressure originated by the so called "giant photoacoustic effect" resulting from bubble formation around laser-heated particles. This effect has been reported before [23,24] and the references therein. The pressure resulting from the giant photoacoustic effect has been proven to be higher than that from thermoelastic expansion of heated particles [23].

Stress confinement conditions are met when the laser pulse is shorter than the acoustic characteristic time and therefore the energy cannot propagate mechanically out of the interaction volume. A theoretical model proposed by Oraevsky [25] calculates the pressure radiated due to thermoelastic expansion of a melanosome under such conditions. The pressure amplitude is determined by the rate of thermal energy deposition.

$$P = \frac{3}{16\pi} \cdot \frac{E_{abs} \beta c_s}{c_p r_o R \tau_p} \tag{5.2}$$

where E_{abs} is the absorbed energy that can be calculated as the product of the absorption coefficient, the laser fluence and interaction volume; β, r_o and c_s are the volumetric expansion coefficient, radius and speed of sound of the melanosome, respectively, R is the distance from the melanosome surface, and τ_p is the laser pulse duration. For a melanosome 1 μm in diameter, the acoustic characteristic time is 0.7 ns, one order of magnitude shorter than the 6 ns laser pulses used for these experiments and therefore stress confinement conditions are not met. Both, thermal expansion coefficient and speed of sound in melanosomes are unknown and data from some polymers are used for this model [15].

For the simplest case in these experiments, for a melanosome positioned at the surface of the scattering disk, the pressure radiated as a function of laser fluence varies by a factor of four from the 355

nm to the 532 nm wavelengths. Figure 5.10 shows a qualitative comparison of the theoretical model with the experimental data in Figure 5.7. The inset shows the results from the model while the main figure shows the experimental results. Only a qualitative comparison is valid since the units of the experimental data are volts*seconds whereas the resulting units from equation 5.2 are Pascals. The model agrees well with the experimental data for fluences lower than 0.6 J/cm^2. The pressure for both wavelengths increases linearly with laser fluence, being the pressure for 355 nm higher than that of 532 due to the four-fold difference in the absorption coefficient of melanin at the first wavelength with respect to the second. This is a regime in which the pressure due to the thermoelastic expansion of the melanosomes is dominant over the pressure radiated by the bubble expansion. For fluences higher than 0.6 J/cm^2, pressure from bubble expansion, described as the "giant photoacoustic" effect previously mentioned, is dominant over thermoelastic expansion.

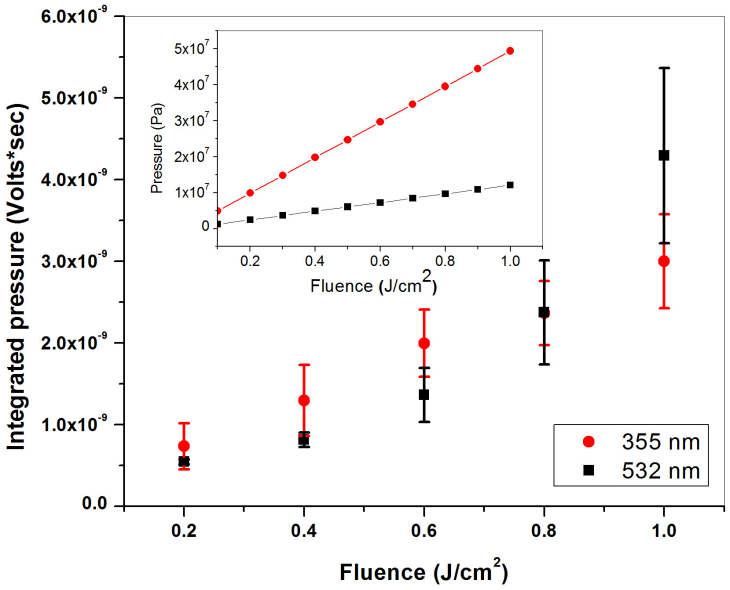

Fig. 5.10. Qualitative comparison of experimental data (main figure) with results from theoretical model in equation 5.2 (inset figure). Reasonable agreement between the model and experiments for fluences lower than 0.6 J/cm^2 is observed. Both curves increase linearly with fluence.

There could be various mechanisms that damage cells due to laser irradiation with a few nanosecond-long laser pulses. Temperature increment within CMC due to linear absorption of laser light by melanosomes can be calculated under thermal confinement conditions, when the optical absorption coefficient is well known [26].

$$\Delta T = \frac{\mu_a F}{\rho C_p} \tag{5.3}$$

Where ΔT is temperature increment, μ_a is the optical absorption coefficient of melanosomes at the irradiation laser wavelength, F is fluence or radiant exposure, and ρ and C_p are density and specific heat at constant pressure of CMC, respectively. As the different absorbers within a cell are of submicron scale (melanosomes containing melanin, in our case), thermal confinement conditions require the pulse duration to be shorter than the thermal relaxation time, defined as [22,27]

$$\tau = \frac{d^2}{\alpha} \tag{5.4}$$

where τ is thermal relaxation time, d is characteristic length and α is thermal diffusivity. For a melanosome 1 μm in diameter [16] and thermal diffusivity of 1.37×10^{-7} m^2/s [28], relaxation time is 7.3 μs, which is three orders of magnitude longer than our 6 ns laser pulses; thus thermal confinement conditions are fulfilled in our experiments. Although some authors provide other definitions of thermal relaxation time [18,29], with the melanosome size and thermal diffusivity presented here, the thermal relaxation time is two orders of magnitude longer than the laser pulses used for these experiments. Even though more complex theoretical heat transfer models have been developed to study radial and temporal temperature distributions surrounding laser irradiated absorbing microspheres [14,17-19,26], the approximation provided by equation (5.3) is valid for the purposes of the current study.

Thermal denaturation of biomolecules in the cell may also be another mechanism of cell damage. Protein denaturation kinetics has been studied within a time resolution of several hundred of

microseconds.[29] For thermal denaturation, an extrapolation of the Arrhenius equation leads to denaturation temperatures between 370 and 470 K for time range from pico- to nanoseconds. This temperature range is well above the threshold for bubble formation around melanosomes; in other words, like in the case studied here, it will be very difficult to kill cells thermally in the nanosecond time regime.

The most likely damage mechanism for the case studied herein is expansion of laser-induced bubbles inside cells around melanosomes. Laser-induced bubbles without optical breakdown formation have two possible formation mechanisms: boiling and/or cavitation [14,15,30,31]. As melanoma cells contain a large amount of melanosomes (containing melanin), these serve as nucleation centers for bubble formation. When bubbles around single melanosomes expand they merge forming larger bubbles that disrupt the cell membrane as they expand. Boiling nucleation on melanosomes and absorbing beads has been studied previously [14,15]. In these studies, experimental results show that the threshold fluence for bubble formation decreases linearly with increasing ambient temperature for different laser pulse durations. The authors extrapolated their data and showed that a bubble is formed around the melanosomes for 12 ns pulse duration at 532 nm wavelength when a temperature of 136 ± 23 ^{o}C is reached. Table 5.1 shows calculations of the temperature increment calculated with Equation 5.2 for the lowest and highest fluences used in our experiments, considering the thermal properties in [27] and the absorption coefficients of skin melanosomes in [9] and not retina melanosomes. Our calculations show that the temperature increments were well above the reported nucleation temperatures for the highest fluence, whereas with the combination of lowest fluence and absorption coefficient, temperature increments were near and below nucleation temperatures.

Table 5.1. Temperature increment and properties of CMC calculated according to Eq. 5.3. Properties of melanosome extracted from indicated references.

λ [nm]	**Reference**	**μ_a** [cm^{-1}]	**F** [J cm^{-2}]	**ΔT** [K]
532	[9]	555	1.3	213
	[9]	555	0.063	10
355	[9]	2268	0.912	610
	[9]	2268	0.063	42

Another study reports detection of laser-induced bubbles in hemoglobin solution and in individual red blood cells at temperatures as low as 30°C [26]. Other authors have experimentally studied bubble formation at temperatures below 100°C in absorbing solutions, gels and soft tissues [30,31]. Under stress confinement conditions, tensile stresses are responsible for a change of phase below 100°C, thereby reducing the threshold fluence for bubble formation. Tensile stresses in those experiments are the result of the material optical properties and experiment geometry, in which a compression wave experiments a reflection with opposite sign becoming a tensile wave because of the acoustic mismatch at the boundary. For a melanosome 1 μm in diameter and with acoustic velocity of water, the acoustic confinement time is about 0.7 ns, which is one order of magnitude shorter than the pulse duration in these experiments; however, if two melanoma cells 10 or 20 μm in diameter contained a large amount of melanosomes and were very close to one another, then an acoustic characteristic length in the order of the cell size can be considered, and stress confinement conditions could be fulfilled. Although the complex geometry of the interior of individual cells makes it difficult to affirm that this is the case herein, this mechanism for laser-induced bubble formation inside cells has been proposed previously [26], and some of our data for low fluence combined with the low absorption coefficient of melanosomes seem to suggest that this mechanism is indeed plausible.

In the study where a similar experiment with melanocytes was carried out [32], the authors reported that the cell was not “blown to pieces”; unfortunately, they do not specify if they captured images

for higher fluences where the cell was actually “blown to pieces”. In our case, it is evident that the cells resulted being “blown to pieces” and therefore melanin leaked out the cell and diluted in the PBS solution, which was determined with the nanodrop spectrophotometer.

There is evidence that UV and VIS radiation produce damage to subcellular structures via photosensitization, a process in which a molecule absorbs light and produces reactive species that alter cellular molecules and initiate cellular responses, e.g., apoptosis [33,34]. It was proven that when Rose Bengal is used as photosensitizer, 532 nm light induces oxygen singlets, while 355 nm radiation induces both oxygen singlets and highly reactive free radicals. Free radicals were found to damage membrane functions more effectively than oxygen singlets [33]. Furthermore, for the 355 nm wavelength, melamoma cells are more likely to go through a combination of photochemical decomposition biomolecules due to the UV light [35] than the 532 nm wavelength. These biological and chemical mechanisms, along with a stronger photothermal interaction of melanosomes with UV light may explain the differences in the cell survival rate we observe at both wavelengths.

Long term effects on cell viability were not considered in this study as these are not significant for the design of the CMC photoacoustic detection system and are beyond the scope of this investigation. Further research with shorter time resolution is required to better understand the boiling phenomenon. The required time resolution is possible by synchronizing the pump nanosecond laser pulse with a femtosecond laser as a probe pulse.

Conclusions

Four main conclusion statements can be extracted from this study:

(1) There is statistically significant difference in the slope of the curve fit that indicates the amount of cells that survived laser irradiation for both wavelengths. λ=355 nm kills cells at a higher rate (*vs* fluence) than λ=532 nm.

(2) There is statistically significant difference in the integrated pressure resulting from irradiation of melanoma cells with both wavelengths up to 0.6 J/cm^2, as expected due to the 4-fold increment in the melanin absorption coefficient at λ=355 nm with respect to λ=532 nm[9]. For fluences higher than 0.6 J/cm^2, the higher amount of damaged cells at 355 nm may be precluding appropriate photoacoustic detection. Integrated pressure detected is the superposition of pressure due to thermoelastic expansion of melanosomes and pressure resulting from the giant optoacoustic effect.

(3). The post-laser irradiation absorbance of the mixture of melanin and PBS increases equally for the two wavelengths used in the experiments, which suggests that although the λ=355 nm irradiation is killing cells at a greater rate, melanin is leaking from them just as much as it does for λ=532 nm irradiation.

(4) The main plasma membrane damage mechanism is microbubble formation within the cell, though it is not linearly correlated to laser energy absorption only; thus, mechanisms other than laser light absorption contribute to the plasma membrane damage. From a practical standpoint, λ=355 nm wavelength does not offer a much larger SNR of the photoacoustic signal with respect to λ=532 nm.

References

1. Braun S, Naume B. Circulating and Disseminated Tumor Cells. J Clin Oncol 2005; 23(8):1623-1626.

2. Cristofanilli M, Budd GT, Ellis MJ, Stopeck A, Matera J, Miller MC, Reuben JM, Doyle GV, Allard WJ, Terstappen LWMM, Hayes DF. Circulating Tumor Cells, Disease Progression, and Survival in Metastatic Breast Cancer. N Engl J Med 2004; 351(8):781-791.

3. Ghossein RA, Bhattacharya S, Rosai J. Molecular Detection of Micrometastases and Circulating Tumor Cells in Solid Tumors. Clin Cancer Res 1999; 5(8):1950-1960.

4. Mocellin S, Hoon D, Ambrosi A, Nitti D, Rossi C. The Prognostic Value of Circulating Tumor Cells in Patients with Melanoma: A Systematic Review and Meta-analysis. Clin Cancer Res 2006; 12(15):4605-4613.

5. Loberg RD, Fridman Y, Pienta BA, Keller ET, McCauley LK, S. TR, Pienta KJ. Detection and Isolation of Circulating Tumor Cells in Urologic Cancers: A Review. Neoplasia 2004; 6(4):302-309.

6. Ring AE, Zabaglo L, Ormerod MG, Smith IE, Dowsett M. Detection of circulating epithelial cells in the blood of patients with breast cancer: comparison of three techniques. British Journal of Cancer 2005; 92(5):906-912.

7. Swetter S. Malignant melanoma. wwwemedicinecom/DERM/topic257htm 2008.

8. Wain E, Stefanato C, Barlow R. A clinicopathological surprise: amelanotic malignant melanoma. Clin Exp Dermatol 2008; 33:365-366.

9. http://omlc.ogi.edu/spectra/melanin/jacques.mcauliffe.gif.

10. Jacques SL, et.al. The Melanosome: Threshold temperature for explosive vaporization and internal absorption coefficient during pulsed laser irradiation. Photochemistry and Photobiology 1991; 53(6):769-775

11. Weight RM, Viator JA, Dale PS, Caldwell CW, Lisle AE. Photoacoustic detection of metastatic melanoma cells in the human circulatory system. Opt Lett 2006; 31(20):2998-3000.

12. Zharov VP, Galanzha EI, Shashkov EV, Khlebtsov NG, Tuchin VV. In vivo photoacoustic flow cytometry for monitoring of circulating single cancer cells and contrast agents. Opt Lett 2006; 31(24):3623-3625.

13. Ara G, Anderson RR, Mandel KG, Ottesen M, Oseroff AR. Irradiation of Pigmented Melanoma Cell With High Intensity Pulsed Radiation Generates Acoustic Waves and Kills Cells. Lasers in Surgery and Medicine 1990; 10:52-59.

14. Neumann J, Brinkmann R. Boiling nucleation on melanosomes and microbeads transiently heated by nanosecond and microsecond laser pulses. Journal of Biomedical Optics 2005; 10(2):024001-024012.

15. Neumann J, Brinkmann R. Nucleation dynamics around single microabsorbers in water heated by nanosecond laser irradiation. Journal of Applied Physics 2007; 101(11):114701-114709.

16. Faraggi E, Gertsman BS, Sun J. Biophysical effects of pulsed lasers in the reitna and other tissues containing strongly absorbing particles: shockwave and explosive bubble generation. Journal of Biomedical Optics 2005; 10(6):064029-(064021-064010).

17. Pustovalov VK, Jean B. Theoretical Investigations of the Processes of Selective Laser Interaction with Melanin Granules in Pigmented Tissues for Laser Applications in Medicine. Laser Physics 2006; 16:1011-1028.

18. Brinkmann R, Huttmann G, Rogener J, Roider J, Birngruber R, Lin CP. Origin of Retinal Pigment Epithelium Cell Damage by Pulsed Laser Irradiance in the Nanosecond to Microsecond Time Regimen. Lasers in Surgery and Medicine 2000; 27:451-464.

19. Lee H, Alt C, Pitsillides CM, Lin CP. Optical detection of intracellular cavitation during selective laser targeting of the retinal pigment epithelium: dependence of cell death mechanism on pulse duration. Journal of Biomedical Optics 2007; 12(6):064034-064014.

20. Neumann J, Brinkmann R. Cell disintegration by laser-induced transient microbubbles and its simultaneous monitoring by interferometry. Journal of Biomedical Optics 2006; 11(4):041112-041111.

21. Roegener J, Brinkmann R, Lin CP. Pump-probe detection of laser-induced microbubble formation in retinal pigment epithelium cells. Journal of Biomedical Optics 2004; 9(2):367-371.

22. Lapotko DO, Lukianova EY, Shnip AI. Photothermal detection of laser-induced damage in single intact cells. Lasers in Surgery and Medicine 2003; 33(5):320-329.

23. Egerev S, Ermilov S, Ovchinnikov O, Fokin A, Guzatov D, Klimov V, Kanavin A, Oraevsky A. Acoustic signals generated by laser-induced metal nanoparticles. Applied Optics 2009; 48:C38-C45.

24. Lin CP, Kelly MW. Cavitation and acoustic emission around laser-heated microparticles. Applied Physics Letters 1998; 72:2800-2802.

25. Oraevsky AA. Laser-induced acoustic and shock waves in ocular tissues: Armstrong Laboratory, Occupational and Environmental Health Directorate, Optical Radiation Division 1995.

26. Lapotko DO, Lukianova E. Laser-induced micro-bubbles in cells. International Journal of Heat and Mass Transfer 2005; 48(1):227-234.

27. Gerstman BS, Thompson CR, Jacques SL, Rogers ME. Laser Induced Bubble Formation in the Retina. Lasers in Surgery and Medicine 1996; 18:10-21.

28. Vitkin IA, Woolsey J, Wilson BC, Anderson RR. Optical and Thermal Characterization of Natural (Sepia officinalis) Melanin. Photochemistry and Photobiology 1994; 59(4):455-462.

29. Huttmann G, Birngruber R. On the possibility of high-precision photothermal microeffects and the measurement of fast thermal denaturation of proteins. Ieee Journal of Selected Topics in Quantum Electronics 1999; 5(4):954-962.

30. Oraevsky AA, Jacques SL, Tittel FK. Mechanism of laser ablation for aqueous media irradiated under confined-stress conditions. Journal of Applied Physics 1995; 78(2):1281-1290.

31. Oraevsky AA, Jacques SL, Esenaliev RO, F.K. T. Pulsed laser ablation of soft tissues, gels, and aqueous solutions at temperatures below 100°C. Lasers in Surgery and Medicine 1996; 18(3):231-240.

32. Lin CP, Kelly MW, Sibayan SAB, Latina MA, Anderson RR. Selective Killing by Microparticle Absorption of Pulsed Laser Radiation. IEEE Journal of Selected Topics in Quantum Electronics 1999; 5:963-968.

33. Kochevar IE, Lambert CR, Lynch MC, Tedesco AC. Comparison of photosensitized plasma membrane damage caused by singlet oxygen and free radicals. Biochimica et Biophysica Acta 1996; 1280:223-230.

34. Kulms D, Schwarz T. Molecular Mechanisms Involved in IV-Induced Apoptotic Cell Death. Skin Pharmacol Appl Skin Physiol 2002; 15:342-347.

35. Vogel A, Venugopalan V. Mechanisms of pulsed laser ablation of biological tissues. Chem Rev 2003; 103:577-644.

Appendix

This appendix provides a detailed guide of the most important materials and methods used while the work presented in this thesis was done. It presents basically more details about the Materials and Methods section of each chapter that are usually not reported in a thesis. When a new researcher comes to the lab, he/she will find a quick reference on how to get started. Looking at the equipment manuals will always be advised and encouraged.

Tissue models

Agar gels

Agar gels are excellent tissue models because its thermal properties are close to those of real tissues due to its high water content; in addition, its mechanical and optical properties can be adjusted to make a more realistic tissue model. Agar gels can be made with any geometry.

The most used concentration of agar gel was 2 gr. of agar powder (BD Biosciences 214530) in 100 mL of deionized water. It is important to use deionized water to avoid impurities in the gel. A hint to make the gel successfully is to dilute the agar powder in an aliquot of the water when it is cold and bring the rest of the water to a boil; once the water is boiling, pour the solution of agar powder and cold deionized water into the boiling water and stir thoroughly until the whole gel solution boils, then remove from heat source. Let the gel rest for a few minutes so the vapor bubbles disappear and the liquid gel looks clear and clean. Then pour the liquid gel in a mold designed for the experiment and wait for it to gel.

The agar powder concentration can be adjusted to change the mechanical properties of the gel, but in general it is difficult to make agar gels with concentration higher than 4 gr. of agar gel in 100 ml of water.

Dyes

Water-soluble dyes will change the optical properties of the tissue models. The one used for this work was Direct Red (Sigma-Aldrich, 195251). Its absorption coefficient spectrum is shown in Figure 4.1.

Its absorption peak is around the green part of the spectrum. That is the reason for using green wavelengths for selective treatment of vascular lesions. Figure A.1 shows a plot of absorption coefficient of Direct Red in aqueous solution at λ=532 nm as a function of dye concentration. These data were obtained using a photospectrometer.

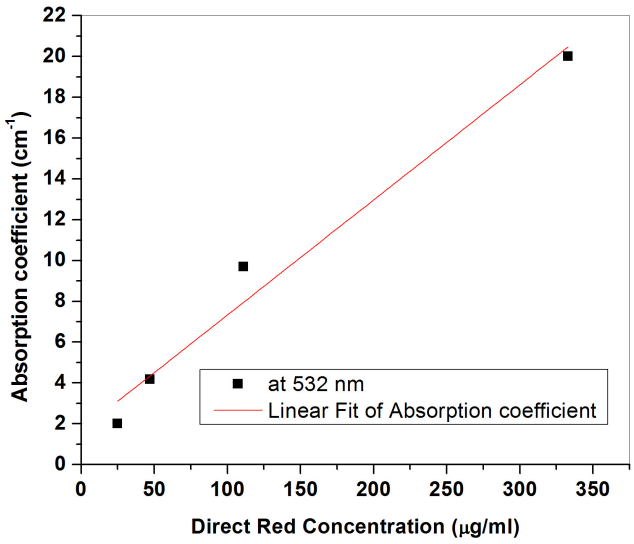

Fig A.1 Absorption coefficient of Direct Red in aqueous solution at λ=532 nm as a function of the dye concentration. Linear fit equation is y=0.0564x+1.6945. Experimental data was acquired using a photospectrometer.

Piezoelectric Transducers

The piezoelectric transducers used were made of Polyvinylidene Fluoride (PVDF) (Ktech, Albuquerque, NM) which is a piezoelectric polymer. The transducer is made of three main components, the piezoelectric film, the body and a BNC connector.

Electrical model

PVDF film is a piezoelectric material, it responds to the pressure on its surface with an electric signal that can be read using an oscilloscope. An analysis of the signal provides with information about the rate of change of the pressure with respect to time.

The transducer can be electrically modeled as a current source in parallel with a capacitor and a resistance. The capacitor is the intrinsic capacitance of the transducer, it can be directly measured with a multimeter and it is usually in the order of nanofarads or even picofarads. The resistance is the equivalent resistance of the internal resistance of the transducer and the load resistance in parallel. The first can also be easily measured with a multimeter and the latter is the impedance used to connect the transducer to an oscilloscope. Most digital oscilloscopes have two coupling impedances, 1M Ω and 50 Ω. Figure A.2 shows the diagram of the equivalent electric circuit of a PVDF transducer.

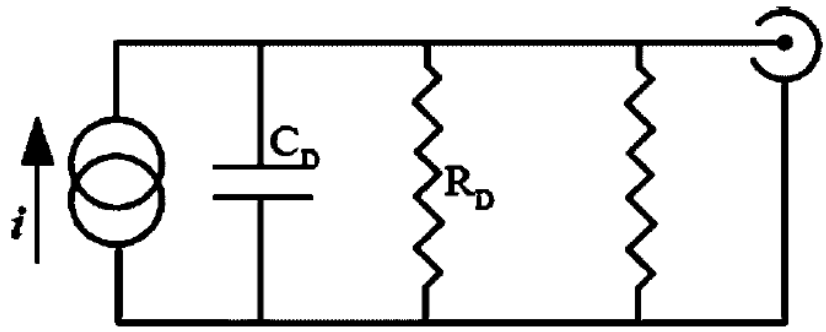

Fig A.2 Equivalent electric circuit of a PVDF transducer. It can be modeled as a current source in parallel with a capacitor, internal resistance (both intrinsic) and a load resistance (either 50Ω or 1 M Ω).

The source current is proportional to the time derivative of the pressure exerted on the transducer surface, so the circuit equation is given by

$$C\frac{dV}{dt}+\left(\frac{1}{R_D}+\frac{1}{R}\right)V = B\frac{d}{dt}(\Delta P) \tag{A.1}$$

where C is the transducer capacitance, R_D is the internal resistance and R is the load resistance, B is a constant that depends on the manufacturing process. When dV/dt >> 1/RC, the electric signal from the sensor V is proportional to the pressure fluctuation ΔP; when dV/dt<< 1/RC, the electric signal V is proportional to the time derivative of the pressure fluctuation. The sensor was connected to a digital oscilloscope through a 1MΩ impedance to ensure proportionality of voltage to pressure.

Piezoelectric film preparation

The piezoelectric film is a 25 μm thick film aluminized on both sides. The sides of the film come identified as positive and negative. It is necessary to etch the aluminum coating to make a defined pattern of the active area of the sensor. The portion of aluminum coating that should not be removed must ensure there is good electric contact to the electrodes that must be connected to the BNC connector. Electrical tape is the best option to mask the portion of aluminum coating that must not be etched.

The etching process is done immersing the piece of film with the appropriate electrical tape mask into a 0.3 molar solution of Iron Chloride (III) between 50 and 60 ^{o}C. Immerse the film for no more than 2 to 3 seconds stirring thoroughly to avoid overheating of the piezoelectric polymer and affecting its time response. Double-check the etching process and repeat immersion if necessary. Usually no more than two immersions are necessary.

Glue positive side of the film to the electrode connected to the positive side of the BNC using cyanoacrylate, commercially known as Krazy glue and let it cure.

Calibration

As the PVDF films have been subject to some heat during the etching process, the D33 measurements from the manufacturer may not be entirely accurate. Also, other factors (especially those related to induced charge) will affect actual sensitivity so the following procedure should be used to determine the sensitivity of the PVDF sensor. The result will be in mV/bar, or voltage signal/ unit pressure.

Prepare several (about 5) absorbing solutions made using deionized water and a photostable dye, such as Direct Red. These solutions will be irradiated with a Q-switched laser to induce acoustic waves of predictable pressure amplitude. Visually, these solutions in a 1 cm thick cuvette will be light to very dark. Measure the absorption coefficient of the solutions at the laser wavelength using a spectrophotometer. The second harmonic of the Nd:YAG which is 532 nm is a common wavelength highly absorbed by Direct Red. The absorption coefficient will be equal to

$$\mu_a = \frac{2.303A}{z} \tag{A.2}$$

where A is the absorbance (measured on the spectrometer) and z is the thickness of the sample (cuvette thickness).

Put one of the absorbing solutions on the PVDF transducer. An easy way to do this is by making a small tub with a half inch inner diameter section of PVC piping that is cut in about a half inch length. Fix a piece of celophane on one end with a rubber band so that you have made a little cup from the PVC and celophane. The celophane bottom is used since its thickness is small compared to the acoustic wavlength. Put some absorbing solution in the tub and place it on the PVDF. There should be a drop of water on the PVDF to ensure acoustic coupling between the PVDF and the solution.

Irradiate the solution from above, like it is shown in Figure A.2 with the Q-switched laser. Ensure that the radiant exposure is not greater than 0.03 J/ cm^2 or the acoustic generation will be nonlinear and the analysis won't work out.

The predicted pressure of the photoacoustic wave can be described as

$$p(0) = \frac{10}{2}\Gamma F \mu_a \tag{A.2}$$

where p(0) is the peak pressure of the acoustic wave, Γ is 0.12 at room temperature, and F is the radiant exposure of the laser beam in J/ cm^2. This pressure will be in bars. The calibration factor is the quotient of the peak voltage by this pressure at this μ_a in Volts/bar.

Repeat this procedure for all Direct Red concentrations and perform a linear regression to determine the calibration for this transducer.

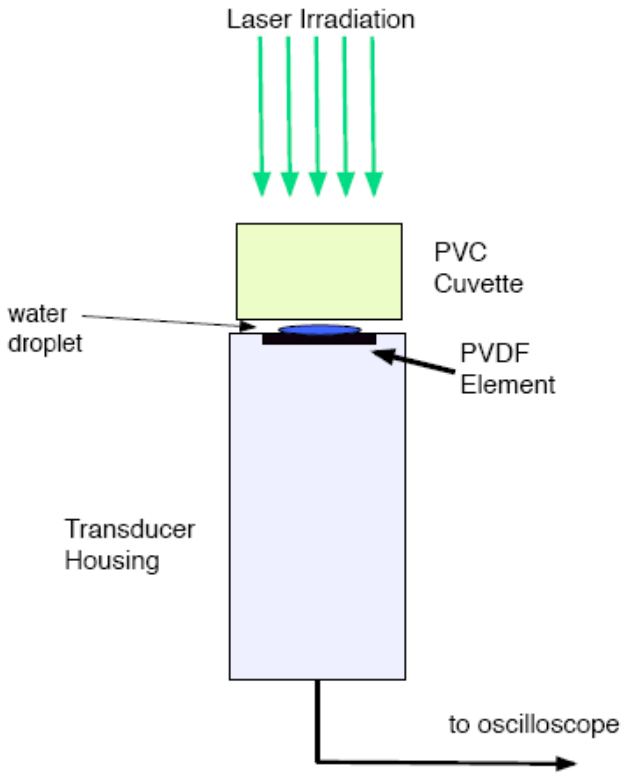

Fig A.3 Set up for calibrating the PVDF sensor. The PVC cuvette contains the Direct Red solutions.

Equivalent target plane system (ETP)

A CCD camera is used to capture the image of the focused beam on the target; this is done by using an image relay system constituted by the microprocessing lens and the ETP lens shown in Fig. A.4. The microprocessing lens is an aspheric lens that minimizes spherical aberrations with focal length of 6 mm; the ETP lens is a long focal length lens, 500 mm for example. The light that reflects backwards from the surface of the sample is collected by the two lenses projecting an image of the beam waist on to the CCD.

The beam waist image at the sample surface captured can be used to measure the beam waist using image processing software, ImageJ for example, to latter calculate the laser fluence used for experiments. A reference of the pixel size must be acquired positioning a reticule at the samples position and a white light

source. It is important to ensure that the image in the CCD is not saturated using ND filters in front of the CCD.

This image relay system provides two very useful features to the set up:

(1) It requires normal incidence to work so that the sample surface is always perpendicular to the incident beam, and therefore, in the event of a transversal scan of the sample the beam waist of the focusing light stays always at a constant distance from the surface.

(2) It allows fine positioning of the beam waist right on the surface of the sample, and hence at a know depth within the layer, with a resolution of the order of the Rayleigh range of the focusing beam, and; (3) the same image relay system allows to record movies of the bubble formation and evolution inside the agar gel.

The light that reflects off the beam splitter (BS) goes to an energy monitor that must be previously calibrated against an energy meter positioned at the samples position. As energy monitor a fast photodiode connected to an oscilloscope measuring the peak-to-peak voltage or, in turn, another energy meter connected to a computer can be used for data acquisition.

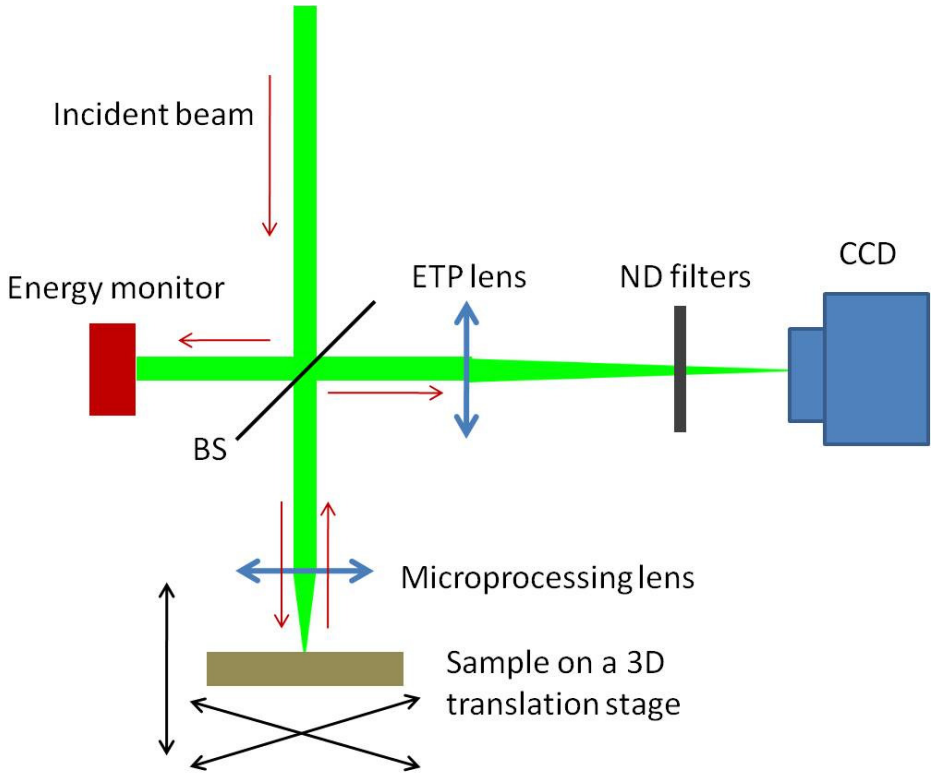

Fig A.4 Schematic of ETP system

Time-resolved imaging system

Details on how to manipulate the remote controls of the laser systems are beyond the scope of this appendix. The reader is encouraged to go over the manuals of each laser, available at the laboratory, to become familiar with the operation of each laser system.

The requirement of the time-resolved imaging system (TRI) to work is to have a highly repetitive phenomenon to study, as it is the case of plasma-induced bubbles in aqueous media.

The system works electronically synchronizing two Nd:YAG, Q-switched lasers by means of a delay generator. One of the lasers is known as *pump* and is the one that drives that interaction between the light and the material, in other words, is the one that produces the interaction to study. The second laser is known as *probe*, and is the one that provides the illumination for imaging the interaction. Typically the

energy of the laser pulses used as a probe must be kept as low as possible, say a few microjoules or less; there are two reasons for that: first, it is desired to avoid any interaction of these laser pulses with the target, and second, is because it is very easy to saturate the CCD and additional ND filters in front of the CCD may be required. If possible, select the wavelength that is less absorbed by the material to be studied.

The idea is that a delay generator sends electronic pulses of the appropriate voltage and duration to the external triggering ports in the power supplies of each laser to trigger each laser. By adjusting the relative delay of the probe laser with respect to the pump laser, it is possible to acquire images with time resolution in the order of the laser pulse duration.

Most of the times, the EKSPLA laser was used as probe since it incorporates the Optical Parametric Oscillator (OPO), which allows to change the wavelength of the probe laser pulse, and the Quantel laser with the second harmonic unit as a pump. Each laser has different external triggering requirements. The Quantel laser requires that both, the flash lamp and the Q-switch are triggered by independent electronic pulses; the relative delay between these pulses that produces the maximum energy out of the laser is 167 μs. The EKSPLA laser requires that a single electronic pulse to be triggered externally; the rise edge of the pulse triggers the flashlamp, while the fall edge triggers the Q-switch, a pulse duration of 300 μs gives the maximum energy out of the laser. Both lasers must be triggered at 10 Hz. The delay generator available at the lab, BNC 555, has 4 channels. For convenience, channels A and B were used to trigger the flashlamp and the Q-switch of the Quantel laser, while channel C was used to trigger the EKSPLA laser. Channel D was used to trigger a CCD camera for experiments where a single laser pulse was nor required.

Experiments where a single pump laser pulses are required, like those in Chapter 5 about time-resolved imaging of intracell-laser pulse interactions, are possible incorporating a mechanical shutter in the pump beam path. While the laser pulses are triggered at 10 Hz, that is a laser pulse each 100 ms, the shutter is open for only 100 ms to ensure that only one laser pulse goes through, while the latter laser pulses are blocked by the shutter. The shutter is open for 100 ms when it is externally triggered with a function

generator that sends a single TTL pulse 100 ms long. The same TTL pulse should be sent to the CCD camera and allow the camera's exposure to be at least 100 ms. With this configuration, the user can randomly trigger the TTL that goes to the shutter (and CCD camera) allowing a single laser pulse be delivered to the target. The down side of this methodology is that, if the pump beam is high energy, it is necessary to immediately block the pump beam as it damages the shutter.